CLUSTER ION BEAM INDUCED NANO METALLIC RIPPLE STRUCTURE FOR LOCALIZED SURFACE PLASMON RESONANCE (LSPR) BASED BIOSENSOR

AND

BACTERIAL GROWTH ON NANO RIPPLE GLASS SUBSTRATE UNDER THE INFLUENCE OF WEAK MAGNETIC FIELDS

A Dissertation Presented to

the Faculty of the Department of Physics

University of Houston

In Partial Fulfillment

of the Requirements for the Degree

Doctor of Philosophy

By

Iram Saleem

August 2017

CLUSTER ION BEAM INDUCED NANO METALLIC RIPPLE STRUCTURE FOR LOCALIZED SURFACE PLASMON RESONANCE (LSPR) BASED BIOSENSOR

AND

BACTERIAL GROWTH ON NANO RIPPLE GLASS SUBSTRATE UNDER THE INFLUENCE OF WEAK MAGNETIC FIELDS

_____
Iram Saleem

APPROVED BY:

_____
Dr. Wei-Kan Chu, Chairman
Department of Physics

_____
Dr. Samina Masood,
Department of Physics

_____
Dr. Widger William,
Department of Biology and Biochemistry

_____
Dr. Gemunu H. Gunaratne,
Department of Physics

_____
Dr. Dong Cai,
Department of Physics

_____
Dean, College of Natural Sciences and Mathematics

CLUSTER ION BEAM INDUCED NANO METALLIC RIPPLE STRUCTURE FOR LOCALIZED SURFACE PLASMON RESONANCE (LSPR) BASED BIOSENSOR

AND

BACTERIAL GROWTH ON NANO RIPPLE GLASS SUBSTRATE UNDER THE INFLUENCE OF WEAK MAGNETIC FIELDS

An Abstract of a Dissertation

Presented to

the Faculty of the Department of Physics

University of Houston

In Partial Fulfillment

of the Requirements for the Degree

Doctor of Philosophy

By

Iram Saleem

August 2017

Acknowledgments

It is my genuine pleasure to express my highest gratitude and appreciation to my thesis advisor, Dr. Wei-Kan Chu for his continuous assistance, encouragement and support that he provided during the entire duration of my research activity. My special thanks are reserved for all the committee members; Dr. Dong Cai, Dr. Gemunu Gunaratne, Dr. Samina Masood and Dr. William Widger for their inspiring suggestions, constructive criticism and helpful suggestions. Dr. Widger and Dr. Masood deserve a special gratitude for the collaborative support in research too.

I appreciate all the support of my friends and colleagues including Dr. Dharshana Wijesundera, Dr. Buddhi Tilakaratne, Dr. Epie Njumbe, Kalyan Sasmal and Derek Smith for the several useful and productive discussions. Dr. Dharshana Wijesundera, provided guidance and constant encouragement throughout. I also owe a great debt of gratitude and extreme appreciation for my Uncle M. A. Sheikh, my Aunt and cousin Alishpa, who were there whenever I needed them and made it possible to achieve the goal timely. I would be remiss if I did not acknowledge my late grandmother Hanifa Begum who dreamt about me earning doctorate degree while I was just a little girl. I wish she could see that her dream became a reality.

Last but not least, this wouldn't have been possible without the continuous support of my family. I am grateful to my dad Dr. Hamid Saleem who is my true inspiration and role model, my mother Rubina Hamid, who is behind every success I have ever achieved and for being my strength, my sister Sania Saleem for her incredible support throughout, my

brother Dr. Zain Hamid Saleem deserves a special gratitude for his immense support in setting my career goals and providing a sense of trust and confidence in my abilities, and my lovely daughter Arisha who is the love of my life and my motivation.

I am deeply grateful to all my teachers and staff of the physics department of UH and Texas Center for Superconductivity (TcSUH), who contributed towards the attainment of this goal. Each one of them played an important role and I am extremely thankful.

Contents

Abstract

SECTION I

SECTION II

Abstract

This thesis is comprised of two sections. First section describes the development of a simple and cost-effective scheme for bio-sensing, described as the detection of various biological elements inside a system or a body (that can be harmful or dangerous) with the help of specific biological receptor units. Gold nano-ripple pattern is prepared using a gas cluster ion beam (GCIB) system. When the nano-ripple surface is exposed to electromagnetic light, it shows localized surface plasmon resonance (LSPR) effect. Because of this plasmonic behavior, interaction of the targeted biomolecules and the receptors on the surface, sends optical signals that is processed to determine the presence of the specific biomolecule in the body. This LSPR nano-ripple gold biosensor was used to detect antibody-antigen reaction of rabbit X-DENTT antibody and DENTT blocking peptide (antigen) using adsorbate-induced LSPR-wavelength shift from the nano-ripple gold surface and its dependence on the antigen concentration. This approach does not require any chemical processes for its design and has the prominent advantage of possibility of large surface area coverage and applicability to different starting materials. These biosensors have monolayer scale sensitivity and high selectivity. The nano-ripple biosensor can be further developed to obtain a real time analytical detection mechanism.

The second section presents the experimental results based on the effect of weak magnetic field on the growth of bacteria on glass nano structures. Bacteria is found to adhere more on nano-ripple pattern and larger bacterial colonies were observed in comparison to the plain glass surface. Moreover, magnetic field affects the growth by reducing the size of

colonies. In another experiment, we examined the effects of different magnetic field configurations, including static (homogeneous and non-homogeneous) and time-varying magnetic fields, on various species of bacteria on a plain glass surface based on their growth rates. Magnetic field suppresses the growth of bacteria and slowest growth rate was observed in bacteria treated with time-varying magnetic field.

Section I

Chapter 1

Introduction

Biosensor research has gained enormous attention in recent years in which tens of thousands of papers have been published and there lies a growing interest in biosensor applications in a variety of fields including medicine and nanotechnology [1-3]. Biosensors are becoming increasingly important and used as practical tools for healthcare monitoring, drug screening, clinical analysis and diagnosis of diseases, agricultural and environmental applications, industrial processing and monitoring, and in food safety control. Scientists are developing biosensing devices offering simple instrumentation, inexpensive, and label-free procedures that do not require large sample volumes.

Many new approaches and strategies have been developed towards biosensors for clinical applications including enzyme-based biosensors, immunological biosensors, and DNA biosensors. Biosensors are devices with a biological-recognition element such enzymes, antibodies, and other receptors that captures the analyte in the solution and an optical or electronic transducer which converts the event into a quantifying measurable signal. Biological sensors have the ability to detect pathogens and perform genetic testing even for point of care analysis. They have shown tremendous potential for disease-specific biomarkers and real-time monitoring of biological signals [4-6]. For early-stage disease detection and

treatment, it is very important to recognize the health-related complexity in a timely manner. Biosensors prove to be very powerful tool for that matter.

Nanotechnology has played an important role in improving the sensitivity and performance of biosensors. A fast, reproducible, and selective sensing technique is important to obtain information used for disease control, environmental monitoring and agricultural productivity. Nanomaterials enable rapid and continuous detection, reproducibility and sensitive response that is extremely useful for a broad range of areas such as food processing, medical, pharmaceutical, and defense, and water purification systems. The use of nano biosensors brings about a combination of advantages including low cost, integrated, miniaturized devices, selective biological recognition, operational convenience, and high sensitivity. The advancement in biosensors and biotechnology must meet the rapidly growing need for rapid clinical and medical diagnostics.

In recent years with the development of optical biosensing devices, there has been more focus on discovering new technologies and methods to exploit the optical properties of noble metal nanostructures due to their ability to generate localized surface plasmon resonance (LSPR). Localized surface plasmon resonance (LSPR) effect of metal nanostructures has attracted considerable research interest because of its potential applications in several areas including sensors [7], surface enhanced spectroscopy [8, 9], photovoltaics [10, 11], sub-wavelength microscopy [12, 13], near-field lithography [14], nano-photonics [15], bio-imaging [16], laser photo thermal therapy [17], and numerous other applications. LSPR results from coupled

oscillations between the charge density of conduction electrons and their corresponding electromagnetic field in conductive nanostructures that are smaller in dimension compared to the wavelength of exciting electromagnetic radiation, which results in enhanced absorption and scattering resonances [18]. The unique plasmonic property of metals resides in the fact that their dielectric constant is a complex function of the frequency of incident light, $\varepsilon(\omega) = \varepsilon_1(\omega) + i\varepsilon_2(\omega)$. The imaginary component, $\varepsilon_2(\omega)$, causes the resonant behavior. The LSPR peak relies greatly on the shape, size, and composition of the nanostructures. Application of the LSPR effect therefore critically depends on reliable and efficient ways of controlled fabrication of metallic nanostructures.

LSPR sensing chips are nanostructured reusable substrates that use simple optical extinction spectrum for sensing purposes. In my dissertation, I will explain the details of the fabrication and working of the LSPR based optical nano-ripple gold biosensor with argon gas cluster ion beam bombardment. Such a sensor brings several advantages including simple configuration, easy to fabricate (single-step fabrication process), cost effective, large area coverage, label-free, high sensitivity and specific selectivity and the potential of real-time detection analysis. The biosensing chip detects the antibody-antigen binding on its surface and can be similarly used for all receptor-ligand pair by anchoring either the ligand or the receptor to the gold nano-ripple surface.

Chapter 2 is about the gas cluster ion beam (GCIB) system that is used to make the nano-ripple pattern on a thin gold film. It talks about the apparatus of the machine

and the various other characteristics and applications of the GCIB equipment. The difference between a cluster ion beam and a monomer ion beam is explained together with the mechanism of cluster-solid interaction. In Chapter 3, the localized surface plasmon resonance behavior of the nano-ripple metallic substrate under the effect of an incident electromagnetic light and its dependence on the nano-ripple dimension and the polarization of the electric field is emphasized. I will also describe the formation of the self-assembled nano metallic rippled structure induced by oblique cluster ion beam irradiation and its potential for plasmonic sensing applications.

Chapter 4 demonstrates how the localized surface plasmon resonance (LSPR) property of the nano-ripple gold substrate can be utilized for bio-molecular sensing application. It reveals the high sensitivity and the specific-selective nature of the biosensing chip. The dependence of the plasmon resonance spectral peak the surrounding dielectric environment and on the surface morphology which is related to the cluster ion beam fluence is explained in detail. LSPR peak shifts with monolayer adhesion of organic molecules indicates it can be used for various bio and chemical sensing applications. Theoretical model descriptions on ripple formation is discussed briefly. Chapter 5, demonstrates the development of the gold nano-ripple substrate into a bio- chemical sensor. It show the details of the detection mechanism of an antibody-antigen interaction by the nano-ripple LSPR biosensing chip and the advantages of this technology are discussed in detail together with the future possible advancement in the field.

Chapter 2

Gas Cluster Ion Beam (GCIB) System and Applications

In the past few decades the development and demands in surface modification techniques have required better control of surface structures of nanoscale dimension. Such processes have the need of a few hundred eV of ion beam energies. A cluster ion beam has the advantage of producing high current ion beams at low energy for surface treatments and is a unique tool for modification of material surfaces [19, 20]. Aggregates of tens, hundreds, or even as many as thousands of atoms or molecules ionized to a single charge state are accelerated in an electric field of low energy in the GCIB system. The kinetic energy of a cluster is shared by its constituent atoms and each atom in the cluster carries only a few eV of energy. Thus when the clusters strike a surface, it results in a shallow penetration of the atoms on the surface and they stop in the first few layers of the target material.

The interaction of solid surfaces with gas cluster ions and the potential applications for those interactions has been a topic of great interest along with the cluster material, cluster energy is also deposited in a very thin layer at the surface which creates a very high energy density in a very small volume where unique physical and chemical processes take place. For novel technological applications these processes can be very useful in modifying materials [21].

Considerable advancement has been directed towards issues associated with transporting and generating cluster ion beams that can be used in practical processing equipment. Applications of cluster ion beam have been applied to a significant range of materials for smoothing, etching, and chemical transformation effects. It offers uniformity, excellent throughput, and reproducibility over large area targets.

The history of argon GCIB developments, the equipment, the fundamentals of gas cluster impacts, and the applications of GCIBs has been reviewed in detail in reference [22]. Originally argon GCIBs were developed for low damage etching, surface smoothing, trimming, and shallow doping among other aspects. The successful applications of argon GCIBs have been demonstrated in the manufacturing of semiconductor devices, surface polishing, film formations, depth profiling, surface modification of various materials including magnetic.

2.1 Cluster Ion solid interaction

The cluster ion beam has the advantage of generating highly energetic incident clusters accelerated to impact the substrate by means of an applied voltage and the fluence of these incident clusters is adjustable. Cluster ion beam with total energy of several Kev shared among its constituent atoms, upon impact penetrates in to the target surface. Thousands of gaseous atoms bonded by van der Waals force falls on the surface of the substrate and undergo the sputtering effect due to the cluster ion-solid interaction. Cluster ion solid interaction is very different from monomer ion-solid interaction. The simultaneous arrival of

clusters of thousands of atoms at the same location produces multiple lateral collisions between the incident and the target surface atoms which is why the lateral sputtering of the surface target atoms takes place, which then redeposit on the surface depressions and smoothens the solid surface. The energetic clusters have a large mass but low energy per individual atom, thus the penetration depth is determined not by high energy of the clusters but by the low energy carried by the constituent atoms. The high total energy carrier clusters upon impact transfer their energy to a small impact volume typically of the order of a tens of angstroms. Consequently, extreme pressure and temperature conditions are generated in a small volume of the surface that adds to high sputtering yields and strong enhancement in chemical reactivity and diffusion and ejection of target material. These characteristics make cluster beam a particularly suitable technique for growth of films on substrates even at low temperatures, especially the surfaces that are difficult to coat using other deposition techniques [23].

The main characteristic of the GCIB processes is to allow adjustment for the incident energy, the cluster size and the flux which explains its broad range of application in surface modification, cluster fusion. However in order to achieve optimal process performance for specific applications, it is essential to have a sophisticated system of controlling the process parameters. Gas cluster ion beam GCIB bombardment has emerged as a widely applicable surface smoothing technique for many materials including metals, high T_c-superconducting YBCO films, and semiconductors.

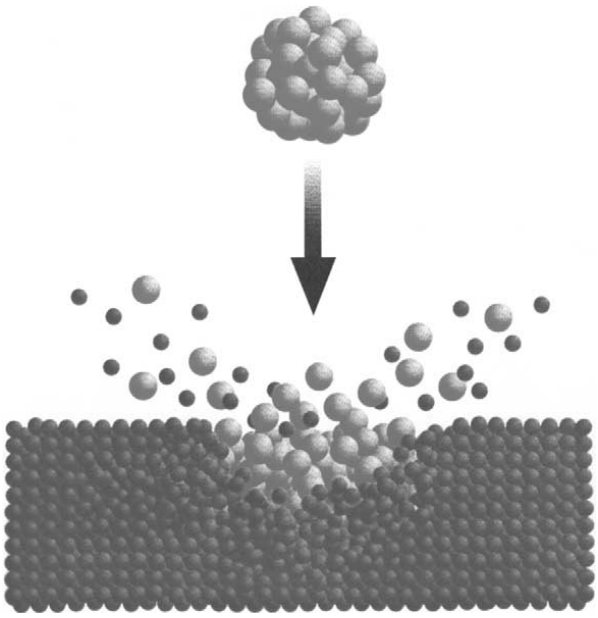

Figure 2.1: Shows a simple representation of cluster impact taken [21].

2.2 Cluster Ions Vs Monomer Ions

Gas cluster ion beams (GCIBs) have low particle energy (velocity) and high particle numbers compared to monomer ion beams. An atom in a gas cluster carries a small fraction of the energy, comparable to the metallic or covalent bond energies, which causes low levels of damage in the surface due to sputtering. For instance, 3000 atoms in a cluster beam accelerated to 30 keV means each atom has 10 eV/atom which is about 2-4 times that of an interatomic bond. Furthermore, cluster ion beam can offer high-sputtering yields and minimal induced-surface damage which is required for some depth profiles by transporting thousands of times larger numbers of atoms at the same ion current compared with monomer ion beams [24].

For the past few decades, the surface self-assembled patterns due to monomer ion bombardment have been extensively studied. In 1962, Navez et al., studied the first self-assembled pattern formation (mainly the ripple pattern) [25]. They observed

glass pattern formation by a charged beam of air of 4 Kev energy and noticed the change in the ripple orientation from perpendicular to parallel to the direction of the beam when the angle of incidence of the beam shifts from surface normal to grazing angles. Bradley and Harper first derived a model for ripple formation on solid materials [26] explaining ripple formation and mechanism behind the process.

2.3 GCIB Apparatus

In supersonic expansion, a high pressure gas adiabatically expands into a vacuum through a de Laval nozzle. The beam condenses and form clusters by limiting the velocity of the gaseous atoms. The large gaseous clusters are bonded with weaker van der Waals forces and the cluster temperature is less than 10 K [27]. The clusters then pass through a metal skimmer and are ionized by speeding electrons generated from a heated tungsten filament. The charged clusters are then mass selected and accelerated into a target chamber. A detailed description of the instrumentation of this cluster ion source is discussed below:

2.3.1 The Nozzle

The nozzle is a very important part of the GCIB system, since its structure controls the gas flow, cluster size, beam divergence, and temperature. Adiabatic expansion in vacuum through a small diameter nozzle flow of a high pressure ion beam with essential parameters produces clusters of gaseous and metal atoms. Nucleation and growth of clusters depends critically upon the nozzle dimensions and shape and on the gas initial temperature and pressure, and is also highly sensitive to the thermodynamic properties of the material. Adiabatic expansion is governed by the

thermodynamics of the expansion process. All atoms and clusters, after expansion move with approximately the same velocity. The large gas flow requires high speed pumping even through a very small nozzle. The translational kinetic energy of the atoms is of the order of their thermal energy before expansion. Noble gas clusters such as Ar gas, whose atoms are loosely bound by Van der Waals forces are readily formed by expansion from a high stagnation pressure. Cluster can be in the form of dimers, molecules or large cluster ions up to about 10 nm in diameter. The first study that indicated condensation of individual vapor expansion out of a small nozzle into a vacuum was conducted by Bechet et al. in 1956. High beam intensity with energy per atom ranging up to 10 Kev require a low specific charge along with the necessary conditions of current and charge density.

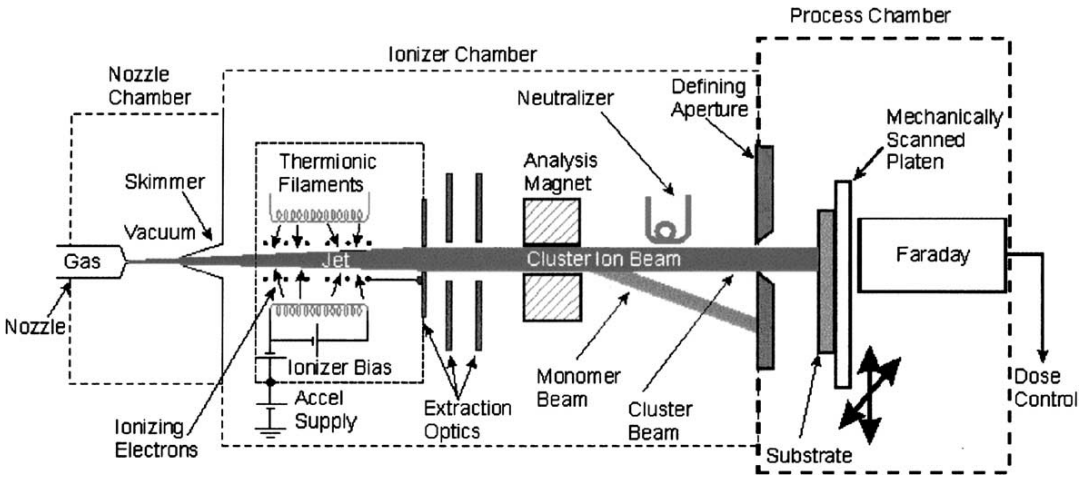

Figure 2.2: Schematic diagram of gas cluster ion beam (GCIB) system [21].

2.3.2 Cluster Formation

Cluster formation is a complicated process and the theoretical descriptions of this process are limited. The phenomena of nucleation and growth takes place through the birth of small molecular clusters that form and grow by molecular collisions.

Cluster-cluster aggregation becomes more evident when the number of the clusters are large.

Initially, dimers are formed when the local temperature is less than the binding energy of the dimer of the gas atoms. These dimers act as condensation nuclei for the cluster growth. The cluster grows with the inclusion of monomers. In order for the cluster to start growing, the ratio of molecules to clusters must be to be large.

$$Ar + Ar + Ar \rightarrow Ar + Ar_2 \tag{2.1}$$

Classically the nucleation process is considered an equilibrium process and the cluster's free energy is equal to the sum the free energy due to the surface of the cluster and of the free energy of the same number of molecules in the bulk state. Change in the Gibbs free energy (ΔG) in thermodynamic theory during the formation of a cluster of radius r is defined as:

$$\Delta G = -\frac{4}{3}\pi r^3 \left(\frac{kT}{V_c}\right) lnS + 4\pi r^2 \sigma \tag{2.2}$$

Where r is the surface energy, S, is the saturation ratio (P/P_∞) of the vapor pressure (P) to the equilibrium vapor pressure (P_∞), V_c is the specific volume per molecule in a cluster and T is the vapor temperature. The surface energy of a bulk state is different from the surface energy of a cluster. Surface energy of a cluster of radius r is:

$$\sigma = \frac{\sigma_0}{1+\frac{2\delta}{r}} \tag{2.3}$$

Where σ_0 is the surface energy for a plane surface of the bulk is state and δ is a correction parameter in the range of 0.25 to 0.6 times the intermolecular distance. ΔG has a maximum at $r*$ which is the radius of the critical nucleus. Clusters larger

than $r*$ are stable, they grow due to condensation whereas clusters with smaller radius are unstable and dissociate by evaporation. $r*$ is calculated to be [28]:

$$r^* = \frac{2\sigma V_c}{kTlnS} \tag{2.4}$$

2.3.3 The Skimmer

Gas at the stagnation pressure, P_o, and temperature, *T*, expands through a nozzle, N, into a region maintained at a pressure, P, by a diffusion pump. A conical skimmer, S, located a distance, d, from the nozzle. The intensity of the cluster beam depends on the distance, d. The directed axial stream of clusters emerging from the nozzle passes through the aligned skimmer which blocks downstream transmission of most of the excess gas and admits the center part of the beam to a high vacuum region maintained at a pressure, P_2. The skimmer in this study is made out of nickel (Ni) and has a diameter of a 0.075 mm. A shock wave called Mash disk is formed in front of the skimmer if the distance between the skimmer orifice and the nozzle is larger than an optimal value and decreases the beam intensity. Also, a high pumping rate turbo pump is essential to reduce distortion caused by the cluster beam interference that can occur due to the evaporating gas collisions with the cluster beam.

2.3.4 Ionization and Acceleration of Clusters

The clusters passing through a skimmer and a collimator, then enters an ionizer. Inside the ionization chamber, the clusters are ionized by electron bombardment and accelerated by applying an extraction voltage to a high potential, typically a few kV to a few tens of kV. The ionized beam consists of both the clusters and the

monomers at this point. A low extraction voltage is applied in order to suppress the monomer ions through the space charge. The cluster ion size distribution can be selected by a retarding potential. The cluster ion beam is then focused by a lens. The extracted and focused ion beam with large clusters and high-kinetic energies is then accelerated towards the substrate, which is placed on a substrate holder in the target chamber.

2.4 GCIB and Surface Modification

GCIB is capable of producing surface effects that are distinctly different from other ion beams and plasma methods. Cluster ion impacts are different from monomer ions. Cluster ion beam has commercial applications in semiconductors, data storage and photonics. With advances in process integration and machine technology. GCIB has proved to play a great role in the industry in manufacturing devices requiring high throughput. Some unique characteristics of gas cluster ion beam bombardment in surface modification [29-31] is high sputtering yield, shallow implantation, surface cleaning and smoothening, uniform etching, surface erosion and thin film formation.

2.4.1 Surface Cleaning and Smoothing

Cluster ion beam with an inert gas source produces huge sputtering effects which are useful in smoothening and cleaning on atomic level [21]. Surface impurities can be effectively removed using GCIB. A high-removal rate together with low-surface damage effect has been a big advantage of a cluster ion beam. Surface smoothening is attributed primarily to the lateral sputtering of the target atoms at the impact site.

This is an important characteristic of the cluster ion beam which is not associated with any other molecular or atomic ion beam processes. GCIB possesses the ability to enhance the surface quality of most materials, such as glass, metals, and diamonds. GCIB shows excellent ability to smooth even to sub-nanometer levels. It typically removes a small amount of the target surface material and offers an effective way of producing superior surfaces on materials. Figure 2.3 shows an AFM image of a Ni-Fe film treated by Ar GCIB system [21].

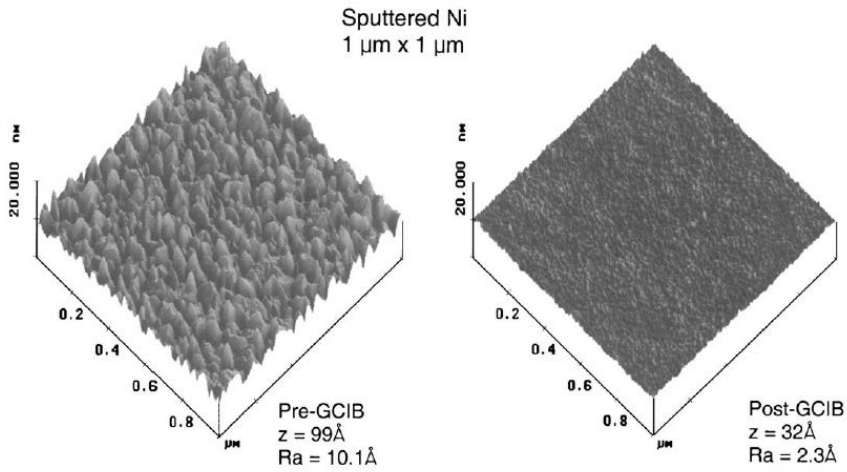

Fig. 5. AFM images of sputtered NiFe film smoothed by GCIB.

Figure 2.3: AFM images of GCIB treated NiFe film [21].

2.4.2 Surface Etching

GCIB can be used for very uniform and controlled etching over a full area substrate. With the inclusion of halogen compound in the argon gas source, the GCIB ability of chemical interaction with the target is strongly enhanced and it can produce a highly efficient and reproducible high-rate etching. Studies show that by addition of a halogen compound in the argon gas source the rate of surface removal can be

greatly increased [21]. Figure 2.4 shows a reduced thickness of a SiO_2 layer on a 200 mm silicon wafer from 526 nm to 347 nm using GCIB for etching.

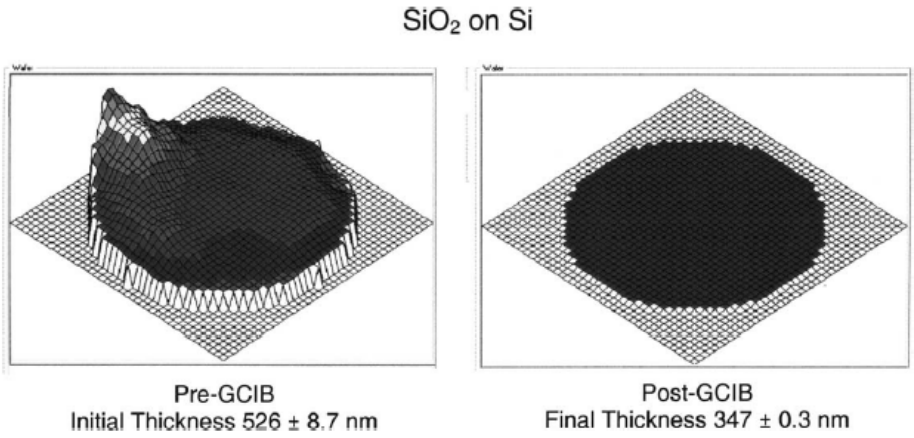

Figure 2.4: Shows GCIB etching of SiO_2 layer (dark shade indicates the surface of the SiO_2 layer) on a silicon wafer.

2.4.3 High Sputtering Yield and Shallow Implantation

Cluster ion implantation results in shallow penetration and high sputtering yield than a monomer ion beam [19, 20]. Argon monomer ions show less penetration in the solid material with the cluster ion beam. Each cluster is about a few thousand Ar atoms. With the same total energy, the thickness of the damaged layer by the Ar cluster ion beam is much shallower as compared to the Ar monomer ion implantation.

2.4.4 Thin Film Formation

Sputtering causes unnecessary damage in the targets and electrodes in the experimental equipment such as microscopes and ion sources. However, it has found to be a very useful phenomena in many techniques and applications in the

manufacturing industry including thin film deposition. High sputtering yield plays an important role in improving the throughput. High density bombardment with low energy cluster ions can modify thin substrate surface layers. Gas cluster ions have a strong chemical reactivity [20].

2.4.5 Surface Nano-ripple Formation

Cluster ion beam sputtering of solid surfaces can be used to form self-assembled nano ripple or nano dot structures at oblique angle incidences [32-33]. A nano-ripple pattern is formed due to lateral sputtering of the surface atoms when a cluster beam hits the substrate thousands of very-low-energy atoms (several eV per atom) simultaneously bombard at the same location on the surface of a target at an incidence normal to the surface of the target and goes through a series of multiple collisions. The relation between sputtering yield and the surface morphology can be determined by varying the incident angle of the cluster beam. The details of the description of nano ripple formation by GCIB irradiation is explained in the next chapter.

Chapter 3

Metallic Nanostructure for Plasmonic Applications

Numerous nano-fabrication techniques are utilized in synthesizing nanostructures for utilization of the LSPR effect [34]. Wet chemical reduction is an attractive method for synthesizing noble metallic (Au and Ag) nano particles of dimensions required for LSPR applications. Because of the face centered cubic crystallization of many metals, in this approach, the nano particles inherently crystalize into a truncated octahedron shape. However, surfactants and stabilizing agents added to the reactants allow engineering of different shapes and morphology by promoting preferential growth along certain crystal facets [35]. Wet chemical reduction synthesis has the advantage of large scale and relatively rapid synthesis. However, it is impaired in reproducibility and ability to fabricate substrates with immobilized ordered nanostructure arrangements. Another attractive approach is to promote plasmonic metal nano-particle growth in a solid solution, where the metal is infused into a solid substrate by means of ion implantation to reach a concentration exceeding the solid solubility of the metal in the substrate [36, 37]. Nano-particles formed in this process are inherently immobilized in the solid substrate with high spatial propinquity and therefore, these composites are also effective as surface enhanced Raman spectroscopy (SERS) substrates [38].

Lithographic techniques are attractive in achieving size and shape control of plasmonic nanostructures. Fabrication of nano structures via electron beam (EB) lithography and focused ion beam lithography allows high resolution and precise control of size, shape, and spatial distribution of nano structures [34, 39, 40]. Despite their advantages, they suffer from being slow processes and are limited to relatively small area fabrication [39]. Nano sphere lithography offers a cost effective method to produce large area 2D periodic arrays of plasmonic nano structures [41, 42] that are also effective SERS substrates. Alterations to fabrication methodology of nano sphere lithography allows fabrication of nano structure morphologies that include nano disks, nano rings, nano holes, and even cup-like structures [43]. Nanoimprint lithography can be considered to be a next generation lithographic technique that offers high precision comparable to EB lithography, while offering high throughput suitable for large-scale patterning [34,39]. This method allows finest lithographic resolutions, however, limited by the resolution of mask fabrication [34]. Some attractive and effective alternate approaches include the fabrication of metallic plasmonic resonators by nano skiving of chemically synthesized micro-plates of gold [44, 45]. In this approach, microplates of metal (gold) of nano-scale thickness are embedded in epoxy, and then sliced along with epoxy via nano skiving. This forms nano wires of well-defined dimensions that act as plasmonic resonators and plasmonic waveguides. One attractive feature is that when deposited microplates are single crystalline, the structures themselves become single crystalline, making them low-loss plasmonic resonators. The

approach, however, is a multiple step process and is unable to produce large area nano structure arrays.

Systematic laboratory procedures with cleanroom techniques do produce effective plasmonic structures, however, industrial applications such as large-area photovoltaic module production requires inexpensive and scalable techniques for controlled fabrication of metal nano patterns [46]. Simple methods to achieve this include thermal evaporation of a thin metal film on to a substrate and heating at a moderate temperature (200–300 °C). This causes agglomeration of the metal film by surface tension that forms a random array of nanoparticles with more regularity achievable by evaporation through a porous membrane (for example porous alumina) [47-49].

3.1 Plasmonic Nanostructure by GCIB Irradiation

To compliment such large-area high-throughput fabrication methods, in this chapter we discuss a method to fabricate plasmonic nano-arrays by oblique angle gas cluster ion beam (GCIB) irradiation of gold surfaces. Our method is a single step process with high throughput and the capability to produce large-area fabrication (200 mm wafer processing with commercial cluster ion implanters). Further, as any ion irradiation process this method produces minimum contamination since it does not involve any chemical processes. The fabrication method is further reproducible, and can be applied to many different starting materials that include metals and non-metals [50-52].

Cluster ions are charged, bound units of thousands of atoms. Energetic flux of cluster ions makes a cluster ion beam. Interaction of cluster ions with a solid is significantly different from how monomer ions interact with a solid. This is because of comparatively very low kinetic energy per constituent atom of a cluster ion and the synergetic reaction caused by the simultaneous arrival of thousands of constituent atoms of a cluster at the target with high spatiotemporal propinquity [53, 54]. The resulting nature of cluster ion-solid reactions is ideal for controlled surface modification. Gas cluster ion irradiation at normal incidence to a surface is widely used in research and industry for atomic scale smoothing of surfaces [53, 55, 56]. In contrast, GCIB irradiation of surfaces at an oblique angle roughens a surface, under proper conditions, producing self-assembled periodic nano-scale ripple arrays that closely resemble aeolian sand-ripples [33,51, 52]. Our approach utilizes this self-assembly process in order to fabricate metallic plasmonic nano structure arrays. Interestingly, with our approach, it is straightforward to control the scale and the separation of the nano-ripple structures, for example in this case of gold, to be in the range that exhibit LSPR in the visible range. In our experiment we irradiate a thin plain gold surface with ionized clusters of argon gas. Argon being an inert gas does not react with the surface and forms a one dimensional gold nano-ripple pattern due to sputtering of the gold atoms at the surface [33]. The nano-ripple wavelength depends on the number of clusters hitting the surface per unit area (centimeter square). By varying fluence of these clusters we obtain nano patterns of different sizes. In this chapter, we report the variation in the localized surface plasmon resonance frequency with the change in dimension of the gold

nano-ripples and the polarization dependence of the plasmonic response of these nano-ripples on the incident electric field vector due to their one dimensional structure.

3.2 Fabrication of Nano Ripple Array

We fabricate nano-ripple structures on gold surfaces (100 nm thick gold film on silicon obtained from Sigma Aldrich) by means of oblique angle irradiation (see figure 3.1) by 30 keV Ar GCIB (with 3000 mean Ar atoms per cluster ion) using an Epion cluster ion implanter. In order to control the geometry of the nano-ripple structures for the purpose of tuning the LSPR resonance frequency, we change the GCIB irradiation fluence as the variable parameter. For the cases discussed, at a base angle of incidence of 60 degrees, we irradiated the gold surface with different GCIB fluence of 1×10^{16} clusters/cm^2, 2×10^{16} clusters/cm^2, and 4×10^{16}clusters/cm^2. The cluster ion beam flux is approximately 3.9×10^{12} clusters/cm^2/sec and was kept constant. The variation of irradiation fluence affects the self-assembly process such that geometric parameters of the ripple arrays vary, which subsequently determined the LSPR resonance frequency. We have chosen the mentioned incident angle because it is within the ideal range of irradiation angles for the nano-ripple formation process [33]. The same holds true in our choice of the range of irradiation fluence, for example, below our choice of the lowest fluence of 1×10^{16} clusters/cm^2 nano-arrays lose their periodicity. At the fluence of 4×10^{16} clusters/cm^2 the separation between the individual nano ripple saturates. As we increase the fluence beyond this point, height of the ripples starts reducing and an increase in the fluence

does not increase the plasmon resonance frequency. The detailed mechanism of GCIB induced ripple formation and the reasons for these lower and upper bounds are explained in detail by Tilakaratne et al. in reference [33].

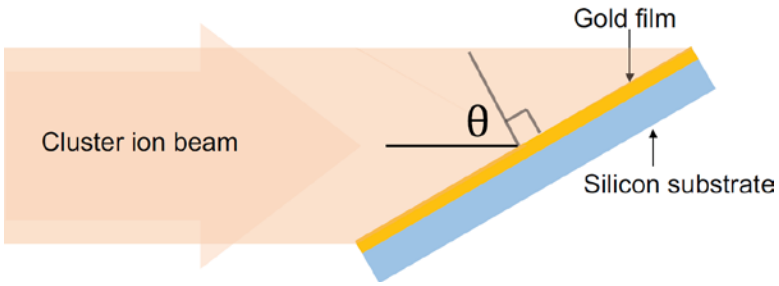

Figure 3.1: A schematic of oblique angle gas cluster ion beam (GCIB) irradiation configuration used in fabrication of nano ripple array structures. In this case presented, a 100 nm thick film of gold on silicon is irradiated with argon GCIB. θ is the angle of incidence of GCIB irradiation.

Figure 3.2a and 3.2b show scanning electron microscope (SEM) images of the nano-ripple arrays fabricated under selected conditions of 4×10^{16} clusters/cm^2 GCIB fluence, and 60 degrees GCIB incident angle. Tilted view in figure 3.2b shows that the cross-section of ripples are shaped up as *curved walls* forming a cavity between one side of the wall and the gold substrate. Rutherford backscattering measurements of the average thickness of the remaining gold layer confirmed the silicon substrate is not exposed after irradiation. Detailed description of gold nano-rippled surfaces that cover the rest of the fabrication conditions discussed in this chapter can be found in references [33] and [57]. Here, we discuss LSPR of these nano-ripple structures relating it to the geometry of the rippled surfaces that depends on the fabrication conditions. As parameters that characterize the geometry, we use the ripple height (h), and the ripple periodicity

(l) (average peak to peak distance of the periodic ripples) as acquired by atomic force microscopy.

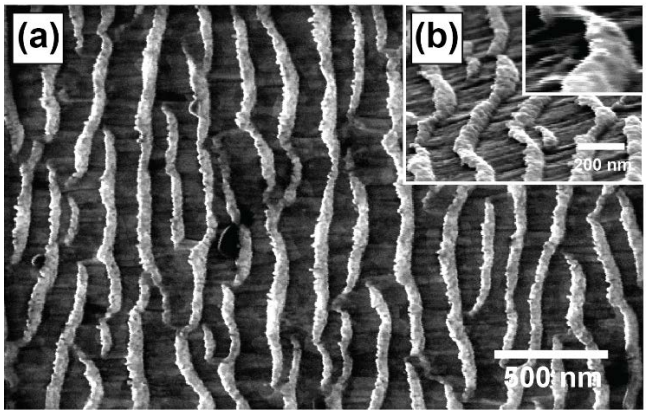

Figure 3.2: (a) SEM top view image of the nano-ripple array on gold surface obtained for GCIB irradiation fluence of 4×10^{16} clusters/cm^2, for an incident angle of 60 degrees. (b) SEM image with the substrate tilted 70 degrees for better visualization of the cross-section of the ripples.

3.3 Optical Characterization and LSPR

We will briefly discuss the localized surface plasmon resonance (LSPR) effect from the gold nano ripple pattern. When white light falls on a plain metal surface, at a particular frequency, the electric field E of the incident beam and the electric field of the free conduction electrons inside the metal couple with each other. The coupling gives rise to huge charge density fluctuations which travel along the metal-dielectric interface. The quanta of these oscillations is called the surface plasmon. When the dimension of the metal is reduced to nanoscale and the wavelength of the incident light is larger than its dimension, the free electrons inside the metal nano particle show plasmonic oscillation at the resonant frequency

under the influence of the incident electric field and give rise to standing waves due to its confined size. These are confined surface plasmon and this effect is called localized surface plasmon resonance (LSPR). However the structure under discussion is not a nano particle. It is a one dimension nano-ripple pattern of gold. Thus by changing the polarization of the incident electric field on these structures the intensity of the LSPR peak will vary which explains the polarization dependence of their plasmonic behavior.

In obtaining optical spectra, we illuminate the nano-rippled surfaces with linearly polarized, focused, white light from a high-intensity tungsten light source as shown in figure 3.3. The incident beam of light is perpendicular to the metal surface with the polarization perpendicular to the length (larger dimension) of nano-ripples. Diffuse light scattered off the surface is acquired and guided through an optical fiber and analyzed using an optical spectrometer.

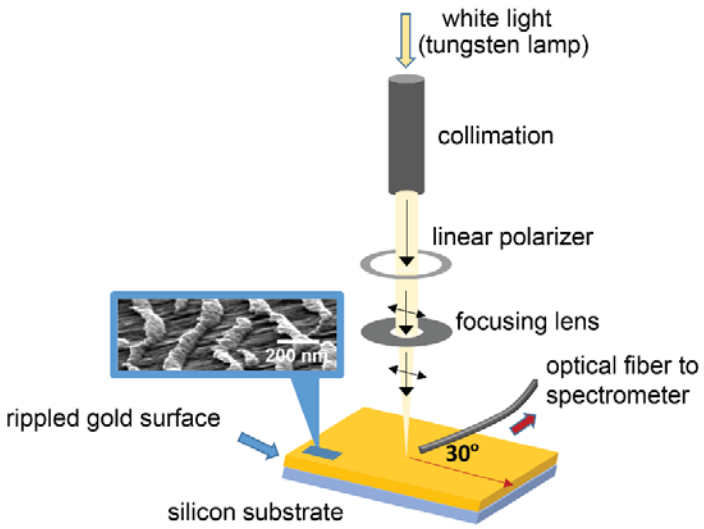

Figure 3.3: Experimental arrangement used for measuring optical diffuse scattering from nano-rippled gold substrates.

Figure 3.4a shows optical scattering spectra of rippled surfaces fabricated by GCIB irradiation at fluence of 1×10^{16} clusters/cm^2, 2×10^{16} clusters/cm^2, and 4×10^{16} clusters/cm^2, for GCIB incident angle of 60 degrees. The enhanced optical scattering peak caused by LSPR of the nano-ripple structures is prominent in these spectra. Figure 3.4b and 3.4c show the variations of nano-ripple height and ripple periodicity that correspond to the peaks of the scattering spectra. The LSPR scattering enhancement is observed when the surface component of the polarization of incident light is perpendicular to the length of the ripple structures, and is suppressed when the polarization is parallel to it as is indicated in the insert of figure 3.4a. The suppression as expected occurs due to the electric vector of the incident beam being parallel to the length of the ripple structure that is significantly larger in dimension than the width.

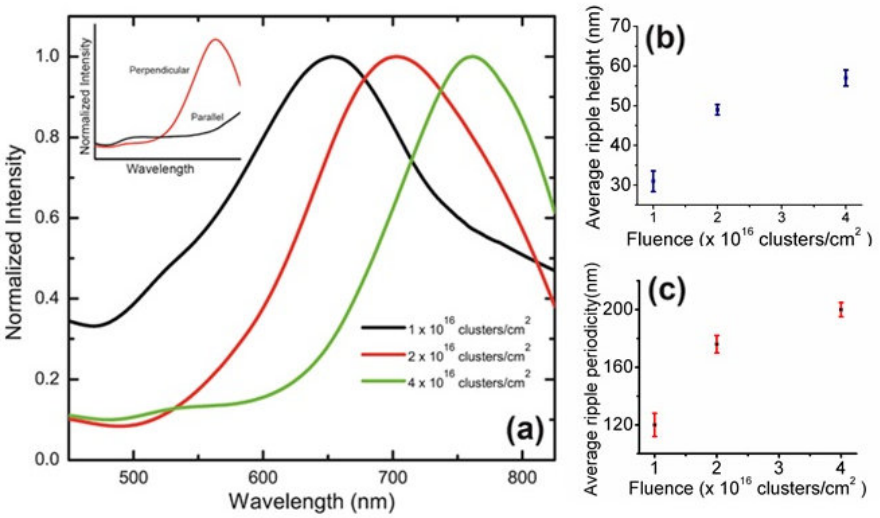

Figure 3.4: (a) Optical scattering spectra of gold nano-ripple array surfaces fabricated by GCIB irradiation at fluence of 1×10^{16} clusters/cm^2, 2×10^{16} clusters/cm^2, and 4×10^{16} clusters/cm^2, for a GCIB incident angle of 60 degrees. Spectra clearly show the enhanced scattering peak due to LSPR of the nano-ripples. The insert shows a comparison of spectra for surface component of polarization of light perpendicular and parallel to the length of ripples showing that LSPR occurs when the polarization is perpendicular to the length of ripples. The frequency of resonance can be effectively changed by changing the GCIB irradiation fluence in fabrication. (b) Variation of average ripple height and (c) average ripple periodicity with respect to GCIB fluence, obtained via atomic force microscopy.

AFM images of these nano ripple structures are shown in figure 3.5 and the process of ripple formation is explained in detail in reference [33]. By changing the irradiation fluence in fabrication (for 60 degree GCIB incident angle), the LSPR wavelength in the nano-ripple surfaces can be changed in a considerable range of 653 nm to 761 nm. Certainly, although we have limited the selection of fluence used for the purpose of this study that is primarily a proof of concept, larger control can be achieved by a much finer selection of irradiation fluence. In addition, the

dimensions of the nano ripple structures can be tailored by changing the GCIB angle of incidence [51] as an additional potential parameter for LSPR control.

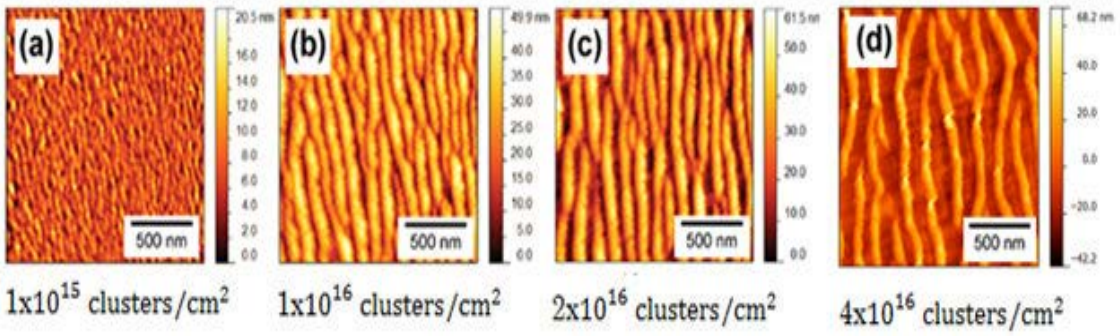

Figure 3.5: (a) (b) (c) and (d) are the AFM images of gold nano-ripples fabricated by ion fluence of 1×10^{15} clusters/cm^2,1×10^{16} clusters/cm^2, 2×10^{16} clusters/cm^2 , and 4×10^{16} clusters/cm^2 respectively.

As mentioned earlier the shift of the LSPR resonance wavelength is caused by the variation of the geometry of the ripple arrays. In case of molding of ripple geometry by varying the GCIB irradiation fluence, it is notable (Figure 3.4b and 3.4c) that the average ripple periodicity increases with increasing irradiation fluence, in this case from 120 nm to 200 nm when the fluence is increased from 1×10^{16} clusters/cm^2 to 4×10^{16} clusters/cm^2. Along with that, in the same range of fluence the average ripple height varies between a minimum of 30 nm and 60 nm. The red-shift of the LSPR resonance frequency can be qualitatively described as being caused by the increase of ripple height perturbed by increase of ripple periodicity within this

range of fluence. However, the complex cross-section shape of the ripples, including the curvature and the cavity observed in SEM imaging (Figure 3.2) was not quantified in this work and may affect the LSPR resonance frequency. Therefore, we have not yet established a functional relationship between the GCIB irradiation conditions, ripple dimensions, and the SPR resonance wavelength in this chapter. Further analysis is needed in developing this relationship. The SPR resonance wavelength is however, reproducible with the same GCIB irradiation conditions.

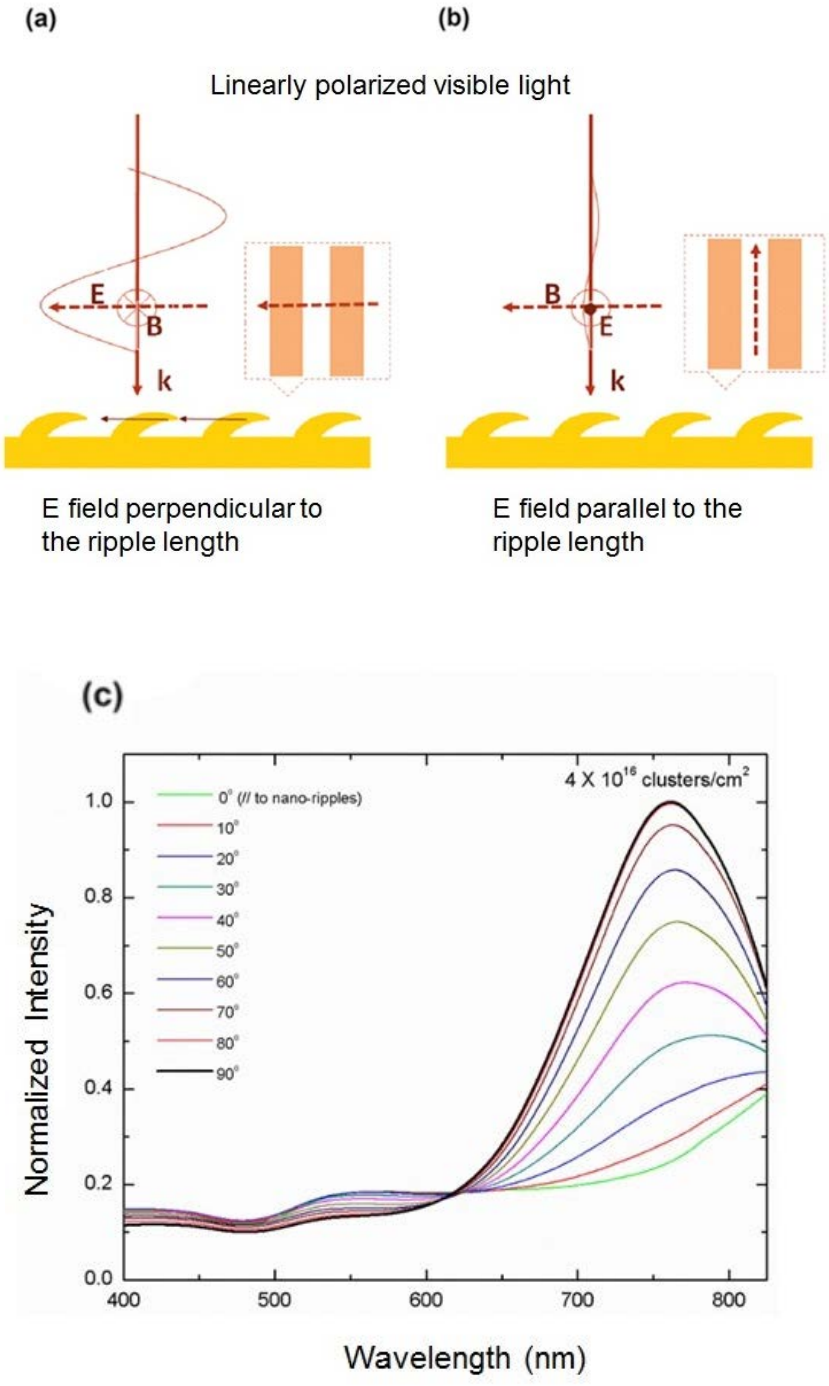

Figure 3.6: The polarization dependence of the plasmonic property of the nano ripples array surface is addressed. (a) Explains the LSPR effect occurs when the incident E field is perpendicular to the ripple array. That is when the wavelength of the incident E field is larger than the cross section of the ripples. In the scattering

spectrum, a huge peak in the intensity at the resonance frequency is observed. (b) Shows there is no resonance effect when the incident E field is parallel to the ripple pattern. (c) Shows the drop in the intensity as we change the polarization angle from 90 degrees to 0 degrees for the nanostructure of 4×10^{16} clusters/cm^2 fluence.

The intensity at the resonance wavelength varies with the polarization of the incident electric field vector (Figure 3.6). The intensity is highest when the ripple pattern is perpendicular to the incident E field. For LSPR to occur, the wavelength of the beam must be larger than the dimension of the ripples.

3.4 Plasmonic Behavior of the Nano-Ripple Gold

We did a comparative study of the plasmonic properties of the nano-ripple array generated by three different fluence of the cluster ion beam with intensities 1×10^{16} clusters/cm^2, 2×10^{16} clusters/cm^2, and 4×10^{16} clusters/cm^2. Below the fluence of 1×10^{16} clusters/cm^2, the surface did not establish periodicity in its pattern. As we increase the fluence, the structure starts to attain order. At the fluence of 1×10^{16} clusters/cm^2, we observe the LSPR peak in the spectrum but the spectral curve was broad. The broadening of the scattering spectrum indicates that the structure is not well-ordered and thus the LSPR peak is not very sharp. We use this fluence as the lower bound for our studies. As the fluence increases, the structures begin to become larger and periodic. At 2×10^{16} clusters/cm^2 and 4×10^{16} clusters/cm^2 we achieve a relatively uniform and ordered nano-ripple pattern. As can be seen in the AFM image in Figure 3.5.

The scattering spectrum is narrower for the fluence of 2×10^{16}clusters/cm^2 and becomes sharper when we increase to 4×10^{16}clusters/cm^2 as the structure become larger and uniform with the increased fluence. The plasmon resonance frequency is different for different dimensions of the ripple patterns. The experiment indicates that as the structure gets bigger, the corresponding resonant frequency gets larger.

We plotted the normalized intensity as a function of LSPR wavelength for the three different fluence in figure 3.4. The peak for the smallest fluence occurred at 653 nm (black line), the medium fluence (red) at 700 nm and the highest fluence (green) at 762 nm showing the relation between the LSPR peak and the nano ripple dimension. The increase in the fluence from 1×10^{16} clusters/cm^2 to 4×10^{16} clusters/cm^2 increases the size and the separation between the nano ripples and the corresponding LSPR wavelength from these structures accordingly increases.

The plasmonic response of the nano-ripple structure is polarization dependent because of their one dimensional nature unlike the nanoparticles. When the incident light is perpendicular to the structures, we observe the maximum intensity in the LSPR resonance peak (Figure 3.6a). Changing the polarization will decrease the intensity gradually (Figure 3.6c) and with E field parallel to these nano structures we observe no resonance at all (Figure 3.6b).

3.5 Advantages for Plasmonic Applications

Self-assembly induced by oblique angle cluster ion beam irradiation of metal surfaces is a high-throughput, single-step method for fabricating rippled plasmonic nanostructure arrays. This approach does not require lithographic or chemical

processes and has the prominent advantage of possible large surface area coverage and applicability to different starting materials. The polarization dependent plasmonic property of the gold nano-ripple is due to their one dimension structure. The localized plasmon resonance frequency of synthesized *nano-ripple arrays* is tunable by changing nano-ripple dimensions that can be engineered by changing the cluster ion beam irradiation parameters. The outcome, along with this single step, cost-effective, large area GCIB based fabrication method is promising for the use of these nano-ripple arrays in plasmonic applications.

Chapter 4

Bio-molecular Sensing Application of Gold Nano Ripple Structure

There is a growing interest in developing nano-biosensors with high sensitivity and selectivity in the scientific community due to its various advantages [58-59]. The localized surface plasmon resonance (LSPR) based sensors offer the benefit of low cost instrumentation, label-free detection, high sensitivity, specific selectivity and easy configuration in addition to its ability of real time detection [18, 7, 60]. These optical nano biosensors have proved very useful in applications in wide range fields such as drug screening, DNA recognition, environmental monitoring, and various chemical and biomolecular detection [61, 62]. Researchers currently are investigating ways of developing an LSPR based sensor with better performance. The most common method that the scientists have employed is building the nano sensor by chemically immobilizing metal nanoparticles on a functionalized optically transparent surface [63] and using an optical transducer that can translate the biomolecular interaction into a quantifiable signal in order to detect the specific biomolecule [60]. The unique optical property and bio-compatibility of gold has encouraged scientists to utilize it for biosensing applications [64-65]. We have demonstrated an LSPR based gold nano-ripple biosensor that is produced in a single step process using gas cluster ion beam (GCIB) system [51, 33, 52].

In the recent years the increase in nano-scale applications has created significant interest in self assembled pattern formation due to ion beam irradiation. Nano-patterning and modifications require nuclear collision between ions and substrate atoms in less than 100 eV energy range. Compared to monomer ion beams the cluster ion interactions with the surface produces unique structural alterations because of their capability to deliver a very low particle energy beam (a few eV's) with high current density. Upon impact the cluster ions [27] simultaneously arrive at the same location and transfer their high total energy to a small impact volume (of the order of a tens of angstroms). Due to high energy density collisions, extreme pressure and temperature conditions are generated. Consequently, dissociations close to the surface create synergetic reactions that produces a high sputtering yield and strong enhancement in chemical reactivity and diffusion.

4.1 Theory of Ripple Formation and Mechanism

Gas cluster ion beam forms nano-ripple structures on a thin metal surface at oblique angle incidences [66]. When thousands of very low energy atoms simultaneously bombard the surface of a target at an inclined angle to the normal, a nano-ripple pattern is formed because of the lateral sputtering of the surface atoms. Cluster formation is a complicated process and the theoretical descriptions of this process are limited. First model explaining ripple formation and mechanism was derived by Bradley and Harper [26] on solid materials. It predicts the linear growth of ripples, but does not predict ripple saturation. The Makeev, Cuerno, and Barabási (MCB) model [67] modified the Bradley and Harper model and included the non-linear

terms that depend on the random ion flux and the slope of the surface and considered effective ion-induced diffusion rather than isotropic thermal diffusion. Most theoretical calculations of ripple formation illustrate coupling of mobile surface atoms and monomer ions.

4.2 Nano-ripple LSPR based Biosensor

LSPR based gold nano ripple biosensor has the benefit of low cost of fabrication, real-time monitoring capability, and large surface area coverage for label-free biosensing purposes. The light scattered from the metal nano structure show a peak intensity at the resonant wavelength of the nano ripples depending on their dimensions [66], where it couples with the electric field of the incident light (Figure 4.1a). The nano ripple pattern act as a probe for the detection of biomolecules immobilized on the surface by sensing the change in the dielectric environment and altering the resonant wavelength [68-69]. The LSPR peak shift acts as a biomarker that identifies the specific biomolecule attachment [70].

The nano-gold surface can be functionalized by thiolated organic compounds due to the strong affinity of gold to the thiol group of these compounds. The property of gold to make a strong bond with a thiol group of organic compounds enables it to achieve stable and uniform monolayer of these organic compounds on its surface. This monolayer can act as a cross-linker for binding antibodies or other receptors and make them sterically accessible for the target antigens or ligands as illustrated in Figure 4.1b and thus can be used for studying antibody-antigen reaction dynamics [71-72] by detecting the change in the LSPR resonance wavelength due

to adsorption, dissociation and regeneration of the surface in real time as shown in figure 4.1c and various other such mechanisms.

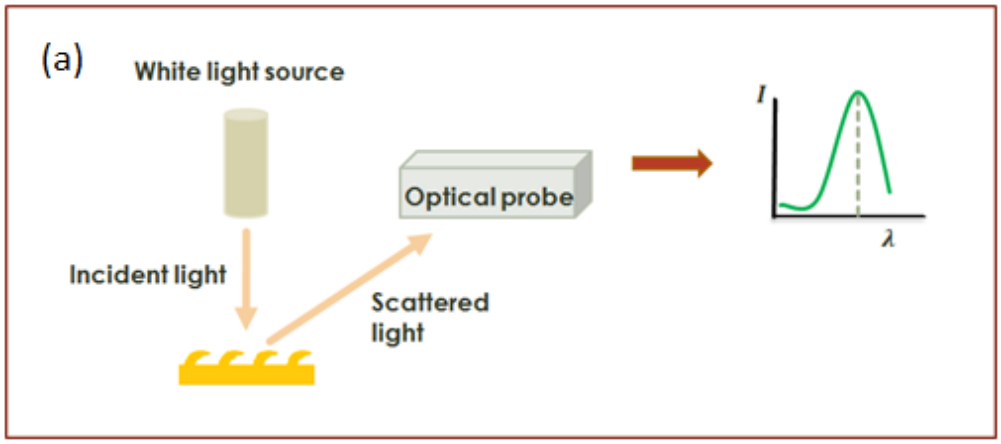

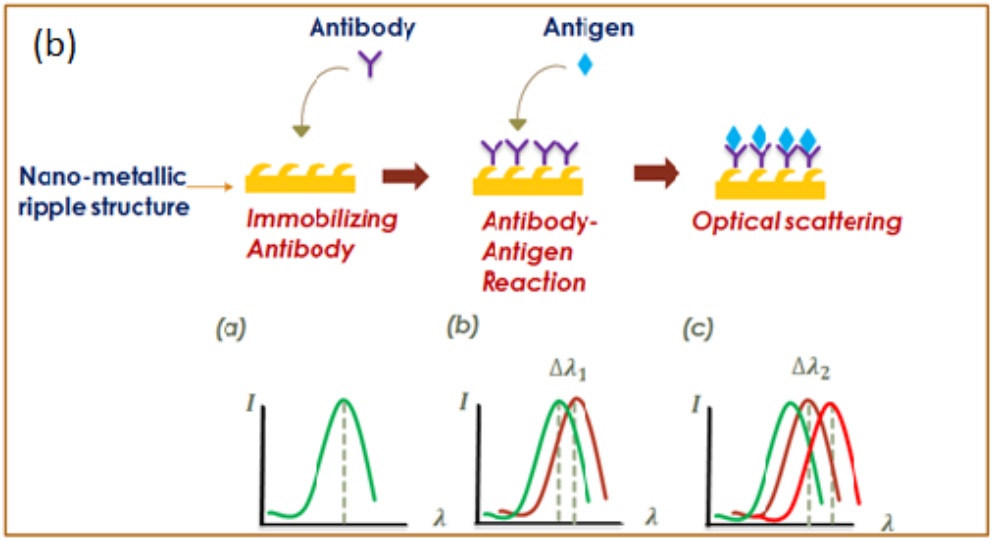

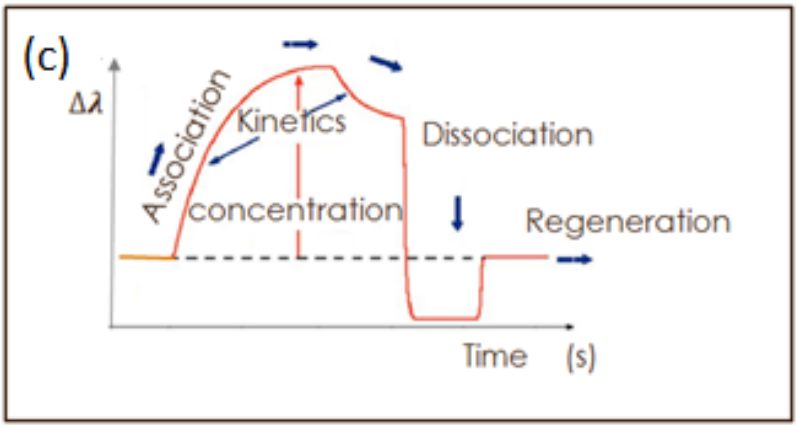

Figure 4.1: (a) A schematic diagram illustrating that the light scattered by the gold nano-ripple pattern shows peak in the intensity at the LSPR wavelength in the scattering spectra collected by the spectrometer. (b) A schematic diagram showing how the technique can be used for antibody-antigen reaction study. When the antibody is immobilized on the surface it changes the LSPR wavelength due to the change it creates in the dielectric environment. If the antibody happens to exist in a system with its specific antigen, the antigen binds on the antibody sites and causes another shift in the scattering spectra. If this change in the spectral peak is studied in real time a graph such as the one shown in (c) is obtained which explains the antibody-antigen reaction mechanism.

In this chapter, we show the dependence of LSPR spectral peak on the nano ripple dimension and its saturation point, and the bio-compatibility of the nano-ripple gold substrates for bio-sensing applications using various simple organic compounds with thiol groups indicating the potential of this LSPR-based sensor for future studying ligand-receptor binding, antibody-antigen reaction dynamics, adsorption, and dissociation kinetics, drug delivery, protein-DNA interaction, and various bio-reaction studies using real time detection technique.

By studying reaction dynamics, the rate at which the body responses to a certain drug can be understood, which plays a significant role in designing drugs and studying their effects. Researchers are developing biosensors with improved

capabilities of diagnosis and monitoring of diseases and drug delivery. Our LSPR based sensor has a sensitivity of 266.66 nm/RIU. With increased control and uniformity of the nano-rippled gold structure, we believe we can make it a useful and reliable technique for biosensing purposes.

4.3 Experimental Procedure and Setup

Figure 4.2 shows our experimental setup. A white collimated beam of light passes through the polarizer and is focused on the gold rippled samples. The scattered light is captured by the spectrometer through the optical fiber and reads the intensity spectra vs the wavelength of light. In this setup we use the microscope to make sure every time we take the spectrum at the same point on the sample to maintain the uniformity of our reading and have a fix reference point.

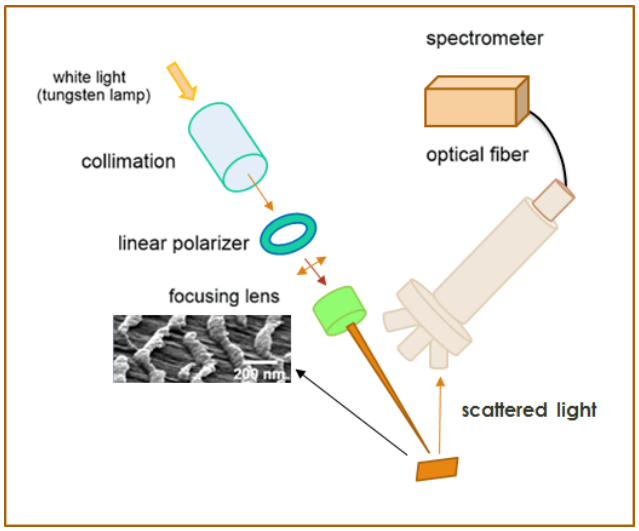

Figure 4.2: Experimental setup used to collect scattering spectra from the gold nano-ripple structures.

The scattering spectra from the structure formed by the fluence of 2×10^{16} /cm^2 of the argon gas clusters gives a peak in the intensity at the resonant wavelength. By changing the polarization of the incident electric field from 90 degrees to 45 degree and then to 0 degrees we recorded the change in the spectral resonance intensity in order to observe the polarization dependence of the LSPR spectral peak, Figure 4.3.

Figure 4.4b shows the AFM image of the one dimensional nano ripple pattern formed by the fluence of 1×10^{16} /cm^2, 2×10^{16} /cm^2, 4×10^{16} /cm^2, and 5×10^{16} /cm^2. The nano ripple dimension is modified by the change in fluence of argon clusters producing these nano-patterns. The LSPR spectrum from these nano structures is shown in the Figure 4.4a. In this chapter the resonance peaks for 1×10^{16} /cm^2, 2×10^{16} /cm^2, and 4×10^{16} /cm^2 are slightly different from the previous reported chapter [66]. This is because before we took the spectrum, the nano ripple surface was being sprayed by nitrogen gas to remove of any dirt on the samples and cleaned in UV-ozone cleaner for 15 min to avoid organic compound pre-attachment to ensure a sharp LSPR peak.

In order to measure the sensitivity of this optical nano-ripple gold biosensor, we studied the shift in the LSPR spectral peak with water and ethanol. Multiple secondary peaks were observed in the spectrum as seen in Figure 4.5. The sensitivity and biocompatibility of the nano metallic ripple surface has checked by introducing it to an organic compound with high affinity to gold. The cleaned ripple surface of 2×10^{16} /cm^2 nano-structure was functionalized with a mono-layer of 4-methyl-benzenethiol (4MBT) by dipping the sample in a 0.02 M of 4MBT solution

(0.285 gm of 4MBT in 10 ml of ethanol) for 2 h. It is then washed with ethanol to get rid of excess 4MBT in order to achieve a uniform and stable monolayer of 4MBT adsorbed on the nano-ripple gold surface and dried using nitrogen gas. A resonance shift of 26nm was seen with a mono-layer of 4MBT in Figure 4.6.

We repeated the same experiment on 1×10^{16} /cm^2, 4×10^{16} /cm^2, and 5×10^{16} /cm^2 nano ripple structures. In Figure 4.7 the shift in the plasmonic resonance wavelength was plotted in nanometers (nm) vs the fluence that determines the dimension of the structures. The plasmonic resonance wavelength shift with monolayer of octanethiol, dodecanethiol, and cystaemine hydrochloride is shown in Figure 4.8.

4.4 Working of the NR-Biosensor

LSPR spectral curve shows a peak in the intensity at the resonance frequency of the structures where the electric field of the oscillating conduction electrons inside the metal nano-ripple couples with the electric field of the incident light. The visible optical scattering spectra of nano-ripple gold substrate formed by the fluence of 2×10^{16} /cm^2 shows LSPR peak at 674 nm. As we changed the polarization angle from 90 to 45 degrees, we saw a drop in the intensity peak at 674 nm and when the incident E field was parallel to the ripples at 0 degrees the LSPR peak disappears. Changing the polarization of the incident light will change the intensity gradually. With E field parallel to the ripple pattern, we observed no resonance at all. We have discussed this phenomenon in Chapter 3. LSPR depends on the polarization of the

incident beam and it disappears if the dimensions are larger than the wavelength of the incident electromagnetic light.

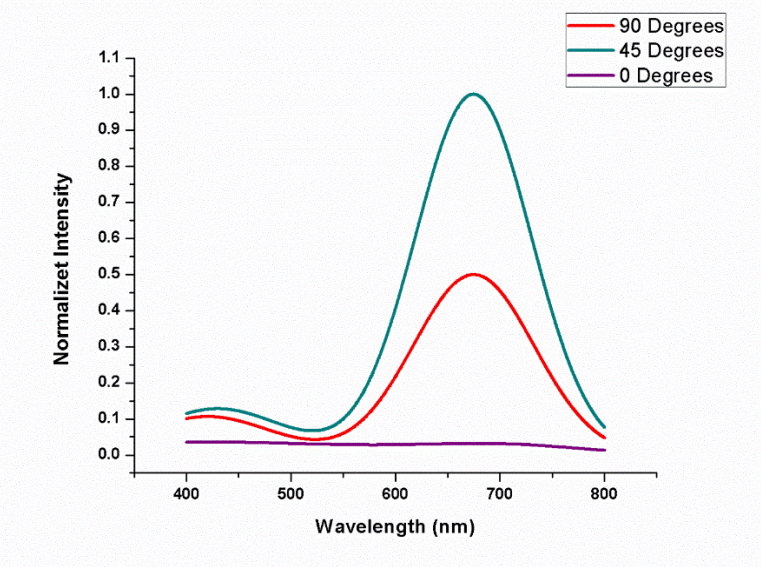

Figure 4.3: The visible optical scattering spectra of nano rippled gold substrate formed by the fluence of $2x10^{16}\ clusters/cm^2$. The LSPR peak occurs at 674 nm wavelength and by changing the polarization of the incident light we observe the disappearance of the peak when the incident electric field is parallel to the nano-ripple dimensions showing the polarization dependence of these nanostructures.

The LSPR wavelength peak is highly dependent on the fluence of the incident cluster ion beam since it determines the dimension of the nano ripple. The plasmonic behavior is extremely sensitive to the nano ripple size and can be modulated by changing the nano-ripple size, shape, the separation between the nanoripples, and the dielectric constant of the environment above the ripple surface [40, 41]. As we increase the fluence from 1×10^{16} /cm^2 to 4×10^{16} /cm^2 the width of the nano ripple increased as the AFM images indicate and the corresponding LSPR wavelength increased accordingly. However increasing the cluster fluence beyond

the fluence of 4×10^{16} /cm^2 showed that the wavelength of the nano-ripple did not increase further because the height of the ripple is decreased. This occur because of the sputtering of the gold atoms from the top of the nano-ripple due to constant bombardment.

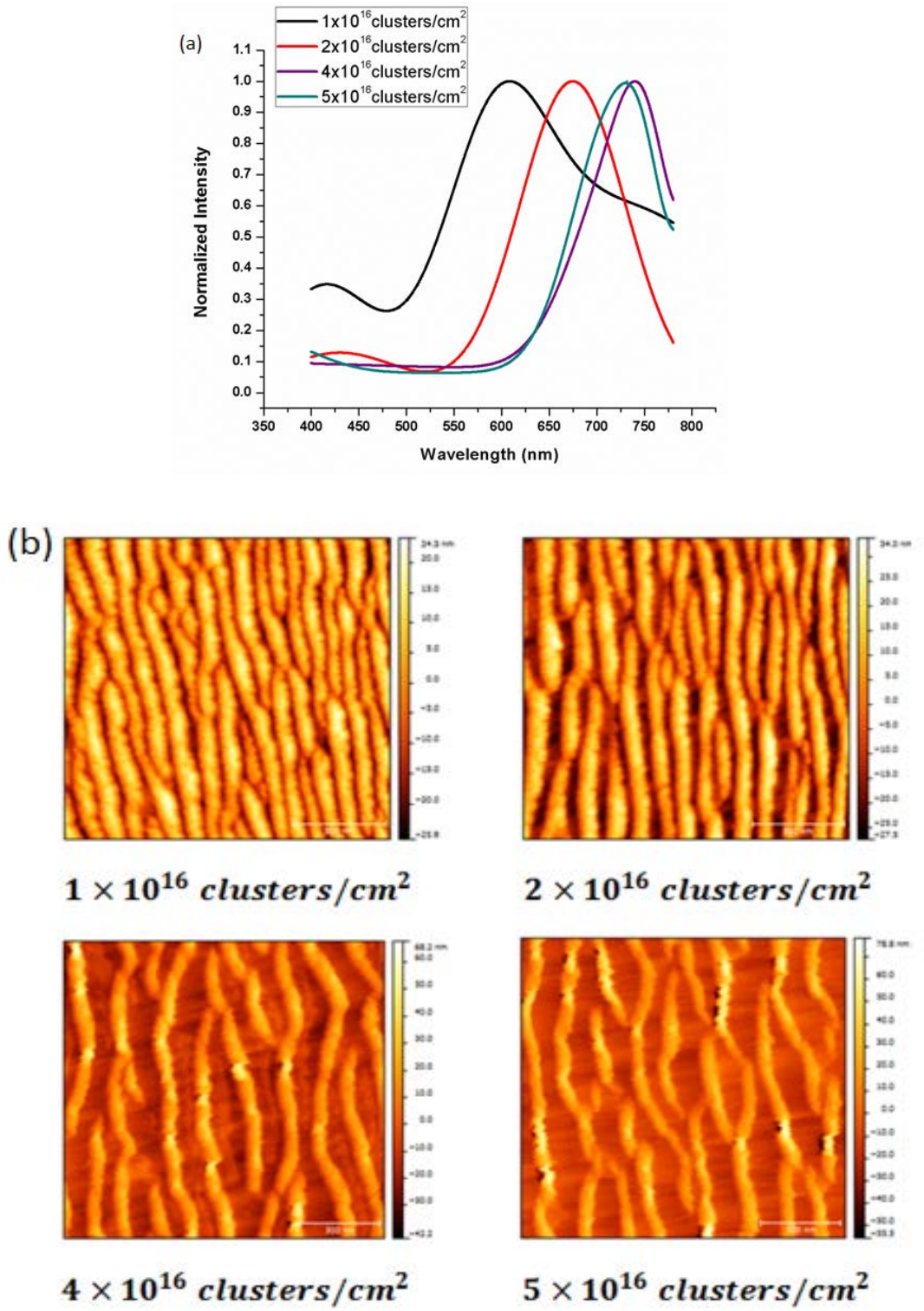

Figure 4.4: (a) The graph illustrates the fact that different dose of the gas clusters form nano-ripples of different dimension and thus the LSPR wavelength is different

for them. The AFM images of these structures are shown in (b). The average maximum height and root mean square wavelength of the profile of each nano-ripple structure is shown in the Table 4.1.

Table 4.1: The width and height of each of these nano-ripple pattern

Nano-ripple Doses (10^{16}clusters/cm^2)	Average maximum height of the profile (nm)	Root mean square wavelength of the profile(μm)
1	26	514
2	40	521
4	64	555
5	59	555

The LSPR for 1×10^{16} /cm^2 and 4×10^{16} /cm^2 occurs at 608 nm and 740 nm, respectively and for the fluence of 5×10^{16} /cm^2 the resonant wavelength did not increase but decreased to 731 nm due to the reduced height of the ripples. Thus there lies a saturation point. The width of the nano ripple does not increase beyond this point but rather reduces the height of the ripples when we keep on increasing the fluence due to sputtering.

We measured the shift in the LSPR peak from the nano gold ripples with water and ethanol and observed the sensitivity S [7] of:

$$S = \frac{\Delta\lambda}{\Delta n} = 266.66 \text{ nm/RIU}$$

Where RIU stands for refractive index unit. .

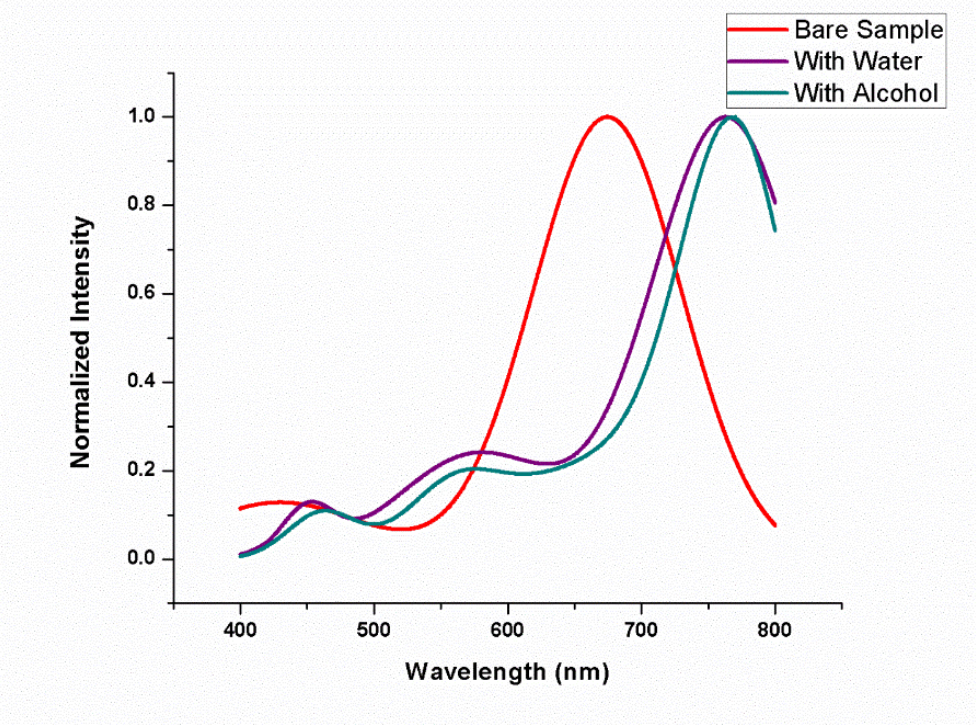

Figure 4.5: The shift with water and ethanol on nano rippled gold structure formed by the fluence of $2x10^{16}\ clusters/cm^2$. The sensitivity of this sensor is 266.66 nm/RIU.

Water with a dielectric constant of 1.33, shifts 88 nm in resonant wavelength and shows the spectral peak at 762 nm with small secondary peaks at 580 nm and 453 nm. These peaks indicate the presence of multiple resonances from the structure. The nano ripple does not have the same width in every dimension such as a sphere. Thus we expect multiple resonance. However, the occurrence of the secondary resonant peaks is prominent only when we put a dielectric on the surface and that is because of the enhancement in the electric field. A similar spectrum was obtained with ethanol of dielectric constant 1.36 units. We see a spectral shift of 90 nm with peak at 770 nm and secondary peaks at 576 nm and 463 nm.

We then tested this structure for bio sensing applications. In order to demonstrate the bio-compatibility of our sensor, we modified the gold nano ripple surface with a monolayer of 4MBT and observed the LSPR shift. Even with a monolayer of the organic compound, we observed the shift of 26 nm in the resonant frequency peak. It shows extremely high sensitivity of the LSPR from these structures that can sense changes to monolayer scale. These LSPR based sensors can be used as sensitive good probes for bio-sensing.

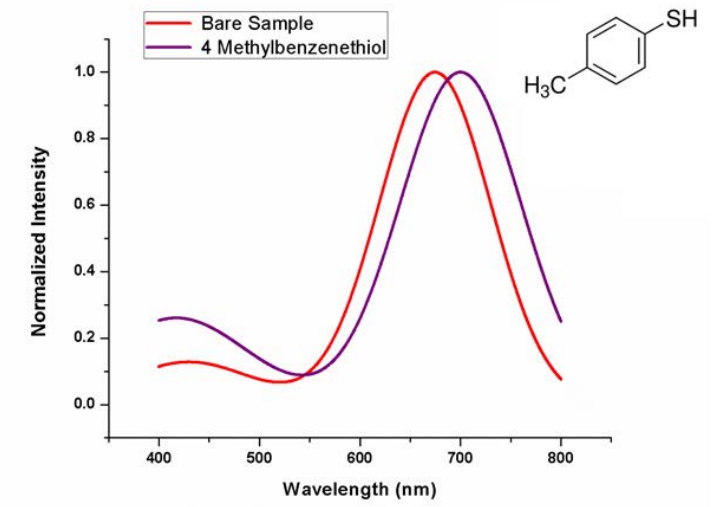

Figure 4.6: Monolayer of 4-methyl-benzenethiol (4MBT) on nano-ripple structure produced by the dose $2x10^{16}\ clusters/cm^2$shifts the LSPR peak to 26 nm.

Similar experiment was performed with 1×10^{16} /cm^2, 4×10^{16} /cm^2, and 5×10^{16} /cm^2 nano-ripple patterns and observed different shifts. We noticed that as we go from 1×10^{16} /cm^2 to 4×10^{16} /cm^2 the shift with the immobilization of a monolayer of 4MBT decreased with increased nano ripple width.

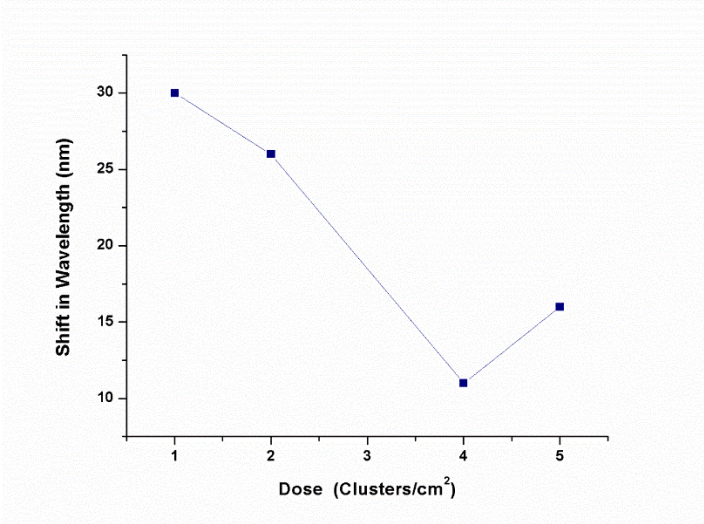

Figure 4.7: Plot of the shift in the wavelength caused by the monolayer of 4MBT on all four nano-ripple structures versus the fluence.

Table 4.2 shows LSPR peaks and the shifts that occur with the monolayer of 4MBT from the nano structures.

Doses (10^{16} clusters/cm^2)	Wavelength without 4MBT (nm)	Wavelength with 4MBT (nm)	Shift in Wavelength (nm)
1	608	638	30
2	674	700	26
4	740	751	11
5	731	747	16

If number of clusters of argon atoms falling on the structures per unit area is increased beyond 4×10^{16} /cm^2, the ripple height starts to reduce. The LSPR wavelength reduces and we see the shift in the peak increasing beyond this point. On the 2×10^{16} /cm^2 nano-ripple gold structure with the monolayer of adhesion of

octanethiol, dodecanethiol, and cysteamine hydrochloride the LSPR peak shift observed is 59 nm, 51 nm and 49 nm respectively.

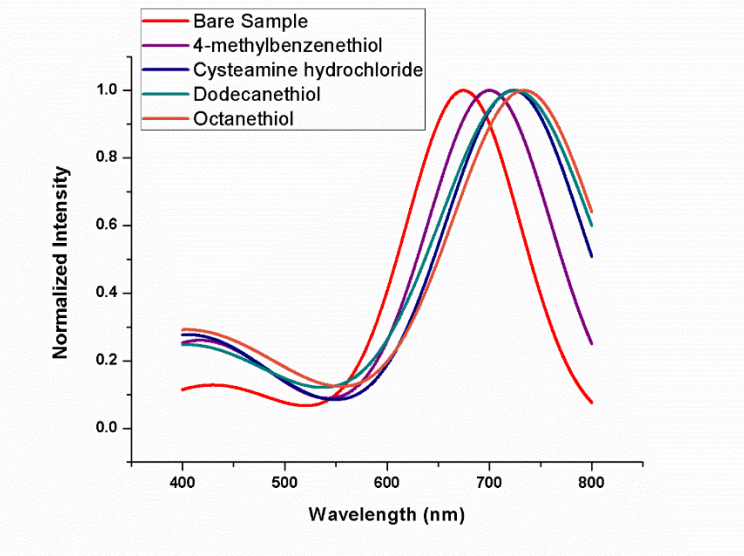

Figure 4.8: LSPR peak shifts with monolayer of 4MBT, octanethiol, dodecanethiol, and cysteamine hydrochloride.

4.5 Potential for Sensitive and Selective Biosensing

We introduce a simple and cost-effective scheme for bio-sensing using nano-ripple structures. Cluster ion beam synthesized self-assembled gold nano rippled structures have potential for plasmonic sensing applications. LSPR wavelength which is tunable based on the nano-ripple dimension reaches a saturation point in the fluence beyond which the resonant wavelength shows a decrease due to the reduced nano ripple height. These localized surface plasmon resonance based bio sensors not only are capable of label free real time analytical detection but also show high sensitivity. By adsorbing a mono-layer of thiolated organic compound

on the surface of these substrates we identified the shift in the localized surface plasmon resonance peaks triggered by the change of dielectric function in the neighborhood of the structures. These plasmonic nano-metallic structures can be utilized to observe the change of localized surface plasmon resonance frequency due to the cycle of adsorption, re-adsorption, and reactions taking place on the surface that can potentially be mapped in to reaction mechanics. The bio-sensor has monolayer molecule-coating sensitivity and specific selectivity. The application of this sensor can be extended to study antibody, antigen, drug delivery, bio-reaction, absorption, and dissociation kinetics. We also speculate the potential application, advantage of possibility of large surface area coverage and applicability to different starting materials.

Chapter 5

Detecting Antibody-Antigen Reaction using Nano Ripple Gold LSPR based Biosensor

The need to develop and design accurate and sensitive methods for detection of biological material is of great importance. A sensitive and quantifiable biosensing scheme is essential to detect and analyze disease-associated pathogens obtained from patients or in the environment. LSPR based sensors have the ability for a reliable and sensitive detection that can facilitate appropriate treatments. These sensors have applications in many fields including medical diagnostics, biomedical research, food safety, and environmental science [73-75, 61]. Unlike ELISA (enzyme-linked immunosorbent assays) or PCR (polymerase chain reaction), LSPR does not require a labelling or amplifying process. The study of binding kinetics in real time and continuous concentration measurement of the target molecules can be achieved on the sensor [76].

The highly non-reactive nature of gold and its strong affinity to bind organic thiols makes it viable for bio-chemical applications [71]. The LSPR nano-ripple sensor can detect biomolecules and biomolecular interactions at the mono-layer scale [65, 77]. In this work, we detected an antibody-antigen interaction using adsorbate-induced LSPR-wavelength shift from the nano-ripple gold surface and its dependence on the antigen concentration. This sensor can also be employed to study

real time reaction dynamics of antibody-antigen, DNA hybridization, toxin-receptor, biotin-streptavidin, and other biological binding reactions.

Here, we demonstrate that the gold nano-ripple localized surface plasmon resonance (LSPR) based biosensor is a highly sensitive, low cost, and a label-free method for detecting the presence of an antigen. A uniform stable layer of an antibody was coated on the surface of a nano-ripple gold pattern on a biosensor chip followed by the addition of different concentrations of the antigen. A red shift was observed in the LSPR spectral peak caused by the change in the local refractive index in the vicinity of the nanostructure. The plasmon-resonance intensity of the scattered light was measured by a simple optical spectroscope. The gold nano ripple sensor shows monolayer scale sensitivity and high selectivity. The LSPR biosensor was used to detect antibody-antigen reaction of rabbit X-DENTT antibody and DENTT blocking peptide (antigen). The sensor can be further developed to obtain real-time analytical-reaction dynamics. Its capability to selectively manipulate bio-materials with high-sensitivity can lead to clinical and biomedical applications.

5.1 SEM Image of the Gold Nano-Ripple Substrate

The nano-ripple pattern fabricated by the fluence of $2x10^{16}\ clusters/cm^2$ impinged on the 100nm thin film of gold at an incident angle of 60 degree, had height of about 50 nm and wavelength 200 nm. There is about 20 nm of gold layer underneath connecting the nano ripples. The SEM image of the nano ripple pattern formed by a fluence of $2x10^{16}\ clusters/cm^2$ is shown in Figure 5.1.

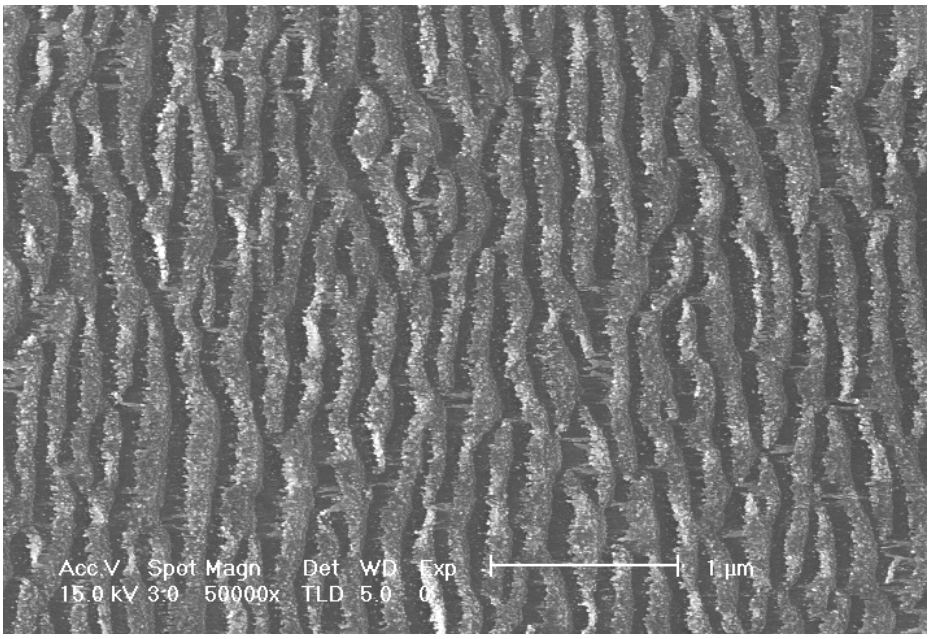

Figure 5.1: The SEM image of gold nano ripple structure induced by Ar gas clusters at a 60° angle of incidence with the fluence of $2x10^{16}\ clusters/cm^2$.

We cleaned the nano ripple gold surface by sonication in acetone followed by ethanol and distilled deionized water and dried by a stream of nitrogen gas. The first LSPR-scattering spectrum was measured at this point.

5.2 Protein A coating and LSPR measurements

The gold nano-ripple pattern formed by gas cluster ion beam irradiation showed plasmonic resonance phenomena [66]. To attach and immobilize antibodies to the nano ripple structures, we used the procedure by A.Hirlekar [71]. The cleaned nano-ripple gold was incubated in a solution of (0.002M) dithiobissuccinimide propionate (DSP) in dimethylsulfoxide (DMSO) at room temperature. DSP acted as a cross-linker that tightly binds protein A to the gold nano surface. It bound to gold through its thiol group and the other end attached to an amine group of protein

A. After 2 h, the surface was washed with DMSO to remove extra DSP and then rinsed with phosphate buffer saline (PBS), pH 7.4. The chip was then dried with nitrogen gas. LSPR reading was measured from the nano-ripple gold containing a monolayer of DSP cross-linker adsorbed on its surface. In order to functionalize the surface with protein A, we soaked the substrate in solution of protein A (1 mg/ml of PBS) at 4 ℃ for 24 h. We then dipped the substrate in ethanolamine hydrochloride (1 M) (used to block the remaining reacting DPS attachment sites) for 1 h. The surface was then washed with distilled water to remove extra ethanolamine hydrochloride and dried with nitrogen gas. The monolayer of protein A on the surface gave an LSPR spectral shift.

5.3 Immobilization of Antibody

The protein A-functionalized gold nanostructure was immersed in a solution of antibody (1 mg/ ml in PBS) overnight, washed with PBS, and dried with a stream of nitrogen gas. A stable and sterically accessible monolayer of antibody was achieved. The LSPR measurement was taken at this point. The uniform antibody coating immobilized on the surface gave a red shift to the plasmonic resonance wavelength. The antigen was then introduced at different concentrations and the shift with each antigen concentration was recorded.

5.4 LSPR Peak and Dependence on Antigen Concentration

The substrate was immersed in an antigen concentration of 1 μg/ml in PBS overnight, washed with PBS, dried, and the respective LSPR wavelength was measured. Similar procedure was conducted on other similar chip with antigen concentration of 2 μg/ml and 4 μg/ml. The plasmon peak increased in the 2 μg/ml sample but remained at the same resonance wavelength for the 4 μg/ml sample, no further red shift was observed.

5.5 Antibody-Antigen Interaction and the Detection Mechanism

In order to determine accurate and optimum LSPR spectral shift in response to a specific antibody-antigen interaction, it is important to achieve a stable and uniform layer of the antibody coating on the nanostructure where the antigen binding sites are sterically accessible. Figure 5.2a is a schematic diagram describing how the antibody coating was achieved on the substrate keeping antigen binding sites open. The red curve is the LSPR spectrum obtained from the antibody monolayer only. When the antigen was introduced in the system it caused an LSPR shift (green curve) representing the antibody-antigen reaction (Figure 5.2b). Hence, indicating the antigen present was specific for the antibody immobilized on the substrate.

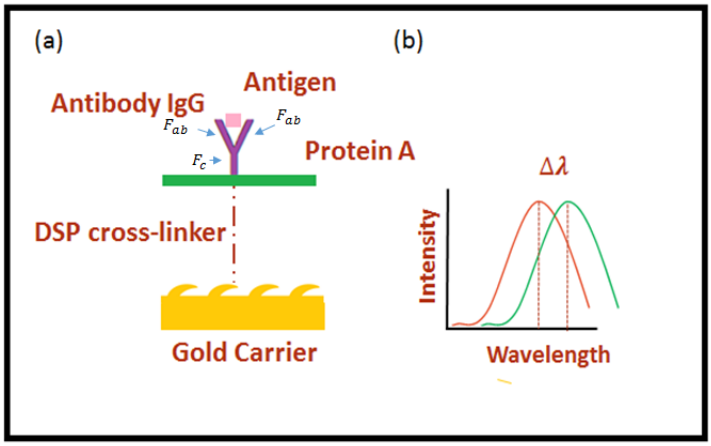

Figure 5.2: (a) A schematic diagram of protein A binds with the F_c unit of the antibody keeping it sterically accessible for the antigen to attach with its F_{ab} units. (b) The resonance curve with the antibody layer (in red) is used as a reference. The antigen attachment triggers the LSPR wavelength shift (in green) indicating antibody-antigen interaction.

The IgG antibody consists of three units. The antigen binds to the antibody site at two regions called the F_{ab} units. To optimize the antibody sites open for the antigen to bind, we avoided random alignment of the antibody immobilized on the surface [78, 79]. The substrate made a strong bond with the F_c unit of the antibody.

Since gold is not reactive to the antibody, protein A was used. IgG antibody bound to protein A with high affinity through the F_c region. In order to attain maximum density of protein A, DSP cross-linker was used to immobilize protein A on the gold nano substrate. The disulphide group in DSP cross-linker bound strongly to gold. DSP is amine reactive and reacted with the amine groups [80] in protein A allowing optimal availability of protein molecule sites bound to the F_c unit of the IgG antibody [81]. With the help of the DSP cross-linker, we were able to achieve a stable and more reliable layer of protein A over the surface. Table [1] describes

the LSPR spectral peaks obtained from DSP-modified gold nano-ripple surface and due to protein A immobilization. With every coating the local refractive index of the surrounding alters which causes a shift in the LSPR spectral peak. The induced-LSPR shift due to the adsorbed biomolecules on the plasmonic nanostructure was easily monitored using an optical spectroscope. The protein A layer produced a shift of 14 nm in the LSPR peak, Figure 5.3.

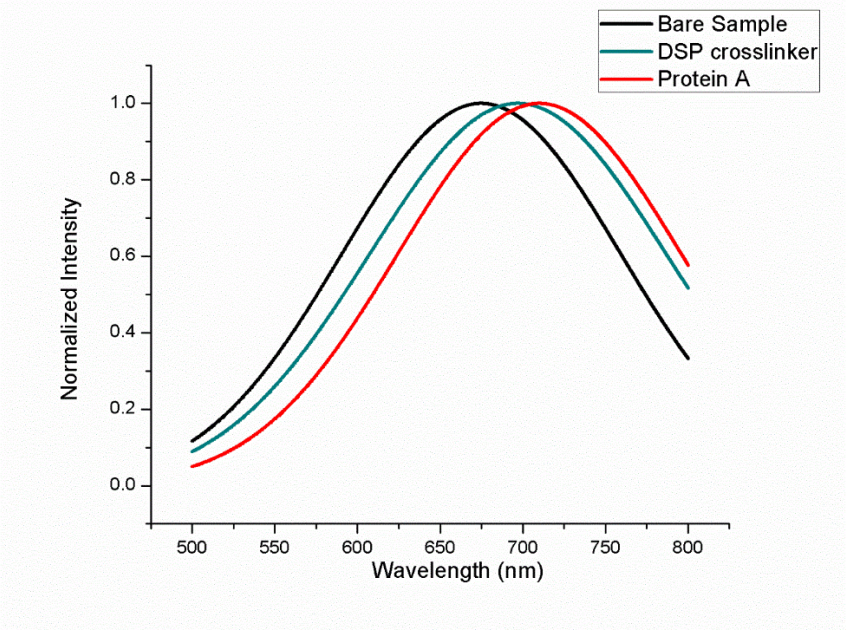

Figure 5.3: Indicates the resonance peak obtained by the nano gold sample with dose $2x10^{16}\ clusters/cm^2$occurs at 674 nm wavelength (curve in black). By functionalizing the surface with the monolayer of DSP cross-linker and protein A the LSPR shifts observed were 22 nm and 36 nm respectively.

Table 1: The LSPR wavelengths with DSP and protein A attachment on the surface

With	Bare Sample	DSP cross-linker	Protein A
LSPR peak	674 nm	696 nm	710 nm

Once the antibody coating was immobilized on the nano gold substrate, different concentrations of antigen solution made in PBS were allowed to bind to the chip and LSPR shifts were observed. We obtained the LSPR spectrum with the antigen concentration of 1 μg/ml, 2 μg/ml, and 4μg/ml in PBS as shown in Figure 5.4.

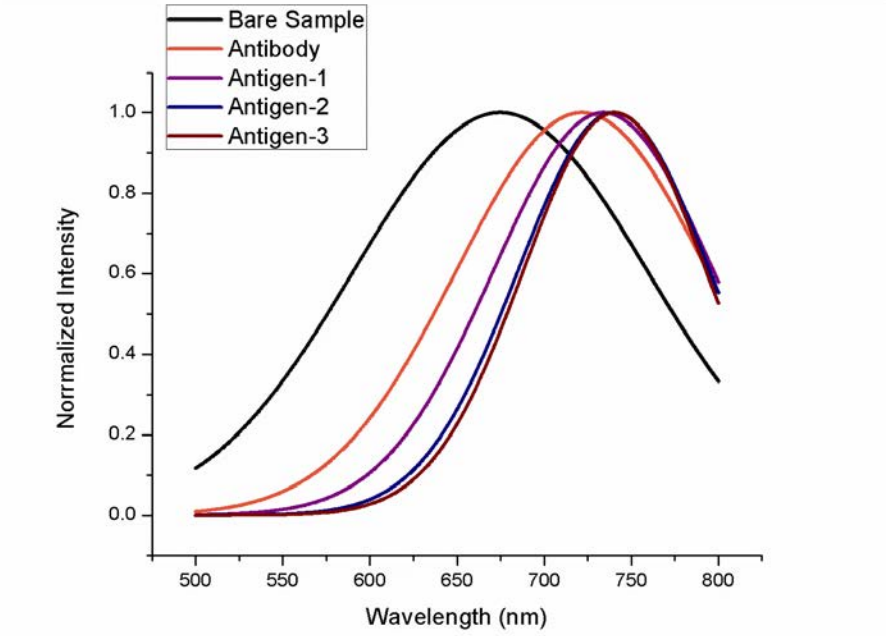

Figure 5.4: The resonance curves with antibody immobilization and three different concentrations of 1 μg/1ml, 2 μg/1ml and 4 μg/1ml (in PBS) of antigen is shown.

Table 2: The LSPR wavelength with the antibody coating is 721 nm and the three antigen concentrations shows that the surface saturates with antigen binding beyond the concentration of 2 μg/1ml with LSPR peak at 740 nm.

With	LSPR peak	Shift from Bare Sample
Antibody	721 nm	47 nm
Antigen-1	734 nm	60 nm
Antigen-2	740 nm	66 nm
Antigen-3	740 nm	66 nm

The resonance peaks occur at 734 nm and 740 nm for the concentration of 1 μg/ml in PBS and 2 μg/ml in PBS respectively. The sensor saturates with the concentration of 2 μg/ml PBS. For 4 μg/ml the LSPR peak remained at the same wavelength of 740 nm. Table [2] gives the resonance shifts with antibody and the three antigen concentrations with respect to the bare gold nano-ripple sample. It shows that as the number of antigen binding on the nano-ripple gold increases, the resonance shift increases. This shift is caused by the increase in the local refractive index change.

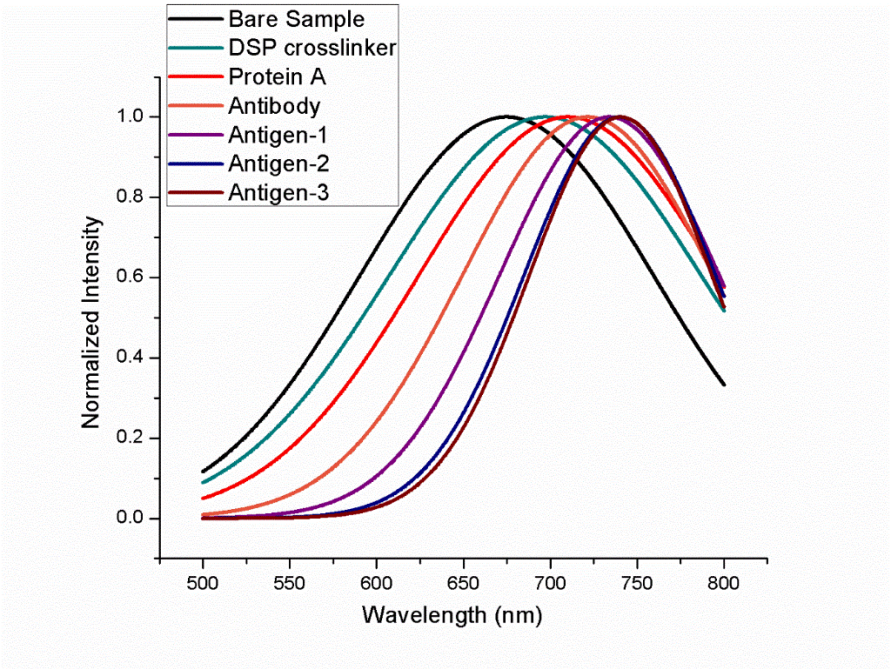

Figure 5.5: LSPR spectral peak with each monolayer attachment.

Figure 5.5 shows LSPR wavelength spectral peak shift with each coating. The AFM image of the bare nano ripple gold substrate and with the binding of antigen concentration of 2μg/ml in PBS is shown in figure 5.6.

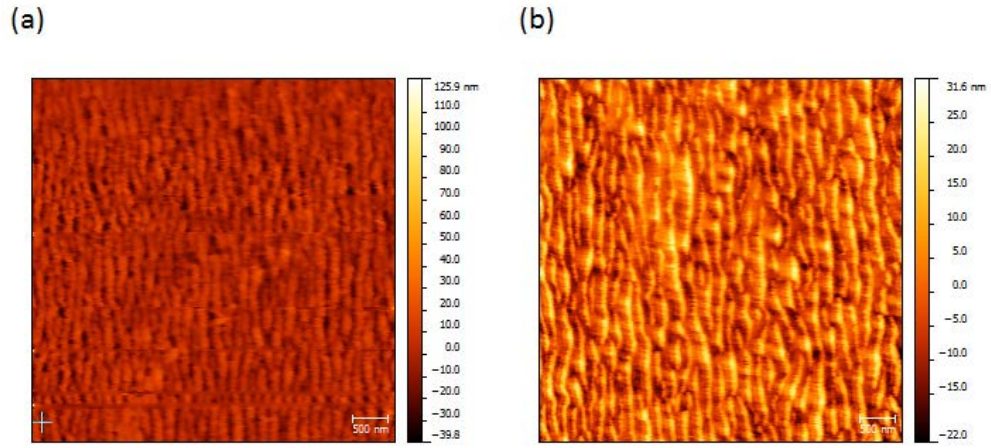

Figure 5.6: The AFM image of bare gold nano ripple structure (at the left) and that with antigen binding of the concentration of 2 μg/ml (at the right).

5.6 Conclusion

The LSPR based nano-ripple sensor fabricated by oblique gas cluster ion beam irradiation can be applied for the detection of antibody-antigen reaction. The induced local refractive index change due to the monolayer functionalization of protein A, the antibody and the antigen on the surface of the gold nano-ripple structure triggered a corresponding LSPR-resonance shift that was easily monitored by a scattering technique (spectroscope). The resonance shift depends upon the concentration of the biomolecules attached on the surface. We observe an increase in the LSPR-spectral shift with an increase in the concentration of the antigen bonded with the gold nano-ripple. The application of this sensor can be extended to other selective bio-molecular recognitions and real time reaction dynamics.

5.7 Future Directions of LSPR Sensing

LSPR sensors have made impressive progress in the past decade by developing into compact working devices and offering a variety of signal transduction platforms. LSPR spectral peak and refractive index RI sensitivity can be tuned by varying the material, geometry, and size of the nanostructure. The capability of LSPR biosensing of simple configuration, inexpensive instrumentation and real time tracking of particles, has made it a powerful medical diagnostic technology together with a platform for the most challenging problems in bio clinical research and medical science. The research interest in the field is so strong that every year there are tons of publications and research development made in the technology and better devices are coming forth. Some technological improvements such as robustness, high quality substrates, more compactness for portability and multichannel detection mechanism can make LSPR sensors a better tool for both biomedical research and consumer purposes.

Multiple sensing channels can have a lot of applications. Simultaneous detection of more than one analyte at a time can help in fast probing. Photonic sensor chips in collaboration with optical fiber can provide a fast, reliable and multi parameter sensing technique for reliable detection of biological species. LSPR sensors are advanced to the scale they can detect single molecular adsorption which opens exciting prospects for miniaturized biosensing devices. A robust, reproducible device with low detection limit, up to single molecules can be achieved with combining nano photonic sensor and whispering gallery mode (WGM) resonators.

In addition, by incorporating microfluidics into LSPR technology, simultaneous delivery of many samples, multiple biomarkers and using a variety of probes at the same time has become possible. It is a great advancement in the field of drug screening and diagnostics on-chip. The miniaturized size, ability to use more than one marker at once, small sample volume, easy-to-use, inexpensive and minimal equipment are some important benefits of these devices. By combining this science with surface enhanced Raman imaging, an interesting and useful application of multiplex biosensing is taking rise and would be a popular field of development in future.

For better medical and laboratory applications the LSPR sensor needs to be able to detect biological species in complex solutions such as blood and urine samples. By replacing white light spectrometers to LEDS and photodetectors for signal amplification and detection, the cost can be greatly reduced for commercial use. The LSPR sensing technology hold future challenges of developing into a further miniaturized device with multiple sensing parameters, high sensitivity, and selective bio recognition system, the ability to detect biomolecules in complex fluids, user-friendly interface for more accurate and precise measurements. With reusable, easily cleanable uniform substrates, it can be then incorporated in to better portable devices for point of care diagnostics and for other cost effective reliable commercial applications.

Section II

Chapter 6

Introduction

Electromagnetic field has a significant impact on ion transport across the cell walls of living organisms. Ion transport plays an important role in cell growth and function [82]. Increased exposure to electromagnetic radiation (EM) and its effect on health and safety is a possible concern. Radiation from all types of electronic devices such as cell phones, bluetooth, video games, laptops, television, and iPad may affect the humans. Experiments to understand the effect of electromagnetic radiation on living cells at the molecular level have been done [83]. Changes in the activity of enzymes, ion transportation through cell membranes, pH of the cells, transcription, protein transport, concentration of the hormones, and the formation of free radicals have been shown.

The use of magnetism in medicine is ancient. The Egyptian physician and philosopher, Avicenna, in the 10th century A.D recommended the use of magnetite powder to remove poisonous iron inside the body. Magnetite grains when taken with milk would attract the poisonous iron and speed the process of its excretion through the intestine. Magnetic force was used to remove iron particles from the eye in a similar fashion. Recently, magnetism is used in the fields of cardiology, oncology, radiology, dentistry, and neurosurgery.

Thousands of molecules take part in the process of cell development which utilize the transfer energy across cell membrane to maintain the electrochemical balance of the cells. Physical quantities such as pressure, temperature, and chemical potential inside the cell, balance the hemostasis of the cell. Recent studies on the affect EM fields on various biological systems have shown that low density exposure can modify gene and protein expressions in some cell types. At higher frequencies, an interaction of some DNA strands with EM signals can lead to strand breakage which causes mutations that can possibly cause cancer [84]. However, there is an inadequate understanding of weak electromagnetic effects on the function of the biological components of living organisms. Over the period of time, microorganisms have adapted to the earth's magnetic field which is about 0.65 G. Due to the increased role of magnetic field generators, both DC and AC magnetic fields in everyday life, there is an increased exposure to magnetic fields. Even extremely low magnetic fields generated by the environmental sources such as video-display terminals, high-voltage transmission lines, and other electrical appliances may cause an impact on the cell function.

At the cellular level, the effects of a static magnetic field are not well understood. Some studies showed little to no effect on the cells. However, recently, some changes in the orientation of the ions and charged particles due to their dipole moment has been detected when bacteria are grown in a nutrient broth under a magnetic field. This affects the flow of nutrients and ions across the membrane and in turn affects the cell growth and survival. One study indicated that certain

biomolecules absorb specific frequency ranges and some weak electromagnetic frequencies therefore can greatly affect behavior.

Magnetic field application in the field of medical and physiological science is growing significantly. There is no standard measure of a safe magnetic field exposure, thus, it is important to research the results of magnetic field exposure on living organisms. There are three types of categories of cellular life, Archaea, Bacteria, and Eukaryote. Prokaryotic organisms are unicellular simpler structure with sturdy cell walls and do not contain organelles or nuclei. They are believed to be the first form of life to exist on earth. Bacteria and Archaea are classified as prokaryotic organisms. Eukaryotic organisms are complex multicellular structures consisting of various organelles and a nuclei. Bacteria are persuasive and abundant. Because of its pervasive behavior, it is very important to understand the nature of the simplest organism in order to understand the activities and functions of more complex like eukaryotic organisms. Bacteria acts as a suitable and simpler model of cellular life and can be utilized to develop valuable insight into the physical processes taking place inside the cells and further investigation can help in the understanding of more complex cells such as the eukaryotic cells.

Bacteria grows exponentially and its growth rate depends on physical conditions such as temperature, nutrient density, oxygen, chemical potential across membranes, pressure, and the density of the cell membrane. It is important to understand the intensity of the electromagnetic fields that bacteria can withstand and bacterial behavior under the influence of the radiation. Chapter 7 provides a

brief overview to the cellular structure of a bacteria, ion transportation across the membrane, bacterial growth, and thermodynamics.

In Chapter 8, we compare the growth of two different types of bacteria on the nano-ripple glass pattern and plain glass slide with and without the effect of a weak magnetic field. Some nanostructure materials have very interesting properties and features regarding facilitating or impeding cell growth. An understanding of which can help us utilize those structure to our benefit in healthcare sciences, research, and other industrial purposes. Scientists have developed and designed biocompatible and environmentally safe polymer and metal nanostructures with several medical and clinical advantages. These can be applied to the fields of agriculture, food manufacturing, and industrial applications. There have been research were metal nanoparticles have evidently damaged bacterial cell walls by influencing the proton and ion transport across the cell membrane of the bacteria. In other cases, bacteria form colonies following certain patterns on the nanomaterial that can have different functions such as guiding specific metabolic reactions or controlling bacterial growth [85].

Here, we use a self-assembled nano-ripple structure on glass for bacterial growth studies. Bacterial orientation and community development on a cellular level was demonstrated. The growth pattern of the bacteria follow different patterns under different conditions of magnetic field at fixed temperature. We performed this experiment with two strains of bacteria. We examined the growth of *Escherichia coli* and *Pseudomonas aeruginosa* on nano-ripple glass structure under weak

uniform, non-uniform, as well as control condition of a magnetic field at room temperature.

In Chapter 9, we investigate the effect of different types of magnetic fields (~5G) on the growth rate of bacterial strains on a plain glass slide. It is not well known if the magnetic field effects the DNA, cell walls, or other enzymatic activities of the bacteria. Standard cultures of *Escherichia Coli*, *Staphylococcus Epidermidis*, *Staphylococcus Aureus*, and *Pseudomonas Aeruginosa* were grown in a series of weak alternating, homogeneous, and controlled electromagnetic fields at room temperature on a plain glass slide. We obtain the growth curve using our collected data and analyze the behavior of the different strains of the bacteria. Further study in this direction can be an interesting extension of this work.

Chapter 7

Bacteria Cellular Structure and Electrodynamics

Electromagnetic fields are hypothesized to be one of the causes of cancer and other life threatening mutations and gene alterations in the living organisms [82-84]. There has not been conducted enough theoretical research in the understanding of how magnetic fields affect cell function and growth. There are also useful magnetic field applications in medical science, such as the magnetic therapy, nuclear magnetic resonance (NMR), and magnetic resonance imaging (MRI). Infection and diseases caused by bacterial incubation in the human body makes it even more significant to understand whether bacterial growth is affected by magnetic field exposure. How can this information be used in medical science to help the recovery process. This information can be helpful in food packaging and storage and other agricultural and industrial purposes. Other results in bacteria treated with magnetic field comprises cell motility and morbidity, the growth rate, and change in antibiotic susceptibility.

7.1 Eukaryotic and Prokaryotic Cells

Living organisms are composed of cells that have evolved over the period of time and inherited common features that make them capable of utilizing chemical

interactions between the organic molecules to produce energy to perform biological functions and maintain survival. There are two kinds of living cells, prokaryotic and eukaryotic (Figure 7.1). Prokaryotic cell does not have a nucleus and organelles. They are also structurally smaller and simpler cells. They exist in the shape of sphere, rod, or other simple shapes with a size of about 0.1-2μm. Whereas eukaryotic cells are larger much complex structures ranging from 10-100 μm in diameter.

Eukaryotic and Prokaryotic cells have several features in common, they both are made up of DNA coiled many times around certain proteins called histones. Their differences are in the DNA structure. Eukaryotic cells have linear DNA and most prokaryotic cells have a single large circular DNA strand, located in an area of the cell called the cytoplasm. Also cells have ribosomes interpret the RNA sequence to produce proteins. Ribosomes for prokaryotic cells are much smaller in comparison with the eukaryotic cells and so many antibiotics can affect prokaryotic ribosomes, but not eukaryotic ribosomes. This is why antibiotics can kill the bacteria without harming human cells. The interior portion of the cell enclosed inside the plasma membrane is called the cytoplasm. It contains of all the membrane bound organelles of the eukaryotic cell that have specific functions. Prokaryotic cells do not contain membrane-bound organelles, such as the nucleus or a mitochondria. The cytoplasm of prokaryotic cells consists of all of its content including the cytosol, ribosomes, cytoskeleton and the nucleoid. Nucleoid contains most of the genetic material of the cell. And most chemical reactions of the prokaryotic cells take place in the

cytosol. Cytosol constitutes most of the soluble proteins of the cell. It contains water, carbohydrates, ions, proteins, lipids, and metabolites. The nucleus of the eukaryotic cell exists in the cytosol and it contains all of the DNA. The examples of eukaryotic cells are plants, animals, algae, and fungi. Prokaryotic cells on the other hand are divided into two categories, bacteria and archaea. Bacteria are small microorganisms that grow by the process of binary fission. They are most abundant in nature and possess the ability to survive in different physical conditions because of its accommodative behavior.

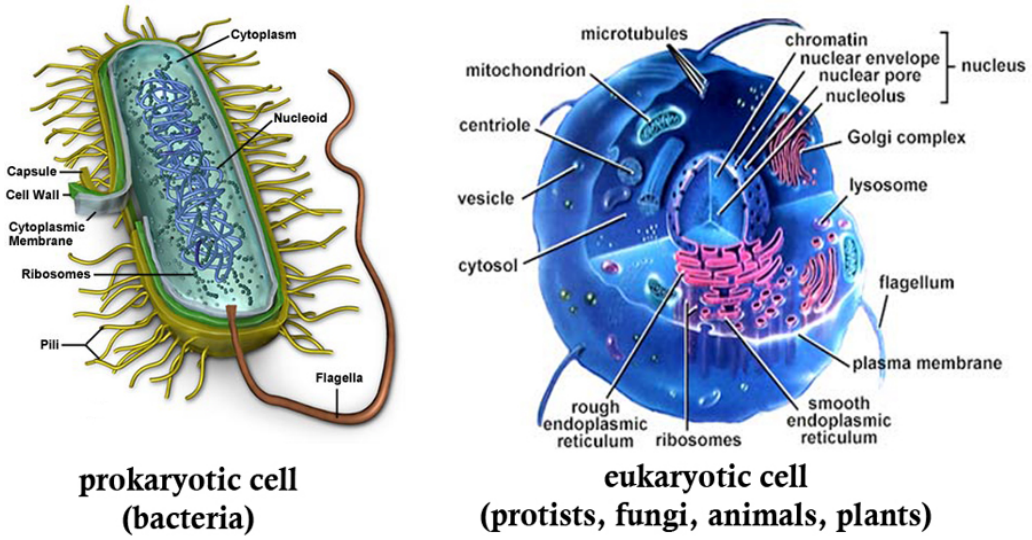

Figure 7.1: Prokaryotic cell and Eukaryotic cell (https://www.thinglink.com/scene/565728773106827265).

7.2 Cellular Membrane and Ion Channels

All cells are contained in a cell membrane that protects the cell and regulates the movement of ions between the extracellular and intracellular spaces. Cell membrane consists of phospholipid bilayer, and embedded proteins, and small

portions of carbohydrates. It has a thickness of about 7.5 nm-10 nm. Phospholipids have both hydrophobic and hydrophilic components and are relatively small molecules. The hydrophilic side of the phospholipid bilayer face the outermost and innermost sides of the membrane while the hydrophobic side forms the center of the layer. Cellular membrane displays selective permeability. Specific ions, nutrients, and proteins needed to retain and synthesize molecules to maintain, cell function, permeates across the cell membrane through special ion channels and porins. While the metabolic waste leaves the cell.

Ionic composition in the extracellular space is different from the cytoplasm which produces an ion gradient across the membrane called the electrochemical gradient. Charge distribution across the inner membrane is altered due to the selective transport of ions by the ion channels. The direction of flow of the ions depends on the ion type, ion concentration, and charge difference across the cell wall. The ion flow gives rise to electrical and chemical signals. These signals are important for the cell to perform certain functions and for the sensory response of the body.

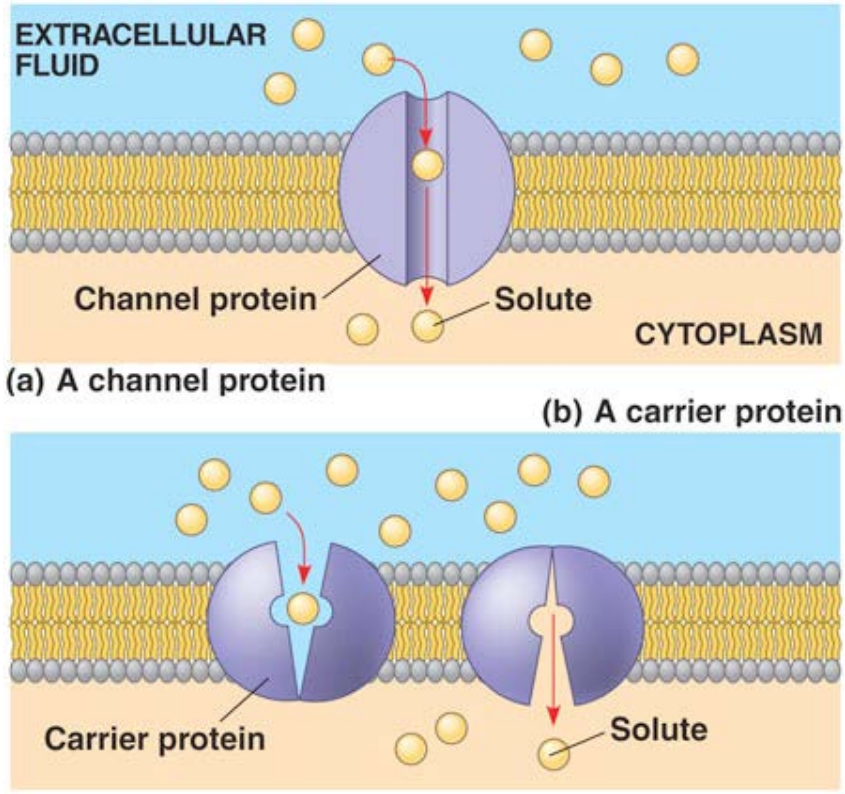

Figure 7.2: Ion Channels (a) channel protein (b) carrier protein (https://physiologue.wordpress.com/).

The cell drives out carbon dioxide by taking in oxygen for cellular respiration. Oxygen, carbon dioxide, and hydrocarbon are non-polar and hydrophobic molecules that can easily cross a lipid bilayer. Sugars and water are small polar molecules that can pass through the lipid bilayer but they do not cross the cell membrane quickly. There exists an electrochemical gradient of ions across the cell membrane, that consists of two parts, the chemical gradient, is due to the difference in solute concentration across the membrane, and the electrical gradient, is because of the difference in charge across a membrane. Two most common types of

membrane transport proteins are channel proteins and carrier proteins (Figure 7.2). Carrier proteins grasp nutrients and substances and undergo conformal changes to transport their passengers to the other side of the cell membrane. Carrier proteins can mediate both passive and active transport. In passive transport no energy is consumed while molecules diffuse down the concentration gradient. In active transport, energy is needed for the movement of solute particles against the concentration gradient. Channel proteins usually have a pore and are ion selective. They have a hydrophilic channel that ions or polar molecules tunnel through across the hydrophobic lipid bilayer.

7.3 Bacteria Cell Wall

Bacteria are a single-celled microorganisms that have well-defined cell wall. The cell wall helps protect and preserve the content in the cytoplasm from any damage from the surrounding environment. There are two types of bacteria (gram-positive and gram-negative) depending on their cell wall structure as shown in Figure 7.3. Peptidoglycan is a complex polysaccharide which gives the outer membrane its structure and surrounds the inner membrane. It consists of two sugars, N-acetylglucosamine (NAG) and N-acetylmuramic acid (NAM) which have alternating glycolytic bonds. The cell wall of Gram-positive bacteria is composed predominantly of the peptidoglycan. Embedded in peptidoglycan layers is a class of molecules called teichoic acid that gives the membrane an overall negative charge. Gram-negative bacteria have a complex cell membrane structure. It has an outer membrane which consists of lipopolysaccharides, carbohydrates that are

bonded to lipids, in addition to an outer membrane and a thin peptidoglycan. Gram negative bacteria have porins that gram-positive bacteria does not have. The outer membrane of Gram-negative bacteria invariably contain endotoxins, such as lipopolysaccharide (LPS). Not all bacteria have a cell wall. However, they have other characteristics of prokaryotic cells and have a prokaryotic ribosome. The cell is enclosed by an adhesive layer of polysaccharide or protein called capsule. The capsules stick together and make colonies.

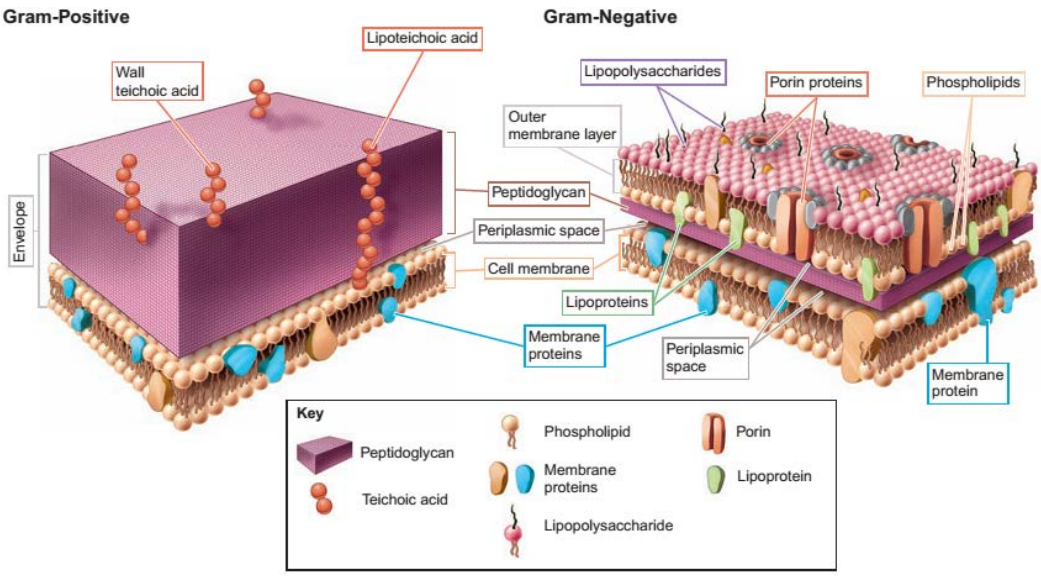

Figure 7.3: Gram-positive and Gram-negative bacteria (http://www.microbiologyinfo.com/differences-between-gram-positive-and-gram-negative-bacteria/).

7.4 Bacterial Growth and Division

Bacterial cell division is the process by which a bacterial cell divides into two daughter cells, each with a copy of the chromosome. Bacteria lack a nucleus. Most

bacteria have a single circular chromosome found in the region of the cell called the nucleoid. Bacteria grows asexually through binary fission. Cell cytoplasm increases during microbial growth and it continues to grow until it reaches a point where DNA replication starts. DNA replication occurs in three steps: initiation, elongation, and termination. There is the lag phase, where bacteria is adapting the new environment and increases in size and mass but has not started cell division. The surface area of the cell grows as the cell mass increases during the lag phase and separates identical components into two daughter cells. This is the log phase of growth where the cells exponentially increase. When the cells reach a maximum concentration, cell replication decreases and enters the stationary phase. In the stationary phase, the growth and death rate of bacterial cells is in equilibrium. In the death phase, individual bacteria die at a uniform rate. Eventually number of dead cells outnumber live cells. Bacteria growth rate depends on the physical conditions and chemical composition of its environment.

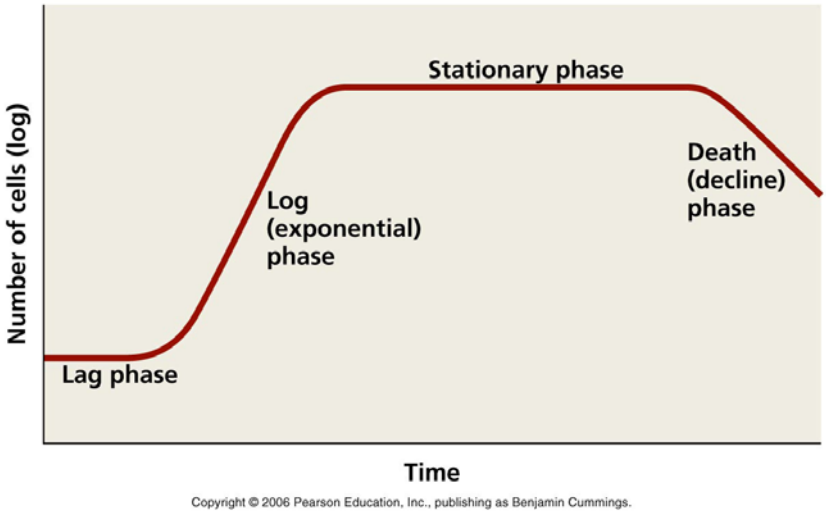

Figure 7.4: Bacteria growth curve (http://academic.pgcc.edu/~kroberts/Lecture/Chapter%206/growth.html).

The generation time of bacteria can be calculated by its growth curve which is experimentally determined (Figure 7.4). By measuring the optical density of bacteria with change in time, we can plot a standard growth curve of the bacteria. The growth curve indicates the increasing cell number and mass during growth. Bacteria require certain physical and nutritional factors to support cellular growth such as temperature, osmotic pressure, pH, hydrostatic pressure, moisture, and amount of carbon, nitrogen, phosphate and other essential elements in the broth. Bacteria divides through binary fission and multiply as 2^0,2^1,2^2,2^3,…2^n where n is the number of generations. If N_o is the initial number of cells and n is the number of division events of the generating daughter cells, then after reproduction the total number would be,

$$N = N_o 2^n \tag{7.1}$$

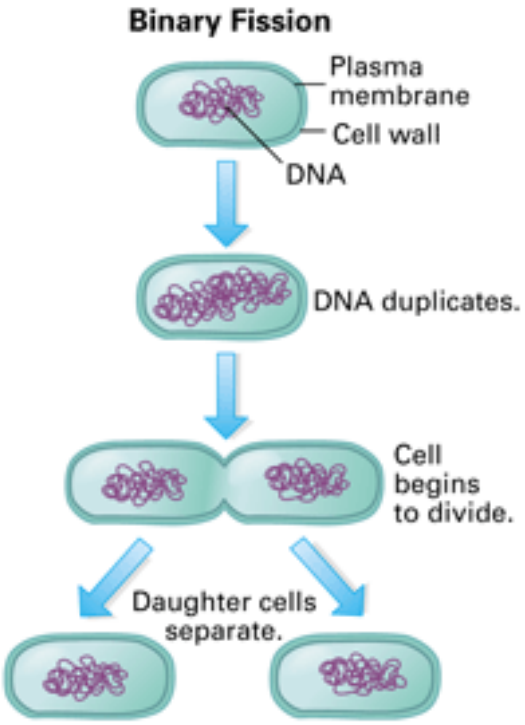

Figure 7.5: Bacterial binary fission division (http://byjus.com/biology/binary-fission/).

Generation time is the time in which bacteria grow double in number. It's different for different bacteria. After an interval of time, Δt, we can calculate the number of generations and the generation time:

$$Generation\ Time = \frac{\Delta t}{n} \text{ where, } n = \frac{\log N - \log N_o}{\log 2} \quad (7.2)$$

However, Equation (7.1) is a simple approach for measuring bacterial growth and does not include the time variable to describe the growth curve of the bacteria. The number of dividing cells must be expressed as a function of time. Friedrich Widdel,

[86] described how the doubling time (t_d) is inversely related to the number of generations $n = \frac{t}{t_d}$. Growth rate can then be represented as:

$$N = N_o 2^{t/t_d} \tag{7.3}$$

Expressing the doubling time reciprical $1/t_d$ by some constant υ, or the number of generations per unit time:

$$\frac{1}{t_d} = \upsilon \tag{7.4}$$

Since $$2 = e^{ln2} \tag{7.5}$$

Equation (7.3) can be written as

$$N = N_o(e^{\ln 2})^{t/t_d} = e^{\left(ln2/t_d\right)t} \tag{7.6}$$

The doubling time of a particular species is a fixed value μ:

$$\frac{ln2}{t_d} = \mu \tag{7.7}$$

Now we can write

$$N = N_o e^{\mu t} \tag{7.8}$$

It is incumbent to know the cell density in order to count the number of cells in a culture volume V.

$$\text{Bacterial Cell Density} = N/V \tag{7.9}$$

Equation (7.8) can be written as:

$$\frac{N}{V} = \frac{N_o e^{\mu t}}{V} \tag{7.10}$$

An optical spectrophotometer is used for measuring cell density. Light gets scattered after passing through the culture by the bacterial cells. Using the optical spectrophotometer we can determine the optical density (OD), proportional to the light absorption by the cells, $\frac{N}{V} = OD$.

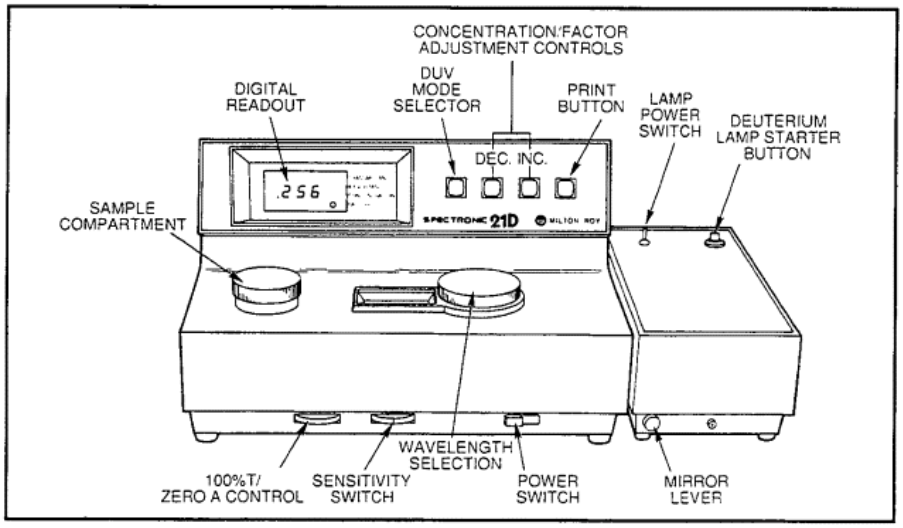

Figure 7.5: Spectronic 20 used in measuring optical density of bacteria.

7.5 Thermodynamic State and Laws

When a system has no net energy flow it is at thermodynamic equilibrium. Living cells have a slight charge on the cell membrane. Any forms of energy such as thermal energy or chemical energy is transferrable across the membrane. A single biological cell might contain 10^{14} molecules. Thermodynamic quantities such as

temperature, density, energy, entropy and pressure describe the cell structure, function and its health. Thermodynamic laws are important in order to understand the ability of biological cells to utilize and transform energy in various ways.

7.5.1 Electrochemical Potential

The electric force on an ion depends on the ion potential difference across the membrane. The equilibrium potential of an ion can be calculated by a simple formula known as the Nernst equation. It relates the equilibrium ratio of the concentration of ions on both sides of the membrane to the potential difference across the membrane. The membrane potential varies according to the functional status of the cell. For example, a nerve cell that has a membrane potential of -70 mV at rest, but when it reaches an excited state the membrane potential increases to about +30 mV, where it starts sending signals.

If c_1 is the concentration of the ions outside the cell membrane and c_2 is the concentration of the ions inside the cell membrane. The Nernst equation is,

$$U_2-U_1=RT/ZF \ln (c_1/c_2) \quad (7.11)$$

Where U_2-U_1 is the potential difference across the cell membrane, $R=Nak_B=R=8.31441$ J/mol-k is the gas constant, Z is the ion valency, T is the absolute temperature in Kelvin and faraday constant $F=Na\mathit{e}=96484.56$ C/mol.

7.5.2 The Equation of Continuity

The equation of continuity can relate the transport of ions from one region to another in a cellular system. As mentioned earlier, there is a slight potential across cell membrane that causes the ion/nutrient transport across the membrane which is essential for cell function and growth, this potential needs to be maintained constantly. If C is the concentration of ions in a length Δx,

$$\partial C/\partial t=-\partial j_x/\partial x \tag{7.12}$$

This is the continuity equation in one dimension where j_x is particles per unit length per unit time, the current density and t is the time of flow.

In three dimensions, it is written as:

$$\partial \rho/\partial t=-\partial j_x/\partial x-\partial j_y/\partial y-\partial j_z/\partial z=-\nabla.j \tag{7.13}$$

Where ρ is the charge volume density.

7.6 Magnetic Field Effects on Ion Transportation

When there is a potential difference, ion charges begin to flow in the opposite direction. Drift velocity is defined as the velocity of an ion experiencing force due to an electric field. In a medium, the nutrients velocity is directly proportional to their charge, mobility μ, and the strength of the electric field which is expressed as:

$$v_D = \mu \boldsymbol{F} = \mu q \boldsymbol{E} \tag{7.14}$$

Considering an electric charge, q, traveling across the membrane in a uniform electric field, E, and magnetic field, B. The force acting on the particle is given by the Lorentz law [87]:

$$\boldsymbol{F} = q(\boldsymbol{E} + \boldsymbol{v} \times \boldsymbol{B}) \tag{7.15}$$

where $\boldsymbol{v}$ is the ion's instantaneous velocity and $E \cdot B = 0$. Equation (7.14) then yields a correlation between the drift of the ionic molecule and its electromagnetic environment.

$$\boldsymbol{v}_D = \mu[q(\boldsymbol{E} + \boldsymbol{v} \times \boldsymbol{B})] \tag{7.16}$$

When we use the transverse field $\boldsymbol{v}x\boldsymbol{B}=v\boldsymbol{B}$ always. So E could simply be replaced by $E+v\boldsymbol{B}$, wherever it appears. Thus in the presence of magnetic field the movement of ions and nutrients across and within the cell membrane is affected which will influence the growth of bacteria. By comparing the initial and final concentrations of the bacteria in the broth we can observe and evaluate the rate of change in growth of bacteria with and without B-field.

Chapter 8

Growth of Bacteria on Nano-Ripple Glass Substrate under the Effect of Weak Magnetic Fields

Nano-ripple pattern on glass was fabricated by gas cluster ion beam irradiation. Comparison of the growth of two bacterial species (*Escherichia coli* and *Pseudomonas aeruginosa*) on nano-ripple glass pattern and plain glass slide showed more growth on the nanostructure. We also studied the effect of (uniform and non-uniform) weak magnetic field on the growth of both *Escherichia coli* and *Pseudomonas* bacteria on the nano-ripple pattern. We observe different behavior in the bacterial growth on the glass nano-ripple surface inside and outside the magnetic field. Bacterial growth seems to slow down on structures in the presence of the magnetic field. Bacteria growing on a nano-ripple pattern over the magnet tends to make smaller colonies as compared to the ones grown outside the magnetic field. Uniform magnetic field effect shows uniformly distributed and much smaller bacterial colonies on the substrate. It was also seen that bacteria grew more significantly around the plain glass and nano ripple glass structure than on the surface.

8.1 Motivation

Because bacteria are abundant in nature and may often incubate inside the human body, it is important to understand their behavior in different environmental conditions, as well as the factors that influence the physiology of bacteria. One of the major causes of illness and death is bacterial infection and contagion. Microbial contamination is a severe issue in healthcare, the food industry, biomedical and clinical equipment, and water purification.

Bacteria play its role in a variety of fields. It can be very harmful at times, and medical devices undergo bacterial colonization all the time. Because of this, scientists are trying to design antibacterial nanostructure materials. Many nanostructures are excellent impeders of bacterial growth and biofilms [88-92]. Nanotechnology has many potential applications in treatment and diagnosis of diseases and maintaining medical equipment. Some engineered nanostructure polymer materials have proven to inhibit the growth of bacteria, and thus act as an antibacterial agent or coating [93]. One study showed that nanostructured microspheres of silver zinc oxide resists the growth of bacteria and biofilms [94]. The arrangement of bacterial colonies and formation of biofilms on nano patterns facilitates metabolic reactions [95]. Thus, it is essential to understand the chemical and physical interactions between bacteria and nano surfaces.

On the other hand, the nature of bacteria is very adaptive and to understand how they survive under different conditions of density, temperature, pressure, and magnetic field is important in medical and clinical science. Microorganisms have

adapted to fluctuations in the earth magnetic field over a period of time. However, the response of bacteria to other external magnetic fields is still a vast topic of study [96, 97]. In space, humans encounter different radiations and electromagnetic forces. One of the interests is to study the magnetic field influence on the human body in outer space, i.e, when they leave the earth's magnetic field. Electromagnetism has significant importance in understanding living organisms. Magnetic signals are received from the brain, heart, isolated nerves and also emitted during the process of muscle building. Bacteria grows through binary fission process and the microbial growth strongly depends on the ion transportation through the cell walls of the microorganisms, their cellular structure, atomic, and molecular interactions, enzymatic activities, other protein functions, and neural network in the living organisms. All these processes are affected by electromagnetic fields. In some animals, some bacteria are magnetotactic, which contain magnetic particles, mainly connected to the neural tissues, which steer the direction of their movement. The rapid increase in the use of magnetic field devices for medical use such as in radiology, cardiology, dentistry, oncology and neurosurgery [98], has made it important for us to understand the effect of magnetic field on living organisms to further use it for biomedical applications.

Strong magnetic fields can have strong effects [99, 100], such as the breaking and forming of chemical bonds which play a big role in the synthesis of DNA and thus cellular growth. However, weak magnetic field effects are not negligible. Although such experiments may be hard to conduct, they are of significant importance as interaction with magnetic devices cannot be avoided and continuous perturbation

may result in permanent biological changes. Hence, the study of biological effects of magnetic fields is crucial to understand microbial growth. The perturbative effects caused by the weak magnetic field may have an impact on some organisms [101, 102]. Since bacteria are single-celled organisms, it is easy to study the effect of magnetic field on their growth and impact on the cell structure in order to control and treat microbial diseases. It is a study that can be extended later to study other cellular structures.

The aim of this chapter is to study the weak magnetic field influence on the growth of *Escherichia coli* and *Pseudomonas aeruginosa* on a nano-ripple glass substrate in comparison with a plain glass cover slip. Some studies show that the low frequency alternating magnetic fields tend to slow down the growth rate of *Escherichia coli* [103-108]. It is interesting to consider the adhesion property of *Escherichia coli* and its growth on a nano-structured glass. The idea was influenced by the regeneration of the tissues and functional recovery following pathways set by nanostructures such as the spinal nerve cell growth guided by nano tubes or other biomaterial designs [109-111]. In our experiment, the bacterial adhesion to the nanostructured glass is enhanced because of the structure resists the motion of the microorganisms in the nano groves thus limiting their movement. The bacterial colonies grow bigger on the nano-ripple glass. However under weak magnetic fields, the size of the colonies was reduced. We studied the effect of both the homogeneous (uniform electromagnetic field) and nonhomogeneous (non-uniform bar magnetic field) magnetic fields on the formation of bacterial colonies on the

nano-ripple and plain glass cover slips in comparison with no magnetic field influence.

8.2 Glass Nano Ripple Pattern

We engineer nano-ripple pattern on a glass cover slip by means of oblique angle gas cluster ion beam (GCIB) irradiation [21, 27, 56] (see Figure 8.1) using an Epion cluster ion implanter. Clusters of argon gas (each with about 3000 atoms of argon) of energy 30 Kev bombard the glass surface at an incident angle of 60°. The off-normal cluster ions and the surface atoms undergo synergistic interactions which cause the forward sputtering of atoms. As a result of forward sputtering and surface diffusion of the glass molecules, a nano-ripple pattern is obtained [51, 52, 66]. The geometry of the nano-ripple structures is tunable by changing the GCIB irradiation fluence [77]. For the cases discussed, we irradiate the glass cover slip with GCIB fluence of 5×10^{16} clusters/cm^2. The cluster ion beam flux is kept constant at approximately 3.9 $\times10^{12}$ clusters/cm^2/sec. Cluster formation is a complicated process and the theoretical descriptions of this process are limited. The phenomena of nucleation and growth takes place through the birth of small molecular clusters that form and grow by molecular collisions. Cluster-cluster aggregation becomes more evident when the number of the clusters are large. The detailed mechanism of GCIB induced ripple formation is explained in detail by Tilakaratne et al. in reference [33]. Figure 8.2 shows an atomic force microscope (AFM) image of the nano-ripple arrays fabricated under selected conditions of 5×10^{16} clusters/cm^2 GCIB fluence, and 60 degrees GCIB incident angle.

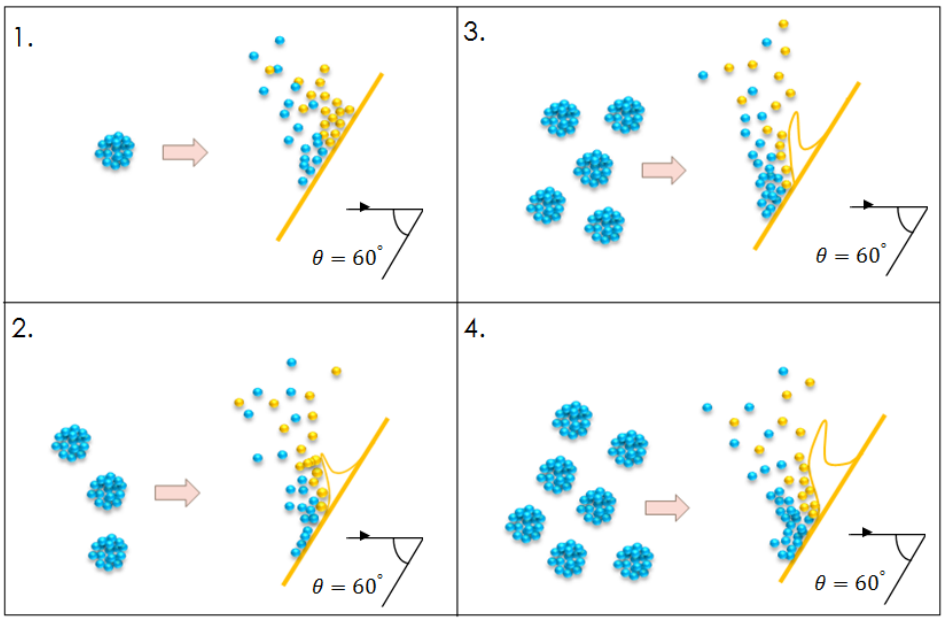

Figure 8.1: Schematic diagram of the oblique angle gas cluster ion beam (GCIB) irradiation used in the fabrication of nano-ripple glass array structures.

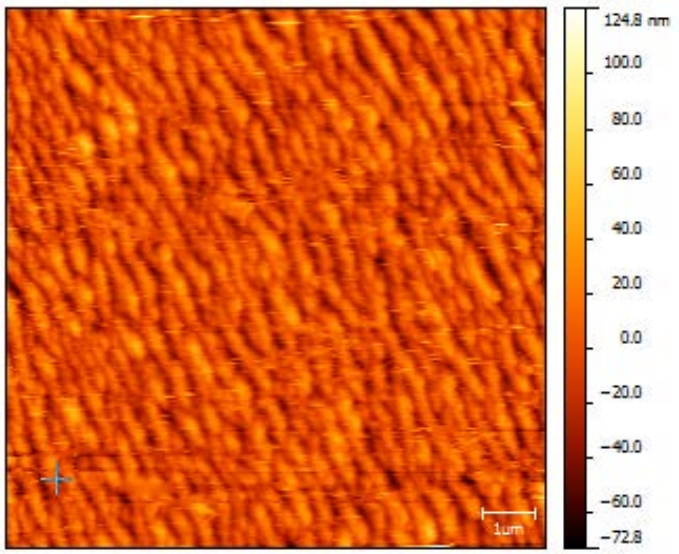

Figure 8.2: AFM image of the nano-ripple array on the glass surface obtained by GCIB irradiation fluence of 5×10^{16} clusters/cm^2, for an incident angle of 60 degrees.

8.3 Weak Magnetic Field Conditions

The glass substrates and the plates were first cleaned in an autoclave system in order to remove all impurities. *Escherichia coli* and *Pseudomonas aeruginosa* were then grown on multiple glass nano-ripple structure for three days at room temperature. We had three plates of each bacteria growing on a plain glass cover slip for comparison. After sufficient growth, we then washed the substrates with phosphate-buffered saline (PBS) to remove the unattached bacteria from the surface. The bacteria were stained using a Gram crystal violet solution. The glass substrates were washed once again with the buffer solution to remove excess stain and dried. We then covered them with the microscopic coverslip. The images of the bacteria on the plain and nano-ripple structured glass substrates were taken under a microscope of 100x magnification.

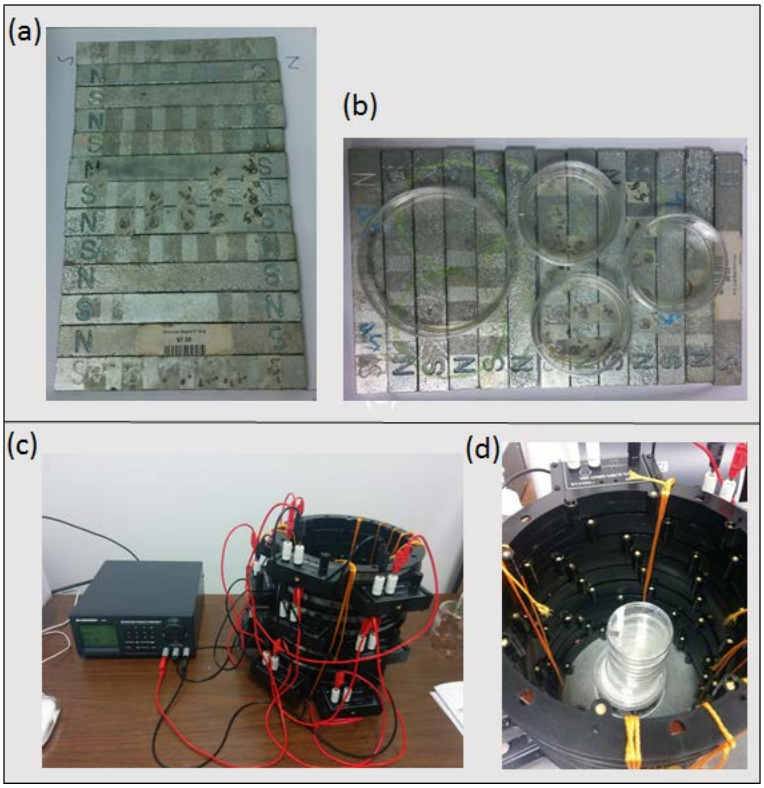

Figure 8.3: Experimental arrangement used for generating desired magnetic field environments. (a) and (b) show the bar magnetic field setup. (c) and (d) show the uniform magnetic field setup. The uniform magnetic field was generated by applying current in the turning coils using a power supply kept at constant voltage.

We studied the growth under weak magnetic field influence as well. One set of *Escherichia coli* plates was placed in the electromagnetic field of ~5 G and one set was placed on the bar magnets with range -5 G to 5 G. The configuration of the electromagnets and the bar magnets is shown in Figure 8.3. All the plates were kept at room temperature. For *Pseudomonas aeruginosa*, a set of plain and nanostructured glass substrates were placed on the bar magnets.

8.4 Bacterial Growth under Weak Magnetic Field Influence

Escherichia coli grew more on a glass nano-ripple surface than on a plain glass slide in the absence of the magnetic field. The nano-ripple pattern seemed to trap the microorganism in the gratings. And since more bacteria stuck on the nano pattern, we observe more bacterial colonies that are also larger in size as compared to ones on a plain glass slide. Figure 8.4 shows microscopic images of *Escherichia coli* colonies on a glass nano-ripple structure and Figure 8.5 shows similar images for the plain glass slide. The growth on the plain glass is less and few any colonies grew on the plain glass slide.

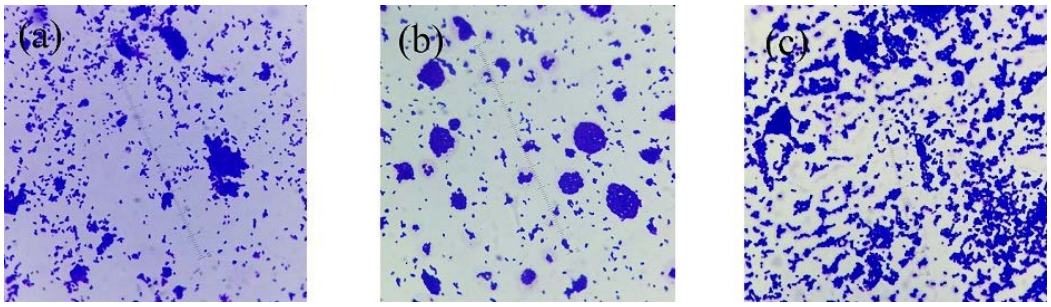

Figure 8.4: (a), (b), and (c) show the growth of *Escherichia coli* on three nano-ripple glass patterns in the absence of the magnetic field.

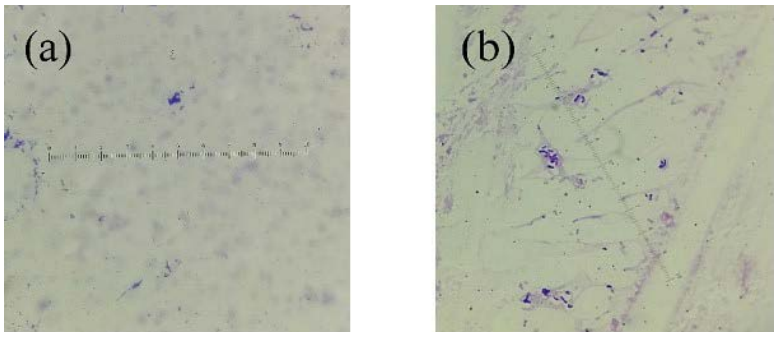

Figure 8.5: (a) and (b) show the growth of *Escherichia coli* on two plain glass surfaces in the absence of the magnetic field.

Bacteria was simultaneously grown on nano-ripple pattern inside uniform and non-uniform weak magnetic fields. Weak magnetic fields do not kill the bacteria, but instead affect their growth. Magnetic fields slow down the growth rate as seen by the reduced size of bacterial colonies. Figure 8.6 and Figure 8.7 compare the bacterial growth on the bar magnets (non-uniform field) and in the uniform magnetic field and shows how growing under the two different magnetic fields affects the size of the colonies as well. The results are very interesting since the magnetic field has a very prominent effect on the growth of the bacteria.

Under the uniform field, the bacteria spreads on the surface in a uniform fashion and colonies are very small. In non-uniform field, the colonies are relatively larger but still much smaller in comparison to the growth outside the magnetic field. The bacteria are also not uniformly distributed over the surface.

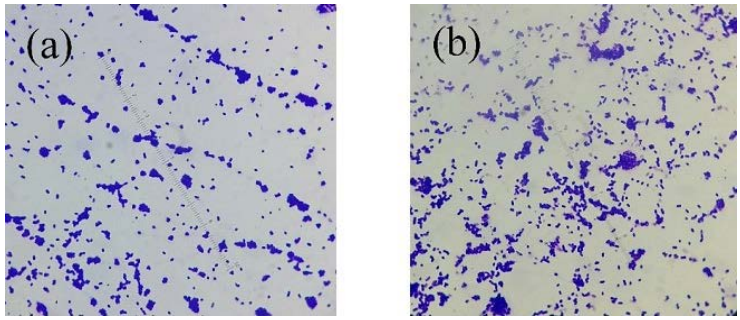

Figure 8.6: (a) and (b) show the growth of *Escherichia coli* on two nano-ripple glass substrates when grown over the bar magnets.

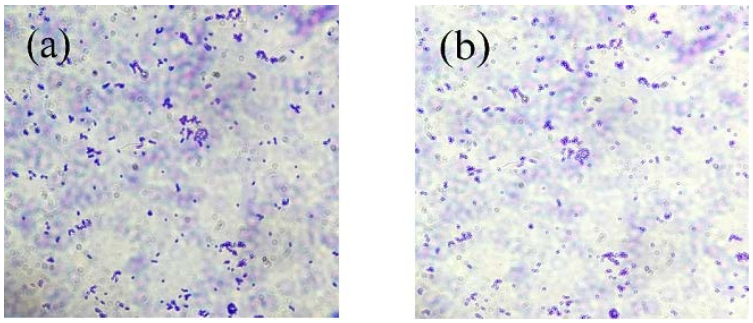

Figure 8.7: (a) and (b) show the growth of *Escherichia coli* on two nano-ripple glass substrates in a uniform magnetic field.

Magnetic field effects on the growth of *Pseudomonas aeruginosa* bacteria reveals similar results. Under the effect of a magnetic field, bacterial colonies were smaller on a glass nano-ripple surface, Figure 8.8. As seen in Figure 8.9, on a plain glass surface, the attachment of the bacteria is relatively less. There is more growth on nano-ripple structures.

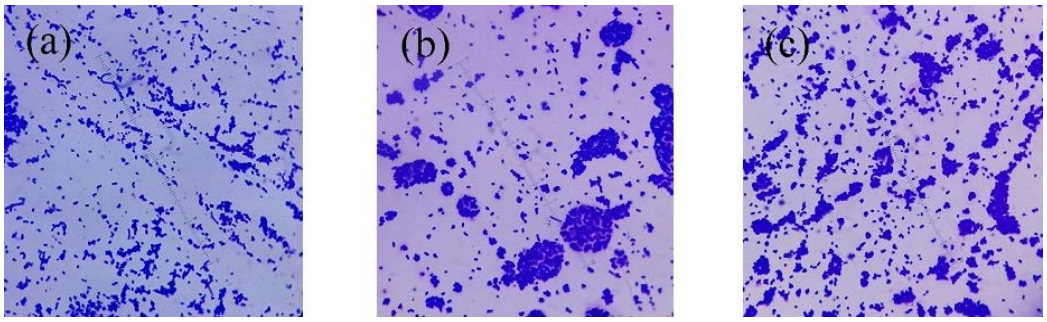

Figure 8.8: (a), (b) and (c) show the growth of *Pseudomonas aeruginosa* on three nano-ripple substrates when grown on the bar magnets.

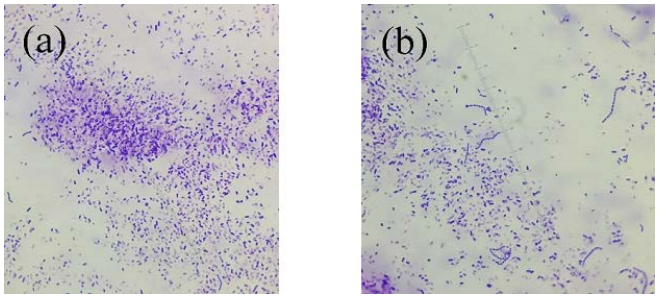

Figure 8.9: (a) and (b) show the growth of *Pseudomonas aeruginosa* on two plain glass surfaces in the absence of magnetic field.

However, there was more growth around the glass both in the case of plain or nanostructure surface instead of over the surface. Indicating bacteria grow better without contact with the glass nano-ripple surface, Figure 8.10.

Figure 8.10: Shows significantly more bacterial growth around the glass nano-ripple structure.

8.5 Conclusions

Nano-ripple glass patterns formed by gas cluster ion beam irradiation show more bacterial growth than on a plain glass slide. The nano-ripple pattern seems to cause hindrance to the movement of the bacteria and causes it to stick on the uneven surface. Bacterial colonies then start to grow, they are more in number, and larger in size on the nanostructure.

A comparison of nano-ripple grown bacteria has shown different behavior inside and outside the magnetic field. The magnetic field seems to suppress bacterial growth on the nanostructures in addition to reducing the size of the bacterial colonies. Bacteria growing on the nanostructures outside the magnetic field tends to make larger colonies. The bacteria overall avoids adhesion to glass and prefers growing without contact with the glass surface.

This study was done for the rod-shaped Gram-negative bacteria. These effects may be different for different bacterial strains. Moreover, extremely weak magnetic field strength shows a perturbative effects on the growth rate only, whereas larger fields may entirely different effects.

Chapter 9

Influence of Weak Magnetic Field on the Growth of Different Bacterial Species

Bacterial adhesion and growth is affected by many factors, including topography and material of the surface, associated ion flow, physical conditions of the environment, and chemical features. Proliferation of the adherent bacteria and synthesis of the EPS matrix is influenced by the presence of a magnetic field. It is therefore important for us to understand interaction between biological systems and magnetic fields [112, 113]. Bacterial cells are enclosed by a few nanometer thick cell membrane which constitutes of ionic channels that regulates ion flow through the membrane. The movement of these ions across the membrane forms the basis of survival and growth of the cell. Living organisms have been exposed to electric and geomagnetic fields since the beginning of life and numerous effects of magnetic field impact have been reported on these organisms [102, 106, 107].

Apart from earth's magnetic field, a variety of man-made magnetic fields exist in our everyday surroundings. From electrical appliances, high-voltage power lines, and weak magnetic fields, such as cell phones, laptops, and other frequently used electronic devices. The understanding of biofilm formation and bacterial growth in the influence of magnetic field has been of considerable interest in food and healthcare industry, as well as in academic research. It was not known until recently

that low frequency magnetic and electric fields can have impact on the physiology or biology of a cell [84, 96-99, 108]. Both stimulatory and inhibitory effects of weak fields on the growth rate has been observed during several investigations [101, 103]. Certain cells have magnetic structures and in the presence of a magnetic field, their enzymatic activities and RNA machinery may function differently. This might result in affecting their growth rate, mutation frequency, and other cell factors. It has also been suggested that the magnetic fields inactivate pathogenic microbes [104, 105]. A number of studies report the inhibition in the bacterial growth under the influence of an electromagnetic field [114-117].

We have investigated the details of bacterial adhesion and growth on plain glass and nano-ripple glass surfaces in the previous chapter. This study deals with the growth of different species of bacteria in a test tube after being treated in different conditions of magnetic field. We outline the results of an experimental investigation on how weak static, non-homogenous and alternating magnetic fields can affect the growth dynamics of bacteria species of *Escherichia Coli, Pseudomonas Aeruginosa, Staphylococcus Epidermidis,* and *Staphylococcus Aureus.*

All culture plates including control cultures and the ones in the magnetic field were simultaneously grown at room temperature, 20℃. We exposed the four bacterial strains for three days in four different magnetic field conditions using liquid nutrient broth and agar as the growth medium. The two Gram-positive (*Staphylococcus Epidermidis, Staphylococcus Aureus)* and the two Gram-negative (*Escherichia Coli, Pseudomonas Aeruginosa*)) species previously exposed to the

magnetic fields and the controls were then grown in broth cultures in the test tubes in the incubator. Growth rate was measured by optical density (OD) measurements every one to two hours at 650 nm. Magnetic field conditions prominently affect the rate of growth of bacteria originally grown in liquid nutrient broth and agar environment differently. The chapter is organized such that we first describe the preparation of bacteria culture and the experimental set up used in the study. Later section is devoted to discussing the experimental procedure and the results of our investigation. In the end main results are summarized.

9.1 Preparation of Bacteria Culture

Samples were prepared beginning with the cultivation of mother cultures from dehydrated solutions. A small amount of rehydrating medium was then added in the containers of the dehydrated bacteria. It was transferred into separate tubes of rehydrating medium. A small volume of the solution was then spread onto agar plates after the tubes were vortexed assuring proper mixing. The plates were moved into a 37 °C incubator to grow. The plates were taken out of the incubator once the colonies were visible. A single colony was carefully removed from the plate and placed into a tube filled with nutrient broth. The tube was kept in the shaking incubator until sufficient growth was seen. Again a small amount of the solution was pipetted and spread onto agar plates. The above process of incubation and subsequent acquisition of an individual colony was repeated to guarantee consistency in the bacteria. This process was conducted for each selected species to obtain the mother cultures with limited variance. These mother cultures were

used to prepare the experimental and control samples. We ran each species separately due to spatial restraints as well as the cumbersomely large number of samples.

9.2 Magnetic field setup

We accomplished four different magnetic field configurations in order to search for varying effects.

9.2.1 Bar Magnets Configuration

We accomplished four different magnetic field configurations in order to search for varying effects. The first of these was created by aligning alternately a series of twelve bar magnets in a line such that each pole is adjacent to the opposite poles as shown in Figure 9.1. Each individual bar magnet was approximately 0.75 inches wide and 6 inches long, building the total dimension of the rectangular arrangement to approximately 9 inches wide and 6 inches long. This magnetic field arrangement created a field strength according to position that was in the range of |3G| to |5G|.

Figure 9.1: Bar magnet arrangement

9.2.2 Round Magnets

The second and simplest magnet configuration was made using eight small, individual circular, and relatively stronger magnets. These magnets had a diameter of approximately 1 and 7/16 inches. Each magnet was numbered individually, and kept separate for use and measurements. Because of the simplicity of fields generated by each individual round magnet, an approximate field strength can be measured without need for ranges of values. The approximate field measurements for each round magnet was about 75 G, and the magnet can be seen in Figure 9.2.

Figure 9.2: Round magnets

9.2.3 Uniform Magnetic field Arrangement

For the uniform magnetic field setup, we used a series of eight 200 turn coils laid in order to achieve a vertical oriented cylinder configuration. One terminal of a direct current power supply was plugged into the bottom coil and the other was connected to the top coil. This created what was essentially a large solenoid,

allowing a nearly uniform field to develop within the interior region of the coils. Using a magnetic field sensor, we tuned the DC voltage to a magnetic field of approximately 5 G in the center of the solenoid. This uniform magnetic field setup can be seen in Figure 9.3.

Figure 9.3: Uniform field configuration

9.2.4 Oscillating Magnetic field Formation

The oscillating magnetic field was set up like an electromagnet, similar to the configuration used for the uniform field. The difference from the previous setup is that it was connected to a programmable power supply, which varied the magnetic field with time. The system was set up to alternate between two voltage settings every 60 seconds. The two settings were tuned to allow for a near-constant field of strengths approximately 0.5 G and 5 G, with 0.5 G being detected when the system was on its lowest setting. This slowly varying, oscillatory magnetic field setup can

be seen in Figure 9.4. We grew the control bacteria in the same room at the same time as the experimental samples to keep the same environmental conditions.

Figure 9.4: Oscillating field configuration

9.3 Experimental Procedure

Experimental samples were prepared using a pipette and sterilized plates. Half of the plates were remained unfilled while the other half contained agar. Prior to inoculation the unfilled plates had a sterilized, flat circular glass coverslip placed into the center of the plate. Each set of plates was then inoculated with bacteria pipetted from the mother culture, including the plates that did not contain agar. After inoculation, sterilized glass cover slips were placed on the site of inoculation on the agar plates. The plates with agar have a cover slip on top of the bacteria culture and the one without agar plates will grow bacteria on the glass cover slip. The two types of media were chosen to illustrate if the bacterial growth depended

on the growth media. After each plate was carefully labeled, it was then placed at the respective position in the previously described four magnetic field environments together with the control samples at room temperature. After three days in their respective environments, the plates were then removed in order to be processed.

Each plate was scraped for bacteria carefully targeting from one individual colony, which was then inoculated into the nutrient broth in sterile tubes. When the measurement process was ready to begin, each sample was vortexed and 50 µl of sample from each test tube was inoculated into three fresh test tubes with 5 ml of broth. After preparation was complete, the numerous low concentration experimental samples were then placed into a shaking incubator set to 37 °C. The samples were then periodically removed from the incubator temporarily for taking the optical density reading on the optical spectroscope. After each test tube was individually measured, the entire set of bacteria was then placed back into the incubator until the time of the next scheduled measurement, which was about after every two hours approximately. This process of taking periodic measurements continued for a 24-36 h depending on the bacterial strain.

The purpose of the present study was to investigate the sustained effect of different weak magnetic field conditions upon the growth rate of bacteria outside the magnetic field. The effect of specific magnetic field on the growth pattern of the various strains of bacteria was demonstrated as inferred by optical density measurements. The device used to take optical measurements of the bacteria was a Spectronix 20D+. 13 x 100 mm Pyrex test tubes (with caps) were involved for this

experiment in order to fit into the spectrometer. Optical properties of the mixture changes as the bacteria grows in a test tube. Broth has low absorbance at 650 nm and the increase in optical density is an indicative of bacterial growth. The spectrometer was set to take measurements at 650 nm, and calibrated using “blank” test tubes only containing broth.

9.4 Bacterial Growth Curves

We plotted the growth curves for each bacterial specie which was originally grown in different types of magnetic fields, both in nutrient broth and agar on a glass coverslip, and was later cultured in the test tubes with the same broth simultaneously under the same conditions. These results are also compared with the bacterial culture which has never been exposed to magnetic field and is labelled as control, hereafter.

To investigate the detailed effect of magnetic field on bacterial growth, we plot the optical density of bacteria as a function of time for almost 36 hours to clearly distinguish between the effects of different types of fields on different species.

9.4.1 Escherichia Coli

We plot the optical density of *Escherichia coli* as a function of time (in minutes) in Figure 9.5. This figure represents two graphs. Figure 9.5a gives a comparison of *Escherichia coli* originally grown over the agar medium in different fields at room temperature and then cultured in broth and the relative growth of all the field exposed samples was studied at 37℃. Figure 9.5b gives a similar set of plots for

Escherichia coli which were originally grown over the broth in various types of above mentioned magnetic fields.

This figure clearly shows that different magnetic fields differently influence the growth depending on the type and strength of the magnetic field. The effect of bar magnets was small and the growth was comparable to the control whereas the effect of oscillating field is greater and minimum bacterial growth was seen. The growth pattern remains unchanged, overall. A general trend of a bacterial growth curve is followed by each set. However, the change from the control growth with time indicates that the effect of a magnetic field keeps multiplying with bacterial generations.

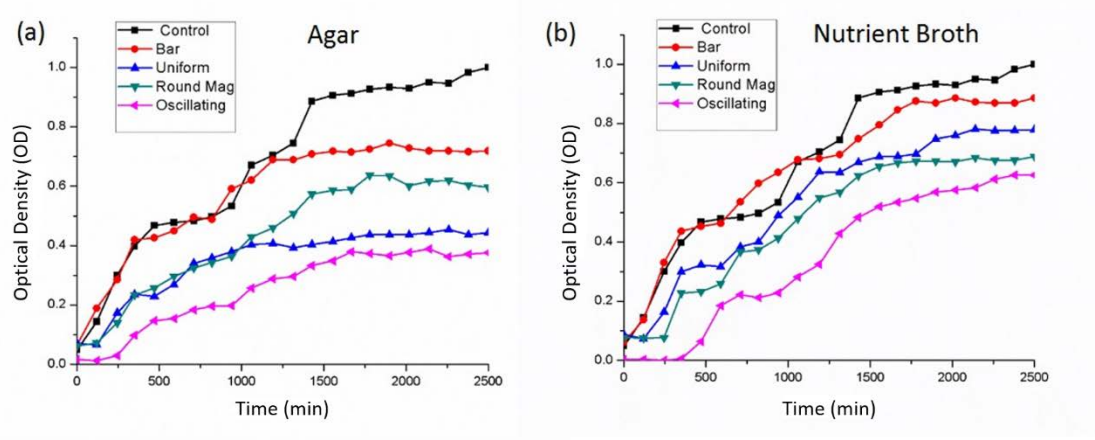

Figure 9.5: *Escherichia coli* growth for all four magnetic field configurations and the control for (a) agar and (b) nutrient broth samples.

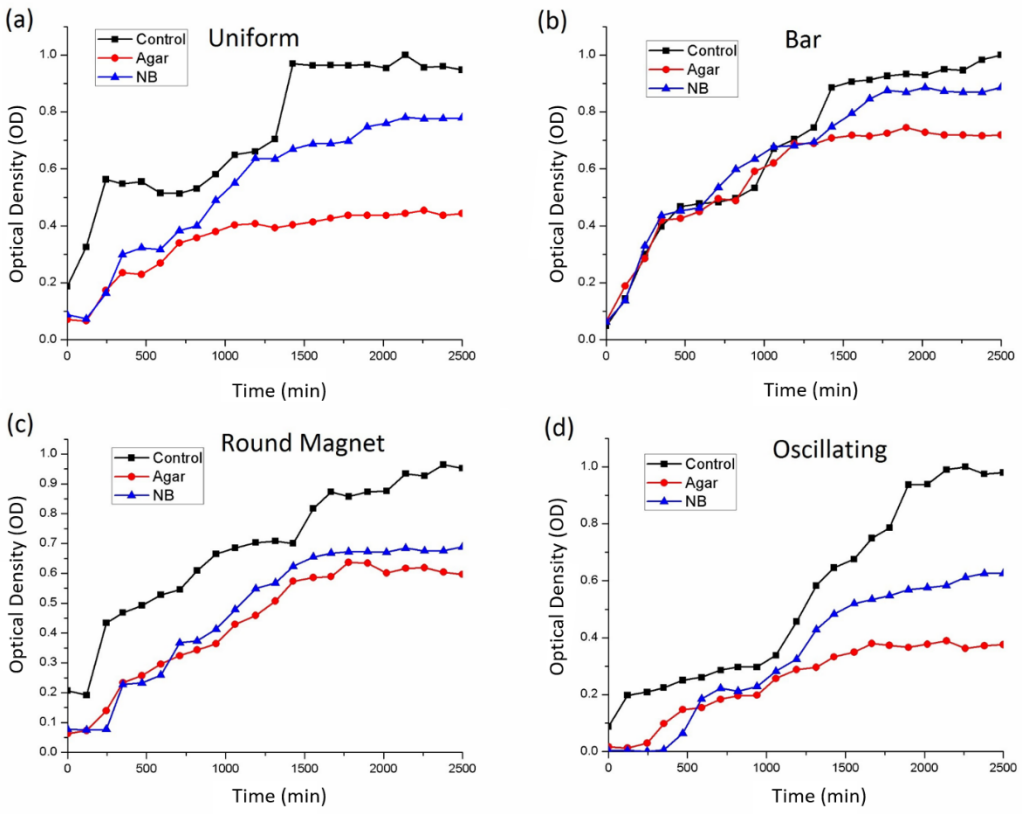

Figure 9.6: Comparing *Escherichia coli* growth of agar and nutrient broth samples in (a) uniform, (b) bar, (c) round magnet and (d) oscillating magnetic field setup.

As seen in Figures 9.6, the agar samples and nutrient broth data sets for each magnetic field environment were plotted together to compare the effect of growth medium in each type of magnetic field separately. The longer lag phase in some cases indicate that the bacteria was still adapting to its environment. Bacteria then grew exponentially until it reaches the stationary phase. Figure 9.6(a-d) shows a clear difference in bacterial growth between nutrient broth and agar. Samples grown in agar reached the saturation level significantly faster. The oscillating magnetic field exposed bacteria took the longest time to adapt to the periodically changing magnetic field environment, hence, a longer lag phase is observed. Also,

bacteria grown over the round magnets (relatively strong field) seemed to take more time to reach the stationary phase. The difference in the growth curves represents the effect of the nature of the medium and, the type and strength of magnetic field on the rate of bacterial cell division.

Initially, the bar magnetic field samples grow with much less variance from the control samples but in 6 h, the control samples begin to split off from the bar magnetic field curve. A lag phase was seen in a large proportion of the oscillating magnetic field samples. This implies a potential temporal effect may have taken place before the bacteria adapted to its environment. Bacteria takes longer time to adjust the alternating magnetic field. The alternating magnetic field gives *Escherichia coli* the hardest time to acclimate to the new environment because of the changing the physical condition in its surrounding. This is why the growth of the oscillating field samples is the slowest. It can be seen that the uniform and round magnetic field samples experience a smaller but noticeable lag phase. Of course oscillating field undergoes the longest lag phase for *Escherichia coli*. It is noticed that the growth rate is slower for the agar samples as compared to the bacteria grown in liquid nutrient broth. Justification of this behavior is related to the mobility of nutrients in the liquid broth as compared to jelly like agar. This mobility keeps increasing the difference in growth rate with time. It is also clearly seen that the difference between the control and the magnet-exposed bacterial growth is widened more rapidly as compared to the growth rate in a liquid and solid medium.

9.4.2 Staphylococcus Aureus

Similar kinds of results are obtained for *Staphylococcus aureus* in the sense that magnetic field exposure suppresses the growth overall. However the bacteria seems to enter into the stationary phase rather quicker than *Escherichia coli*. Thus the measurement time for these bacterial species was reduced to 24 h. Figure 9.7 shows that for *Staphylococcus aureus*, the gap among the bacterial growth curves in all the four different magnetic field configurations is more distinguishable than *Escherichia coli*. The oscillating field inhibits the growth to a much greater extent in comparison with the control. As can be seen, the gap between the two curves is large. Probably because the bacteria grows to its maximum level faster and thus the impact is more significant in a shorter time and the samples have a larger amount of variance to them compared to the other samples.

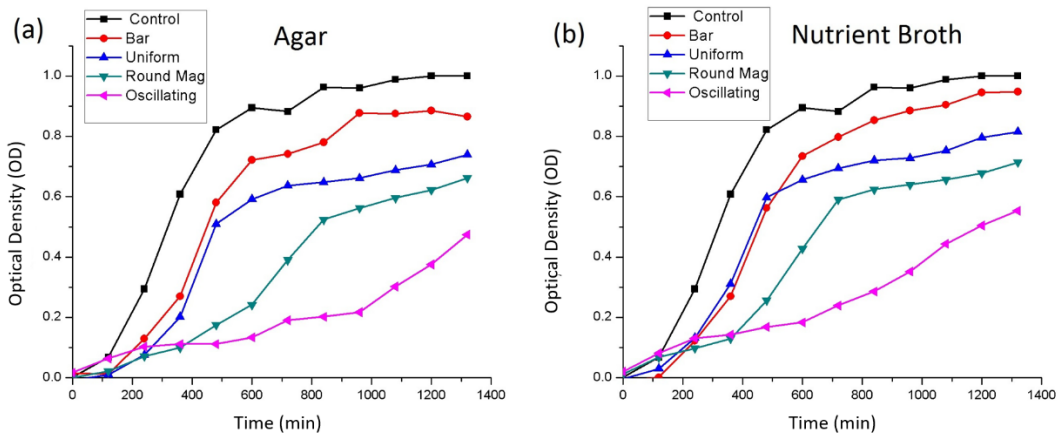

Figure 9.7: Plot of magnetic field treated *Staphylococcus aureus*, in (a) agar and (b) nutrient broth.

In Figure 9.7b the growth curve for uniform and bar magnetic fields are almost overlapping in the beginning. In after 8 h the behavior is distinguishable. The uniform field has a stronger inhibiting influence on the growth. Overall magnetic field treated bacteria showed a difference in the growth pattern just 3-4 h. The figures also demonstrate that *Staphylococcus aureus* has greater effect between different magnetic fields as compared to *Escherichia coli*.

Figure 9.8 shows the difference of growth rate between solid and liquid medium in the same magnetic field and compared it with the control. It is interesting to notice that *Staphylococcus aureus* does not show much difference between the behavior of agar and nutrient broth in all types of fields. However, nutrient broth growth is faster than agar, though small.

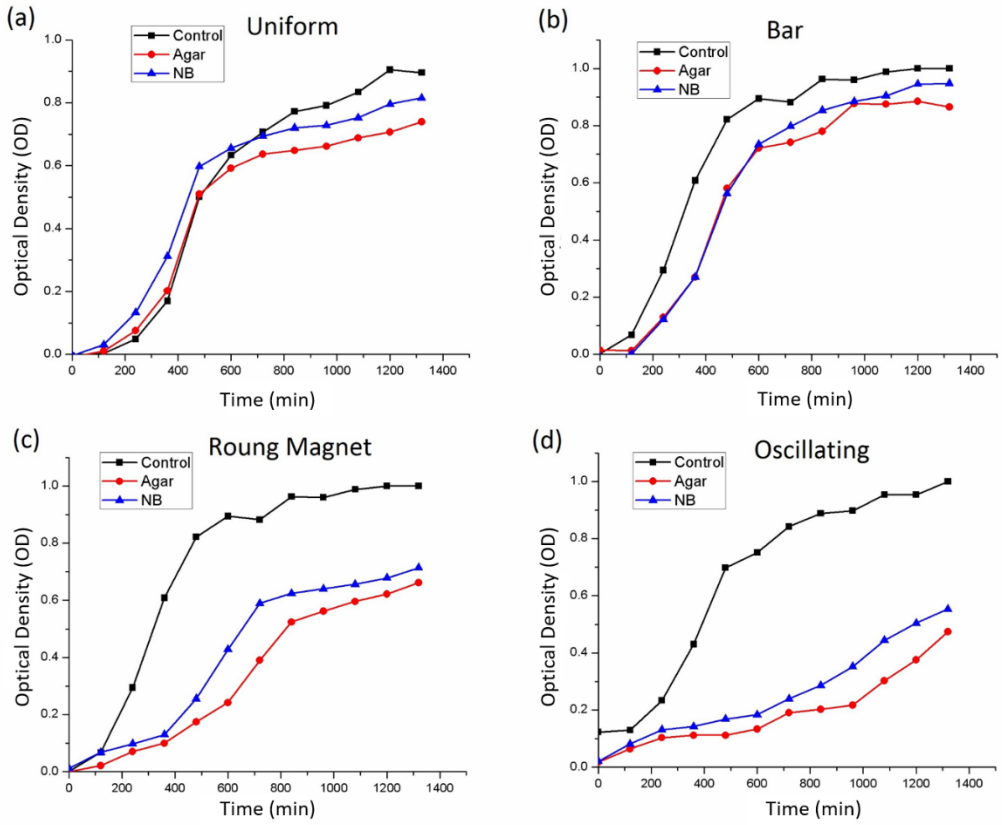

Figure 9.8: Separately comparing *Staphylococcus aureus* growth of agar and nutrient broth samples in (a) uniform, (b) bar, (c) round magnet and (d) oscillating magnetic field setup.

9.4.3 Staphylococcus Epidermidis

Figure 9.9 shows similar set of graphs for *Staphylococcus epidermidis*. Oscillating magnetic field exposed bacteria does not always exhibits the least growth. The round and oscillating magnetic field growth curves are competing with each other. There is an overlap between round and oscillating field curves. One is inhibiting the growth by alternating effect and not giving bacteria enough time to adapt to its environment and the other is due to higher strength of magnetic fields compared to the other samples. The round magnet data from these sets are largely similar with

the oscillating field except some slight variance. This result further reinforces the previously stated possibility of a potentially temporary effect for the round magnet samples as well for the case of *Staphylococcus epidermidis* bacteria. The data therefore strongly agrees with the possibility of a delayed growth rate effect taking place in both magnetic field environments. The round magnetic field and oscillating magnetic field environments are therefore both appealing subjects for further investigation into the effects of weak magnetic fields on *Staphylococcus epidermidis* bacteria.

Figure 9.10 shows relatively more suppression in growth due to exposure to the magnetic fields in agar samples but the separation between nutrient broth and agar growth curves was small compared to *Escherichia coli*. This result is comparable to *Staphylococcus aureus*. It is therefore probable that a difference in the type of broth medium causes a difference in magnetic field effect, possibly implying that the type of nutrient broth and oxygen level may be just as important a factor in low magnetic field environments as the field itself.

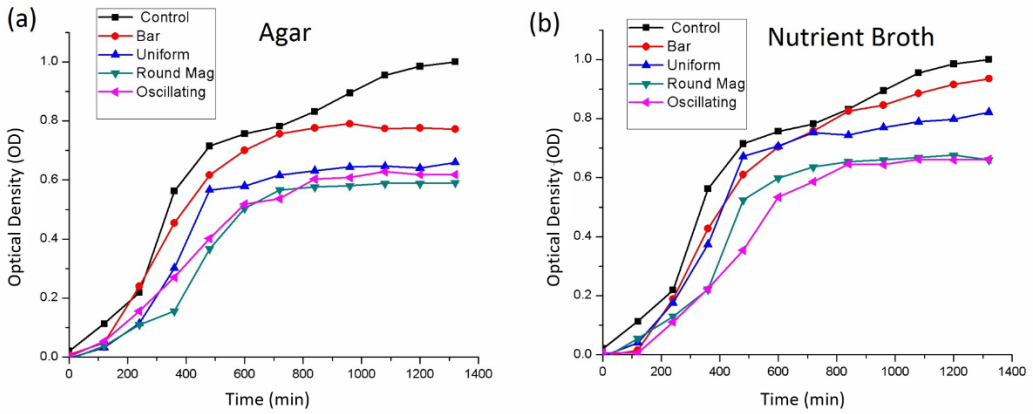

Figure 9.9: *Staphylococcus Epidermidis* growth for all four magnetic field configurations and the control for (a) agar and (b) nutrient broth samples.

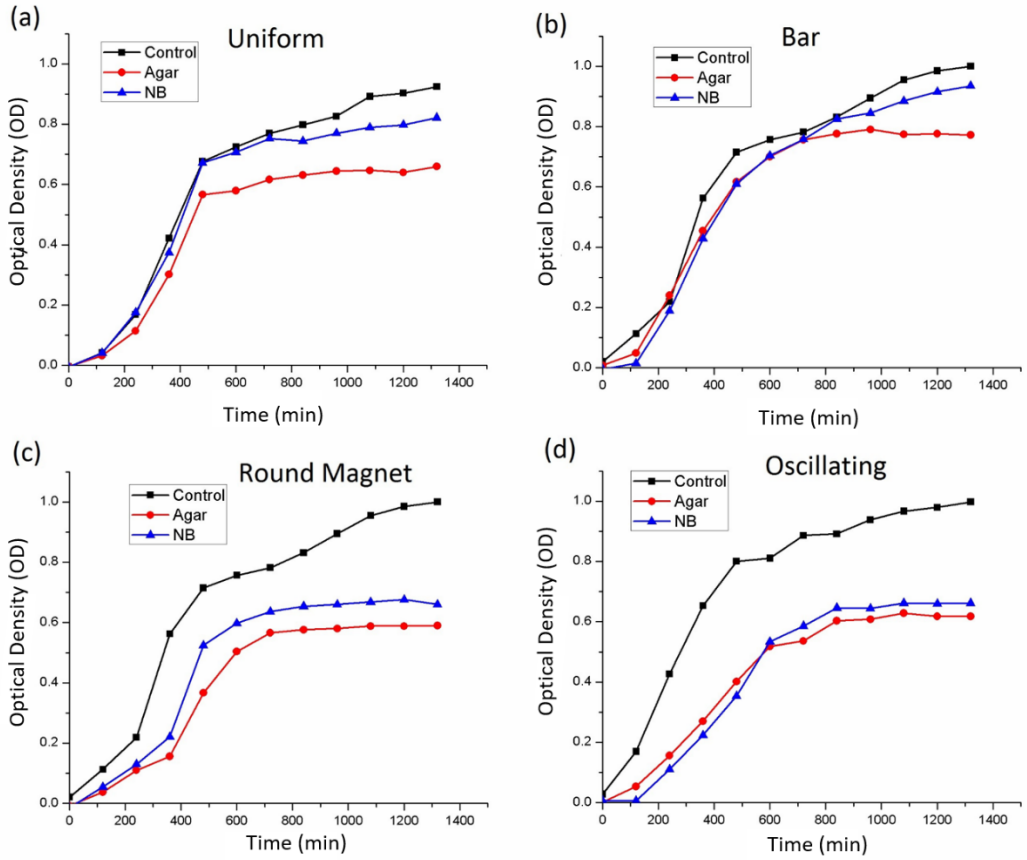

Figure 9.10: Comparing *Staphylococcus epidermidis* growth of agar and nutrient broth samples separately in (a) uniform, (b) bar, (c) round magnet, and (d) oscillating magnetic field setup.

9.4.4 Pseudomonas Aeruginosa

For *Pseudomonas aeruginosa* we only studied bacteria grown in liquid nutrient broth on the glass coverslip. It can be seen that *Pseudomonas aeruginosa* was not influenced by small changes in the field. The similarity of the uniform field to the bar magnet data and a small gap with the control sample growth curve further verifies the lack of change. Also in *Pseudomonas aeruginosa* not only does it takes

a longer time to start the process of cell division and experiences an extended lag phase, it also stays in the exponential phase for a longer time.

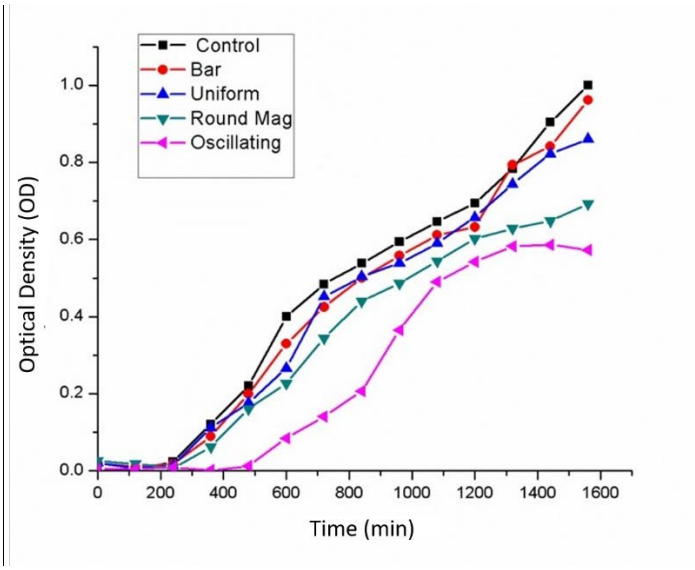

Figure 9.11: *Pseudomonas Aeruginosa* for all four magnetic field configurations and the control for nutrient broth samples.

Lastly, we examine the data for the oscillating magnetic field environment. The curve for each of the experimental sample sets are very similar except the oscillating growth curve, but each set can be seen to deviate from the control after a point. The experimental samples continued to grow up until the end of the measuring process. The bacteria treated in the oscillating field went to the stationary phase faster. The largest difference between control and the magnetic field treated samples is seen for the 0-5 Gauss oscillating field and is a good candidate for further *Pseudomonas aeruginosa* investigations.

9.5 Histogram

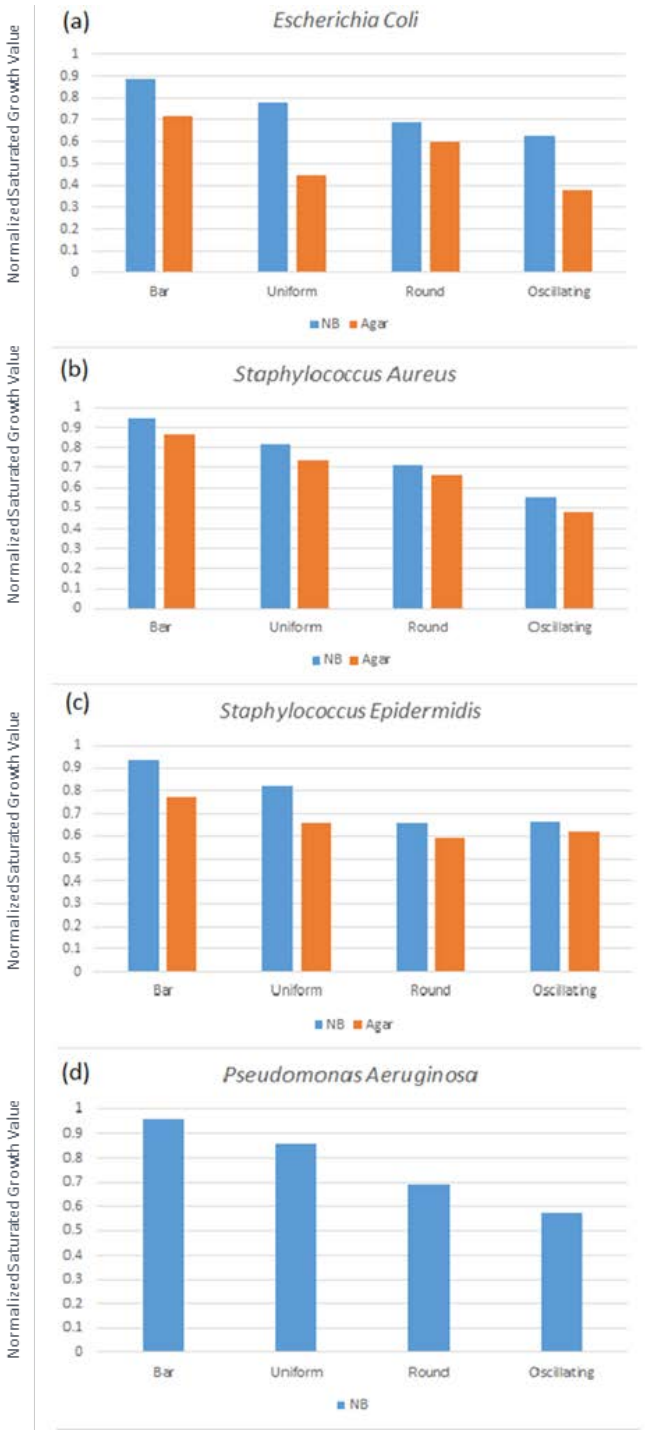

Figure 9.12: Saturation value of growth for (a) *Escherichia Coli*, (b) *Staphylococcus Aureus*, (c) *Staphylococcus Epidermidis* and (d) *Pseudomonas*

Aeruginosa in bar, uniform, round and oscillating magnetic fields for nutrient broth NB (in blue) and agar (in red). *Pseudomonas Aeruginosa* was studied in liquid medium alone. Control has a normalized value of one for each case.

Figure 9.12, gives a comparison of the suppression in growth of different bacterial species in solid (red) and liquid (blue) media originally grown over different setups of magnetic field. The growth of the control samples, where each bacteria was grown outside the field is normalized to one. A common feature of these curves is that the solid medium (agar) has lower maximum growth as compared to the cell growth in liquid medium. The saturation values for the bacterial species shows that it is not only the strength and type of the magnetic field which matters in the growth rate, different bacterial species are affected differently in different magnetic fields as well as the medium. Thus the growth depends on the kind of bacteria as well.

To summarize, it appears that a medium-dependent and magnetic field-dependent effect can be seen in the growth rate of all magnetic field exposed bacterial strains. The trend for each set of oscillating field is approximately similar to each other.

9.6 Summary and Overview

The above study of the growth rates of different magnetic field exposed bacterial strains shows that the magnetic field effect is sustained by bacteria even after the field is removed. We have found that this sustained effect of weak magnetic field negatively affects the growth of the bacterial species. The effect depends on the type of the magnetic field and also the environment. There is not much difference in the growth when the cultures are exposed to the weak uniform static field. The

growth rate for a culture subjected to alternating magnetic fields is significantly reduced in comparison with that of the control cultures and compared to other weak field influenced bacteria. This result is consistent in all four bacterial strains. Overall magnetic field inhibits the growth of bacterial species.

Bacteria grown in agar over magnets shows slower growth in the same medium as compared to the nutrient broth grown magnetic field exposed bacteria. We believe this general trend is due to the fluidity of nutrient broth which increases the availability of nutrients as compared to jelly-like sold agar medium. This effect is more distinguishable in *Escherichia coli*. The separation in the growth curves of different magnetic field growth trends is more pronounced in *Staphylococcus aureus* as compared to other bacterial. *Pseudomonas aeruginosa* shows minimum influence on the growth curves of the different magnetic field conditions except for the periodically changing magnetic field. For which it reaches the saturation level much faster than the rest.

List of Presentations

1. Participated in the Texas Center of Superconductivity at University of Houston Student Symposium 2017 *"Microbial growth on plain and nano-ripple glass in weak magnetic field"*

2. Presented at the APS March meeting in New Orleans, Louisiana in March, 2017 *"Weak magnetic field effect on the growth of bacteria on plain glass and nano-ripple glass pattern"*.

3. Participated in the Texas Center of Superconductivity at University of Houston Student Symposium 2016 *"Bio-applications of self-assembled nano ripple patterns fabricated by gas cluster ion beam"*.

4. Presented at the MRS meeting in Boston, Massachusetts Nov 27- Dec 4, 2016 *"Bacterial growth study on nano-ripple glass pattern fabricated by gas cluster ion beam irradiation"*.

5. Presented at the CAARI Conference Oct 30-Nov 4 2016 Fort Worth, Texas USA *"Cluster ion beam induced nano ripple structures and their biological applications"*.

6. Presented a poster at the APS March meeting in Baltimore, Maryland in March, 2016 *"Propagation of light in a dense medium"*.

7. Presented at the APS March meeting in Baltimore, Maryland in March, 2016 *"Detecting antibody-antigen reaction using nano-ripple gold LSPR based biosensor"*.

8. Presented at the APS March meeting in San Antonio, Texas in March, 2015 *"Cluster ion beam induced nano metallic rippled structures for localized surface plasmon resonance (LSPR) based sensors"*.

9. Presented at the CAARI Conference May 25-30 2014 San Antonio, Texas USA *"Ion beam and cluster ion beam engineered nano-metallic substrates for SPR based sensors"*.

10. Participated in the Texas Center of Superconductivity at University of Houston Student Symposium 2014 and Won 1st prize *"Cluster Ion Beam Induced Localized Surface Plasmon Resonance (LSPR) based sensors"*.

11. Presented in the class of Ion Beam Analysis 2013 on the topic of *"Proton Therapy for Cancer Treatment"*.

List of Publications

- Masood, S. and **Saleem, I.**, 2017 Propagation of electromagnetic waves in extremely dense media *International Journal of Modern Physics A (Accepted, in press).*

- **Saleem, I.**, Widger, W., and Chu, W.K., 2017 A New Technique to Detect Antibody-Antigen Reaction (Biological Interactions) on a Localized Surface Plasmon Resonance (LSPR) Based Nano Ripple Gold Chip *Applied Surface Science* **411** 205–209.

- **Saleem, I.** and Chu, W.K., 2016 Gold nano-ripple structure with potential for bio molecular sensing applications *Sensing and Bio-sensing Research* **11(1)** 14-19.

- **Saleem, I.**, Tilakaratne, B.P., Li, Y., Bao, J., Wijesundera, D.N., and Chu, W.K., 2016 Cluster ion beam assisted fabrication of metallic nanostructures for plasmonic applications *Nuclear Instruments and Methods in Physics Research Section B* **380** 20-25.

- **Saleem, I.**, Masood, S., Smith, D., and Chu, W.K., Bacterial growth on nano-ripple glass substrate under the influence of weak magnetic fields (*Submitted March 2017).*

- **Saleem, I.**, Masood, S., Smith, D., and Chu, W.K., Growth Pattern of Magnetic Field Treated Bacteria (*Submitted July 2017).*

Invention Disclosure (Filed Patent Application)

- Title: LOCALIZED SURFACE PLASMON RESONANCE-BASED METALLIC NANO RIPPLE BIOSENSORS
  Application no: 62/402,533, File date: September 30, 2016
  Reference no.: UHID 2016-052, RS Reference no.: 20005.0013.PZUS00

Bibliography

1. Veloso, A. J., X. R. Cheng, and K. Kerman 2012 "Electrochemical biosensors for medical applications." Biosensors for Medical Applications, 3-40.

2. Tombelli, S. 2012 "Piezoelectric biosensors for medical applications." Biosensors for Medical Applications, 41-64.

3. Claussen, J. C., J. Shi, C. S. Rout, M.S. Artiles, M. M. Roushar, M.C. Stensberg, D. M. Porterfield, And T.S. Fisher. 2012 “Nano-sized biosensors for medical applications.” Biosensors for Medical Applications, 65-102.

4. Misun, P. M., J. Rothe, Y. R. F. Schmid, A. Hierlemann, and O. Frey. 2016 "Multi-analyte biosensor interface for real-time monitoring of 3D microtissue spheroids in hanging-drop networks." Microsystems & Nanoengineering 2 16022.

5. Kim, Y. H., J. S. Park, and H. I. Jung. 2009 "An impedimetric biosensor for real-time monitoring of bacterial growth in a microbial fermentor." Sensors and Actuators B: Chemical, 138(1) 270-77.

6. Binkowski, B. F., F. Fan, and K. V. Wood. 2011 “Luminescent biosensors for real-time monitoring of intracellular cAMP.” Methods in Molecular Biology, (756) 263-71.

7. Mayer, K. M. and J. H. Hafner. 2011 “Localized surface plasmon resonance sensors.” Chemical Review, 111(6) 3828-3857.

8. Haynes, C. L. and R. P. Van Duyne. 2002 “Plasmon Scanned Surface-Enhanced Raman Scattering Excitation Profiles.” Materials Research Society Symposium, 728.

9. Stiles, P. L., J. A. Dieringer, N. C. Shah, and R. P. Van Duyne 2008 “Surface Enhanced Raman Spectroscopy.” Annual Review of Analytical Chemistry, 1 601–26.

10. Jung, H., B. Koo, J. Y. Kim, T. Kim, H. J. Son, B. Kim, J. Y. Kim, D. K. Lee, H. Kim, J. Cho, and M. J. Ko 2014 “Enhanced photovoltaic properties and long-term stability in plasmonic dye-sensitized solar cells via noncorrosive redox mediator ACS.” Applied Materials & Interfaces, 6 (21) 19191–19200.

11. Uddin, A. and X. Yang. 2014 “Surface plasmonic effects on organic solar cells.” Journal of Nanoscience and Nanotechnology, 14(2) 1099-1119.

12. Luther, J. M. 2011 “Localized surface plasmon resonances arising from free carriers in doped quantum dots.” Nature Materials, 10 361–366.

13. Kim, K., D. J. Kim, S. Moon, D. Kim, and K. M. Byun. 2009 “Localized surface plasmon resonance detection of layered biointeractions on metallic subwavelength nanogratings.” Nanotechnology, 20(31).

14. Merlen, A. and F. Lagugne´-Labarthet. 2014 “Imaging the Optical Near Field in Plasmonic Nanostructures.” Applied Spectroscopy, 68(12) 1307-1326.

15. Huang, X. X., Cao, Z., Liu, Y. L., Dai, Y. M., Zeng, J. L., Yang, R. H., and Takei, H. 2010 “Interface between Nanophotonics and Biotechnology: How the Near-Field Can Boost Proteomics Based on LSPR Nano Sensor.” Advanced Materials Research, 139-141 1554-1557.

16. Law, W. L. 2011 “Nanostructure materials for biosensing and bioimaging applications.” Thesis (Ph.D.) State University of New York at Buffalo, Dissertation Abstracts International, 72-04 Section: B, 161.

17. Huang, X. and M. A. El-Sayed. 2011 “Plasmonic photo-thermal therapy (PPTT).” Alexandria Journal of Medicine, 47(1) 1–9.

18. Willets, K.A. and R. P Van Duyne. 2007 “Localized surface plasmon resonance spectroscopy and sensing.” Annual Review of Physical Chemistry, 58 267-297.

19. Yamada, I., W. Brown, J. Norhby, and M. Sosnowski. 1993 “Surface modification with gas cluster ion beams.” Nuclear Instruments and Methods in Physics Research B, (79) 223-226.

20. Yamada, I., J. Matsuo, Z. Insepov, and M. Akizuki. 1995 “Surface modifications by gas cluster ion beams.” Nuclear Instruments and Methods in Physics Research B, (106) 165-169.

21. Kirkpatrick, A. 2003 "Gas cluster ion beam applications and equipment." Nuclear Instruments and Methods in Physics Research Section B: Beam Interactions with Materials and Atoms, (206) 830-37.

22. Toyoda, N. and Yamada, I. 2008 “Gas Cluster Ion Beam Equipment and Applications for Surface Processing.” IEEE Transactions on Plasma Science, (36) 1471-1488.

23. Hwang, C. C, J. G. Chang, G. J. Huang, and S. H. Huang. 2002 "Investigation of cluster size and cluster incident energy effect on film surface roughness for ionized cluster beam deposition." Journal of Applied Physics, 92(10) 5904-912.

24. Haberland, H., M. Karrais, M. Mall, and Y. Thurner. 1992 “Thin films from energetic cluster impact: A feasibility study” Journal of Vacuum Science & Technology A, (10) 3266.

25. M. Navez, C. Sella, and D. Chaperot. 1962 "Microscopie electronique - etude de lattaque du verre par bombardement ionique." Comptes Rendus Hebdomadaires Des Seances De L Academie Des Sciences, 254 (2), 240-248.

26. Bradley, R. M. and Harper, J. M. E. 1988 "Theory of ripple topography induced by ion-bombardment", Journal of Vacuum Science & Technology a-Vacuum Surfaces and Films, 6 (4), 2390-2395.

27. Yamada, I. 2001 "Materials processing by gas cluster ion beams", Materials Science & Engineering R-Reports, 34(6), 231-295.

28. Takaoka, G. H., H. Ryuto, and M. Takeuchi. 2012 "Surface irradiation and materials processing using polyatomic cluster ion beams." Journal of Materials Research, 27(5) 806-21.

29. Sumie, K., N. Toyoda, and I. Yamada. 2013 "Surface morphology and sputtering yield of SiO2 with oblique-incidence gas cluster ion beam." Nuclear Instruments and Methods in Physics Research Section B: Beam Interactions with Materials and Atoms, 307 290-93. doi:10.1016/j.nimb.2013.01.087.

30. Yang, L., M. P. Seah, and I. S. Gilmore. 2012 “Sputtering Yields for Gold Using Argon Gas Cluster Ion Beams.” The Journal of Physical Chemistry, 116(44) 23735-23741.

31. Chen, H., F. Chen, X. M. Wang, X. K. Yu, J. R. Liu, K. B. Ma, W. K. Chu, H. H. Cheng, I. S. Yu, Y. T. Ho, and K. Y. Horng. 2005 "Smoothing of $Si_{0.7}Ge_{0.3}$ virtual substrates by gas-cluster-ion beam." Applied Physics Letters, 87(10) 103504.

32. Toyoda, N. and Yamada, I. 2012 "Gas Cluster Ion Beam Technology for Nano-Fabrication." Advances in Science and Technology, 82 1-8.

33. Tilakaratne, B.P. 2012 “Self-Assembled nano-Patterns by Gas Cluster Ion Beam Bombardment.” Ph.D. Dissertation, University of Houston.

34. Hongyan, L. 2015 “Chemically synthesized noble metal nanostructures for plasmonics.” Nanotechnology Reviews, 4(3) 289-302.

35. Petryayeva, E. and Krull, U.J. 2011 “Localized surface plasmon resonance: nanostructures, bioassays and biosensing-a review.” Analytica Chimica Acta, 706(1) 8-24.

36. Lu, X., M. Rycenga, S. E. Skrabalak, B. Wiley, and Y. Xia. 2009 “Chemical synthesis of novel plasmonic nanoparticles.” Annual Review of Physical Chemistry, 60 167-92.

37. Takeda, Y., O. A. Plaksin, H. Wang, K. Kono, N. Umeda, and N. Kishimoto. 2006 “Surface Plasmon Resonance of Au Nanoparticles Fabricated by Negative Ion Implantation and Grid Structure toward Plasmonic Applications.” Optical Review, 13(4) 231-234.

38. Seo, H.W., Q. Y. Chen, I. A. Rusakova, Z. H. Zhang, D. N. Wijesundera, S. W. Yeh, X. M. Wang, L. W. Tu, N. J. Ho, Y. G. Wu, H. X. Zhang, W. K. Chu. 2012 “Formation of silver nanoparticles in silicon by metal vapor vacuum arc ion implantation.” Nuclear Instruments and Methods in Physics Research Section B: Beam Interactions with Materials and Atoms, 292 50-54.

39. Wijesundera, D. N., I. Rajapaksa, X. Wang, J. R. Liu, I. Rusakova, and W. K. Chu. 2013 “Ion beam engineered nano silver silicon substrates for surface enhanced Raman spectroscopy.” Journal of Raman Spectroscopy, 44 1014-1017.

40. Alexandra, B. 2009 “Plasmonic components fabrication via nanoimprint.” Journal of Optics A: Pure and Applied Optics, 11(11) 114001.

41. Rechberger, W., A. Hohenau, A. Leitner, J.R. Krenn, B. Lamprecht, and F.R. Aussenegg. 2003 “Optical properties of two interacting gold nanoparticles Optics Communications.” 220(1) 137-141.

42. Pisarenko, A. N., W. U. Spendel, R. T. Taylor, J. D. Brown, J. A. Cox, and G. E. Pacey. 2009 “Detection of ozone gas using gold nanoislands and surface plasmon resonance.” Talanta, 80(2) 777-80.

43. Gupta, G., D. Tanaka, Y. Ito, D. Shibata, M. Shimojo, K. Furuya, K. Mitsui, and K. Kajikawa. 2009 “Absorption spectroscopy of gold nanoisland films: optical and structural characterization.” Nanotechnology, 20(2) 025703.

44. Kosiorek, A., W. Kandulski, H. Glaczynska, and M. Giersig. 2005 “Fabrication of nanoscale rings, dots, and rods by combining shadow nanosphere lithography and annealed polystyrene nanosphere masks.” Small, 1(4) 439-44.

45. Wiley, B. J., D. J. Lipomi, J. Bao, F. Capasso, and G. M. Whitesides. 2008 “Fabrication of surface plasmon resonators by nanoskiving single-crystalline gold microplates.” Nano Letters, 8(9) 3023-8.

46. Xu, Q., J. Bao, F. Capasso, and G. M. Whitesides. 2006 “Surface plasmon resonances of free-standing gold nanowires fabricated by nanoskiving.” Angewandte Chemie International Edition, 45(22) 3631-5.

47. Atwater, H.A. and Polman, A. 2010 “Plasmonics for improved photovoltaic devices.” Nature Materials, 9(3) 205-13.

48. Pillai, S., K. R. Catchpole, T. Trupke, and M. A. Green. 2007 “Surface plasmon enhanced silicon solar cells.” Journal of Applied Physics, 101(9) 093105.

49. Lim, S. H., W. Mar, P. Matheu, D. Derkacs, and E. T. Yu. 2007 “Photocurrent spectroscopy of optical absorption enhancement in silicon photodiodes via scattering from surface plasmon polaritons in gold nanoparticles.” Journal of Applied Physics, 101(10) 104309.

50. Allen, L. P., Z. Insepov, D. B. Fenner, C. Santeufemio, W. Brooks, K. S. Jones, and I. Yamada. 2002 “Craters on silicon surfaces created by gas cluster ion impacts.” Journal of Applied Physics, 92(7) 3671.

51. Lozano, O., Q. Y. Chen, B. P. Tilakaratne, H. W. Seo, X. M. Wang, P. V. Wadekar, P. V. Chinta, L. W. Tu, N. J. Ho, D. Wijesundera, and W. K. Chu. 2013 “Evolution of nanoripples on silicon by gas cluster-ion irradiation.” AIP Advances, 3(6) 062107-062107-10.

52. Toyoda, N., T. Mashita, and I. Yamada. 2005 “Nano structure formation by gas cluster ion beam irradiations at oblique incidence.” Nuclear Instruments & Methods in Physics Research Section B-Beam Interactions with Materials and Atoms, 232 212-216.

53. Yamada, I. 1991 “New horizons in material processing.” ICB Proceedings of 14th Symposium on Ion Sources Ion-Assisted Technology, Tokyo, Japan 227-235.

54. Yamada, I. 2015 “Materials Processing by Cluster Ion Beams: History, Technology, and Applications.” CRC Press, ISBN 9781498711753 - CAT# K25080.

55. Chu, W. K., Y. P. Li, J. R. Liu, J. Z. Wu, S. C. Tidrow, N. Toyoda, J. Matsuo, and I. Yamada. 1998 “Smoothing of YBa2Cu3O7−δ films by ion cluster beam bombardment.” Applied Physics Letters, 72(2) 246-248.

56. Yamada, I. 1995 “A short review of ionized cluster beam technology.” Nuclear Instruments & Methods in Physics Research Section B-Beam Interactions with Materials and Atoms, 99(1-4) 240-243.

57. Tilakaratne et al. 2016 “Investigation of self-assembled gold nano-ripple formation during gas cluster ion beam bombardment” Submitted.

58. Haes, A.J. and Van Duyne, R.P. 2002 “A Nanoscale Optical Biosensor: Sensitivity and selectivity of an approach based on the localized surface plasmon resonance spectroscopy of triangular silver nanoparticles.” Journal of the American Chemical Society, 124 (35) 10596–10604.

59. Sepúlveda, B., P. C. Angelomé, L. M. Lechuga, and L. M. Liz-Marzán. 2009 "LSPR-based nanobiosensors." Nano Today, 4 244-251.

60. Nath, N. and A. Chilkoti. 2004 "Label-Free Biosensing by Surface Plasmon Resonance of Nanoparticles on Glass: Optimization of Nanoparticle Size." Analytical Chemistry, 76 (18) 5370–5378.

61. Hutter, E. and J. H. Fendler. 2004 "Exploitation of Localized Surface Plasmon Resonance" Advanced Materials, 16 1685-1706.

62. Haes, A. J. and R. P. Van Duyne. 2004 "A unified view of propagating and localized surface plasmon resonance biosensors." Analytical and Bioanalytical Chemistry, 379 920-30.

63. Okamoto, T., I. Yamaguchi, and T. Kobayashi. 2000 "Local plasmon sensor with gold colloid monolayers deposited upon glass substrates." Optics Letters, 25(6) 372-4.

64. Jeong, H. H., S. K. Lee, J. H. Park, N. Erdene and D. H. Jeong. 2011 "Fabrication of fiber-optic localized surface plasmon resonance sensor and its application to detect antibody-antigen reaction of interferon-gamma." Optical Engineering, 50(12) 124405.

65. Li, X., L. Jiang, Q. Zhan, J. Qian, and S. He. 2009 "Localized surface plasmon resonance (LSPR) of polyelectrolyte-functionalized gold-nanoparticles for bio-sensing." Colloids and Surfaces A: Physicochemical and Engineering Aspects, 332 172-179.

66. Saleem, I., B. P. Tilakaratne, Y. Li, J. Bao, D. N. Wijesundera, and W. K. Chu. 2016 "Cluster ion beam assisted fabrication of metallic nanostructures for plasmonic applications." Nuclear Instruments & Methods in Physics Research Section B-Beam Interactions with Materials and Atoms, 380 20-25.

67. Makeev, M. A., R. Cuerno, and A. L. Barabási. 2002 "Morphology of ion-sputtered surfaces." Nuclear Instruments & Methods in Physics Research Section B-Beam Interactions with Materials and Atoms, 197 (3-4) 185-227.

68. Miller, M.M. and Lazarides, A.A., 2005 "Sensitivity of Metal Nanoparticle Surface Plasmon Resonance to the Dielectric Environment." The Journal of Physical Chemistry B, 109(46) 21556-2156.

69. Murphy, C. J., A. M. Gole, S. E. Hunyadi, J. W. Stone, P. N. Sisco, A. Alkilany, B. E. Kinard, and P. Hankins. 2008 "Chemical sensing and imaging with metallic nanorods." Chemical Communications, 8(5) 544-557.

70. Bae, Y. M, S. O. Jin, I. Kim, K. Y. Shin, D. Heo, and D. G. Kang. 2015 "Detection of Biomarkers Using LSPR Substrate with Gold Nanoparticle Array." Journal of

Nanomaterials, Article ID 302816 2015 1-6.

71. Schmid, A. H., S.E. Stanca, M.S. Thakur, K. R. Thampi, and C. R. Suri. 2006 “Site-directed antibody Immobilization on gold substrate for surface plasmon resonance sensors.” Sensors and Actuators B, 113 297–303.

72. Endo, T., K. Kerman, N. Nagatani, H. M. Hiepa, D. K. Kim, Y. Yonezawa, K. Nakano, and E. Tamiya. 2006 “Multiple Label-Free Detection of Antigen−Antibody Reaction Using Localized Surface Plasmon Resonance-Based.” Analytical Chemistry, 78 (18) 6465–6475.

73. Kajiura, M., T. Nakanishi, H. Iida, H. Takada, and T. Osaka. 2009 “Biosensing by optical waveguide spectroscopy based on localized surface plasmon resonance of gold nanoparticles used as a probe or as a label.” Journal of Colloid and Interface Science, 335 140-145.

74. Kim, D. K., T. J. Park, E. Tamiya, and S. Y. Lee. 2011 “Label-free detection of leptin antibody-antigen interaction by using LSPR-based optical biosensor.” Journal of Nanoscience and Nanotechnology, 11(5) 4188-93.

75. Hammond, J., N. Bhalla, S. Rafiee, and P. Estrela. 2014 “Localized Surface Plasmon Resonance as a Biosensing Platform for Developing Countries.” Biosensors, 4 172-188.

76. Endo, T., S. Yamamura, N. Nagatani, Y. Morita, Y. Takamura, and E. Tamiya. 2005 “Localized surface plasmon resonance based optical biosensor using surface modified nanoparticle layer for label-free monitoring of antigen–antibody reaction.” Science and Technology of Advanced Materials, 6 491–500.

77. Saleem, I. and Chu, W.K. 2016 “Gold nano ripple structure with potential for bio molecular sensing applications.” Sensing and Bio-sensing Research, 11(1) 14-19.

78. Lu, B., M. R. Smyth, and R. Okennedy. 1996 “Oriented immobilization of antibodies and its applications in immunoassays and immunosensors -Tutorial review.” Analyst**,** 121 29R-32R.

79. Turkova, J. 1999 “Oriented immobilization of biologically active proteins as a tool for revealing protein interactions and function.” Journal of Chromatography B: Biomedical Sciences and Applications, 722 11-31.

80. Shoham, B. 1995 “A bilirubin biosensor based on multilayer network enzyme electrode.” Biosensors and Bioelectronics, 10 341-352.

81. Gouda, H., H. Torigoe, A. Saito, M. Sato, Y. Arata, and I. Shimada. 1992 “Three dimensional solution structure of the B domain of staphylococcal protein A: comparisons of the solution and crystal structures.” Biochemistry, 31 9665-9672.

82. Goodman, R., Y. Chizmadzhev, and A. Shirley-Henderson. 1993 “Electromagnetic Fields and Cells, Journal of Cellular.” Biochemistry, 51 436-441.

83. Phillips, J. L. 1993 "Effects of electromagnetic field exposure on gene transcription." Journal of Cellular Biochemistry 51(4) 381-86.

84. Hardell, L. and Sage, C. 2008 “Biological effects from electromagnetic field exposure and public exposure standards.” Biomedicine & Pharmacotherapy, 62 104-l09.

85. Hsu, L. C., J. Fang, D. A. Borca-Tasciuc, R. W. Worobo, and C. I. Moraru. 2013 “Effect of Micro- and Nanoscale Topography on the Adhesion of Bacterial Cells to Solid Surfaces.” Applied and Environmental Microbiology, 79(8) 2703-2712.

86. Widdel, F. 2010 "Theory and Measurement of Bacterial Growth." Grundpraktikum Mikrobiologie.

87. Monzon, L. M. A., And J. M. D. Coey. "Magnetic Fields in Electrochemistry: The Lorentz Force. A Mini-Review." Electrochemistry Communications 42 (2014): 38-41.

88. Patil, R., H. Gholap, S. Warule, A. Banpurkar, G. Kulkarni, and W. Gade. 2015 “Quantum dots conjugated zinc oxide nanosheets: Impeder of microbial growth and biofilm.” Applied Surface Science, 326 73–81.

89. Lipovsky, A., A. Gedanken, and R. Lubart. 2013 “Visible light-induced antibacterial activity of metaloxide nanoparticles.” Photomedicine and Laser Surgery, 31(11) 526-530.

90. Brahma, N. S., Prateeksha, D. K. Upreti, B. R. Singh, T. Defoirdt, V. K. Gupta, A. O. De Souza, H. B. Singh, J. C. M. Barreira, I. C. F. R. Ferreira, and K. Vahabi. 2016 “Bactericidal, quorum quenching and anti-biofilm nanofactories: a new niche for nanotechnologists.” Critical Reviews in Biotechnology, 1-16.

91. Epstein, A. K., A. I. Hochbaum, P. Kim, and J. Aizenberg. 2011 “Control of bacterial biofilm growth on surfaces by nanostructural mechanics and geometry.” Nanotechnology, 22(49) 494007.

92. Díaz, C., M. C. Cortizo, P. L. Schilardi, S. G. Gómez de Saravia, M. A. F. Lorenzo de Mele. 2007 “Influence of the Nano-micro structure of the surface on bacterial adhesion.” Materials Research, 10(1) 11-14.

93. Armentano, I., C. R. Arciola, E. Fortunati, D Ferrari, S Mattioli, C. F. Amoroso, J. Rizzo, J. M. Kenny, M. Imbriani, and L. Visai. 2014 “The Interaction of Bacteria with Engineered Nanostructured Polymeric Materials: A Review.” The Scientific World Journal, 410-423

94. Patil, S. S., R. H. Patil, S. B. Kale, M. S. Tamboli, J. D. Ambekar, W. N. Gade, S. S. Kolekar, and B. B. Kale. 2014 “Nanostructured microspheres of silver @ zinc oxide: an excellent impeder of bacterial growth and biofilm.” Journal of Nanoparticle Research, 16 2717.

95. Hochbaum, A.I. and Aizenberg, J. 2010 “Bacteria Pattern Spontaneously on Periodic Nanostructure Arrays.” Nano Letters, 10(9) 3717-3721.

96. Kohno, M., M. Yamazaki, I. Kimura, and M. Wada. 2000 “Effect of static magnetic fields on bacteria: Streptococcus mutans, Staphylococcus aureus, and Escherichia coli.” Pathophysiology, 7(2) 143-148.

97. Brkovic, S., S. Postic, and D. Ilic. 2015 “Influence of the magnetic field on microorganisms in the oral cavity.” Journal of Applied Oral Science, 23(2) 179–186.

98. Mornet, S., S. Vasseur, F. Grasseta and E. Duguet. 2004 “Magnetic nanoparticle design for medical diagnosis and therapy.” Journal of Materials Chemistry, 14 2161-2175.

99. Lai, H. and Singh, N.P. 1991 “Magnetic-field-induced DNA strand breaks in brain cells of the rat.” Environmental Health Perspectives, 112(6) 687-94.

100. Sakurai, T. and Miyakoshi, J. 2009 "Biological effects of strong static magnetic fields on insulin-secreting cells." Journal of Physics: Conference Series 156 012014.

101. Adair, R.K. 1991 “Constraints on biological effects of weak extremely-low-frequency electromagnetic fields.” Physical Review A, 43 1039.

102. Frankel, R.B. 1979 “Magnetite in freshwater magnetotactic bacteria.” Science, 203 1355-1356.

103. Aarholt, E., E. A. Flinn, and C. W. Smith. 1981 “Effects of low-frequency magnetic fields on bacterial growth rate.” Physics of Medical Biology, 26(4) 613-621.

104. Strašák, L., V. Vetterl, and J. Šmarda. 2002 “Effects of low-frequency magnetic fields on bacteria Escherichia coli.” Bioelectrochemistry, 55(1-2) 161-164.

105. Segatore, B., D. Setacci, F. Bennato, R. Cardigno, G. Amicosante, and R. Iorio. 2012 “Evaluations of the Effects of Extremely Low-Frequency Electromagnetic Fields on Growth and Antibiotic Susceptibility of Escherichia coli and Pseudomonas aeruginosa.” International Journal of Microbiology, Article ID 587293, 1-7.

106. Justo, O. R., V. H. Pérez, D. C. Alvarez, and R. M. Alegre. 2006 “Growth of Escherichia coli under extremely low-frequency electromagnetic fields.” Applied

Biochemistry and Biotechnology, 134(2) 155-63.

107. Cellini, L. 2008 “Bacterial response to the exposure of 50 Hz electromagnetic fields.” Bioelectromagnetics, 29(4) 302-11 doi:10.1002/bem.20391.

108. Re, B. D., F. Bersani, C. Agostini, P. Mesirca, and G. Giorgi. 2004 “Various effects on transposition activity and survival of Escherichia coli cells due to different ELF-MF signals.” Radiation and Environmental Biophysics, 43(4) 265-70.

109. Subramanian, A., U. Krishnan, and S. Sethuraman. 2009 “Development of biomaterial scaffold for nerve tissue engineering: Biomaterial mediated neural regeneration.” Journal of Biomedical Science, 16 108.

110. Usmani, S., E. R. Aurand, M. Medelin, A. Fabbro, D. Scaini, J. Laishram, F. B. Rosselli, A. Ansuini, D. Zoccolan, M. Scarselli, M. De Crescenzi, S. Bosi, M. Prato, and L. Ballerini. 2016 “3D meshes of carbon nanotubes guide functional reconnection of segregated spinal explants.” Science Advances, 2(7) 1600087.

111. Straley, K.S. 2010 “Biomaterial Design Strategies for the Treatment of Spinal Cord Injuries.” Journal of Neurotrauma, 27(1) 1-19.

112. Fijalkowski, K., P. Nawrotek, M. Struk, M. Kordas, and R. Rakoczy. 2013 “The Effects of Rotating Magnetic Field on Growth Rate, Cell Metabolic Activity and Biofilm Formation by Staphylococcus Aureus and Escherichia Coli.” Article in Journal of Magnetics, 18(3) 289-296.

113. Shoda, M., K. Nakamura, K. Tsuchiya, K. Okuno, and T. Ano.1999 "Bacterial Growth under Strong Magnetic Field." Electricity and Magnetism in Biology and Medicine, 215-17.

114. Gerencser, V. F., M. F. Barnothy, and J. M. Barnothy. 1964 "Inhibition of Bacterial Growth in Fields of High Paramagnetic Strength." Biological Effects of Magnetic Fields, 229-39.

115. Hedrick, H. G. 1964 "Inhibition of Bacterial Growth in Homogeneous Fields." Biological Effects of Magnetic Fields, 240-45.

116. Gerencser, V. F., M. F. Barnothy and J. M. Barnothy, 1962 "Inhibition of Bacterial Growth by Magnetic Fields." Nature, 196 539-41.

117. Ramon, C., M. Ayaz, and D. D. Streeter. 1981 "Inhibition of growth rate of escherichia coli induced by extremely low-frequency weak magnetic fields." Bioelectromagnetics 2, no 3 285-89.